

Supersonic Cold Spraying for Energy and Environmental Applications: One-Step Scalable Coating Technology for Advanced Micro- and Nanotextured Materials

Seongpil An, Bhavana Joshi, Alexander L. Yarin,* Mark T. Swihart,* and Sam S. Yoon*

Supersonic cold spraying is an emerging technique for rapid deposition of films of materials including micrometer-size and sub-micrometer metal particles, nanoscale ceramic particles, clays, polymers, hybrid materials composed of polymers and particulates, reduced graphene oxide (rGO), and metal–organic frameworks. In this method, particles are accelerated to a high velocity and then impact a substrate at near ambient temperature, where dissipation of their kinetic energy produces strong adhesion. Here, recent progress in fundamentals and applications of cold spraying is reviewed. High-velocity impact with the substrate results in significant deformation, which not only produces adhesion, but can change the particles' internal structure. Cold-sprayed coatings can also exhibit micro- and nanotextured morphologies not achievable by other means. Suspending micro- or nanoparticles in a liquid and cold-spraying the suspension produces fine atomization and even deposition of materials that could not otherwise be processed. The scalability and low cost of this method and its compatibility with roll-to-roll processing make it promising for many applications, including ultrathin flexible materials, solar cells, touch-screen panels, nanotextured surfaces for enhanced heat transfer, thermal and electrical insulation films, transparent conductive films, materials for energy storage (e.g., Li-ion battery electrodes), heaters, sensors, photoelectrodes for water splitting, water purification membranes, and self-cleaning films.

1. Introduction

One of the most significant technological transformations in history is underway, particularly in energy and environmental fields, where we are witnessing massive shifts from nonrenewable to sustainable energy sources. As technological capabilities have grown exponentially in recent decades, many additional technological challenges have arisen, often as unintended consequences of prior advances. The development of advanced materials and the equally important development of economical processes for fabricating devices and systems using these materials have been essential to this rapid technological progress and will become even more important moving forward.

As mechanization, mass production, and automation marked watersheds in the early nineteenth, early twentieth, and mid-twentieth centuries, respectively, a new revolutionary change—the fourth industrial revolution (4IR)—is currently underway. Until now, these industrial

revolutions have occurred through sustained efforts to improve performance and lower costs by developing innovative fabrication technologies. For example, the power loom developed at the end of the eighteenth century and the automated assembly line developed in the early twentieth century were game-changers as scalable and cost-effective manufacturing processes, and thus these technologies significantly influenced modern industrial development.

The 4IR, including the Internet of Things (IoT), involves the coalescence of cyber and physical systems with a focus on networking between humans and machines.^[1] While this may appear to be less dependent upon fabrication technologies than prior industrial revolutions, the underlying hardware technologies for achieving the IoT, including miniaturized sensors, powerful computers, and various smart materials, require innovative, cost-effective, and scalable fabrication techniques. This includes not only these devices themselves, but also the associated energy harvesting, storage, and conversion devices needed to power them. In particular, with an increase in the importance of light, sturdy, flexible, and multifunctional materials, ultrathin components (i.e., films, filters/membranes, and electrodes) and their manufacturing have attracted significant

Dr. S. An, Prof. A. L. Yarin
Department of Mechanical and Industrial Engineering
University of Illinois at Chicago
Chicago, IL 60607-7022, USA
E-mail: ayarin@uic.edu

Prof. B. Joshi
Department of Physics
NES Science College
Snehnagar, Nanded 431605, Maharashtra, India

Prof. M. T. Swihart
Department of Chemical and Biological Engineering
and RENEW Institute
University at Buffalo
The State University of New York
Buffalo, NY 14260-4200, USA
E-mail: swihart@buffalo.edu

Prof. S. S. Yoon
School of Mechanical Engineering
Korea University
Seoul 02841, Republic of Korea
E-mail: skyoon@korea.ac.kr

 The ORCID identification number(s) for the author(s) of this article can be found under <https://doi.org/10.1002/adma.201905028>.

DOI: 10.1002/adma.201905028

interest during the past few years. For example, various nanoscale materials with morphologies ranging from 0D to multidimensional (i.e., 1D to 3D) are employed in optoelectronic applications for next-generation 4IR devices. Examples include quantum dots, nanofibers, ferroelectric nanostructures, and carbon-based materials.^[2–10]

Various bottom-up coating approaches have been employed to develop products based on 1 to 10 μm thick films of such nanomaterials, including magnetron sputtering,^[11,12] chemical vapor deposition (CVD),^[13,14] and physical vapor deposition (PVD).^[15,16] Specifically, these coating techniques have achieved remarkable results and have been deployed in numerous industries. Nevertheless, the high costs of vacuum-based systems, along with often time-consuming complex steps, have limited their further use in fabrication of the low-cost, high-performance, ultrathin materials required for 4IR technologies.

In recent years, our group has successfully addressed these issues by exploring and improving thermal spray-coating technologies, demonstrating their use for energy and environmental applications, and expanding the capabilities of this promising new coating approach. Here, we discuss a newer coating technique—supersonic cold spraying—that is capable of fabricating robust, ultrathin materials for energy and environmental applications in large quantities and at extremely low cost. This review briefly describes the fundamentals of the supersonic cold spraying technique and its feasible applications within the energy and environmental fields. In particular, this review addresses the questions of what supersonic cold spraying is, which factors make it attractive, and finally, why the cold spraying method holds great promise for the manufacturing of advanced energy and environmental materials.

1.1. Why Cold Spraying?

Thermal spraying techniques, which are defined as coating processes in which materials are deposited in a molten or softened condition on substrates, can be categorized into two groups depending on how the thermal energy is generated and contributes to the formation of the coating layer, namely i) combustion spraying and ii) electric discharge spraying (Figure 1a).^[17] A high-velocity gas jet, heated by combustion or an electric discharge process, issues from a torch (or a nozzle) in a spraying system, which almost instantaneously heats (and eventually melts or softens) and accelerates a coating material that is simultaneously fed into the gas stream. The accelerated and softened coating material directly impinges upon a substrate, thereby inducing strong physicochemical bonding between the material and substrate.

The remarkable capabilities of these thermal spraying methods for coating surfaces with microscale metallic and ceramic particles have been widely demonstrated. Thermally sprayed materials exhibit good adhesion to substrates and have been employed in various applications in the aerospace and automotive industries. This includes their use in the fabrication of engines and gas turbines.^[17,18] Thermal spraying has, therefore, become one of the leading coating technologies alongside PVD and weld-overlaying.^[19] For example, these coating



Seongpil An is a postdoctoral research associate in the Department of Mechanical and Industrial Engineering at the University of Illinois at Chicago. He received his B.S. and Ph.D. degrees from the School of Mechanical Engineering of Korea University, Seoul, South Korea, where he mainly researched metal-plated and self-healing nanofibers. His current research interests include, but are not limited to, fundamentals and multidisciplinary applications of multiscale polymer/metal/ceramic fibers.



Alexander L. Yarin received his M.Sc. in 1977, Ph.D. in 1980, and D.Sc. (Habilitation) in 1989. He started out at the Institute for Problems in Mechanics at the USSR Academy of Sciences, Moscow (1977–1990) and went on to become Professor at The Technion-Israel Institute of Technology (1990–2006; Eduard Pestel Chair Professor in 1999–2006) and then Distinguished Professor at The University of Illinois at Chicago, USA (2006–present). His fields of expertise are fluid and solid mechanics, polymer science, and nanotechnology.



Sam S. Yoon has been a Professor in the School of Mechanical Engineering at Korea University since 2005. He received a B.S. degree from Colorado School of Mines in 1997, and his M.S. and Ph.D. degrees in aeronautics and astronautics from Purdue University in 1999 and 2002, respectively. His fields of expertise are spray coating, aerosol science, and nanotechnology.

techniques have contributed to considerable technological advances in thermal barrier coatings (TBCs) and corrosion/erosion protective measures.^[17,20,21] Further details on thermal spraying technologies can be found elsewhere.^[17,21]

Because supersonic cold spraying can deposit coatings using various types of non-molten materials including solid powders and liquid solutions or suspensions, it is not strictly considered thermal spraying.^[17] However, similar to conventional thermal spraying techniques, the coating process depends upon the high kinetic energy and impact derived from the high-pressure

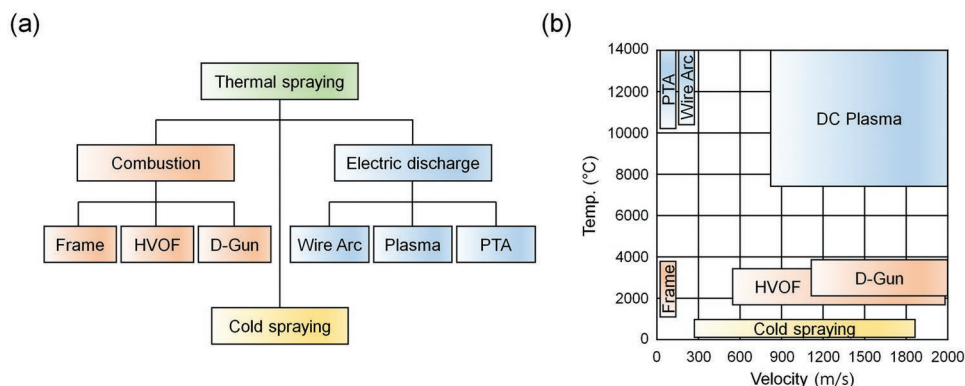


Figure 1. a) Thermal spraying technologies. b) Velocity and temperature ranges of carrier gas for each thermal spraying technology. HVOF: high-velocity oxy-fuel, D-Gun: detonation gun, PTA: plasma-transferred arc.

compressed gas used to propel the coating materials at high velocity (Figure 1b). As a result, the cold spraying technique is gaining recognition as a subset of thermal spraying methods in a broader sense (cf. Figure 1a).^[22] Accordingly, over the past few decades, the cold spraying technique has emerged as one of the essential powder (or particle) deposition additive manufacturing (AM) processes for the aerospace, shipping, and automotive industries, along with other thermal spraying techniques.

With increasing demand for cost-effective and scalable fabrication processes for ultrathin materials, researchers in the energy and environmental fields have devoted increasing attention to the cold spraying method as a rapid, scalable, and high-throughput deposition technique that is applicable to a nearly unlimited range of materials. Moreover, it can be operated at ambient pressure and relatively low temperature (cf. Figure 1b) compared with other bottom-up coating and thermal spraying methods. Thus, cold spraying methods can lower manufacturing costs and enable the use of heat-sensitive materials, giving them great potential as a next-generation large-scale thin-film coating technology in industry.

2. Fundamentals of Supersonic Cold Spraying: From Acceleration of Supersonic Carrier Gas to the Impact of Coating Materials on Substrates

The cold spraying method is based on a kinetic spraying process in which the coating materials (e.g., powders/particles, solutions, or suspensions) to be deposited onto a substrate are injected into a sub- or supersonic gas stream ($300\text{--}1800\text{ m s}^{-1}$, see Figure 1b) that is generated from a compressed gas issued at high pressure from a converging–diverging de Laval nozzle (Figure 2a). Although the gas is usually heated upstream of the nozzle, the temperature of the supersonic gas stream is near room temperature (RT), due to cooling as the compressed gas expands. Thus, this kinetic spraying process is called “cold” spraying. The coating materials in the gas stream are entrained and accelerated to supersonic velocities. Dissipation of their kinetic energy upon impact yields strong physicochemical and mechanical bonding to the substrate (Figure 2b).^[23] To achieve such bonding between the material and substrate, the

gas stream from the de Laval nozzle must exceed a threshold velocity—the so-called critical velocity (Figure 2c).^[22] The carrier gas can be air or an inert gas (e.g., N_2 , He, Ar, etc.) and must often be preheated to achieve the required critical velocity. However, as noted above, the preheated compressed gas rapidly cools as it expands through the diverging section of the nozzle, which renders this technique particularly suitable for coating metallic (or oxygen-sensitive) materials that would be oxidized by air at higher temperature.

In general, the cold spraying setup includes a compressor, gas heater, converging–diverging de Laval nozzle, powder feeder (or solution pump), and the substrate (see Figure 2a). High-pressure gas from the compressor is supplied to the de Laval nozzle, generally after preheating with a gas or electric heater. Because the coating materials should be deeply injected into the supersonic gas stream, the corresponding feed rate from the powder feeder (or solution pump) must be sufficiently high. Two approaches are used to introduce the coating material into the propelling gas. In upstream injection, the coating materials are injected before the throat of the converging–diverging nozzle. Alternatively, the coating materials can be supplied after the throat of the nozzle in downstream injection. Further details of these two approaches can be found elsewhere.^[22] We have recently developed a modified downstream approach in which the coating materials are atomized into the supersonic gas flow using an ultrasonic atomizer. This approach performs particularly well for coating nanomaterials in suspension form, as described in detail later in this review. The accelerated coating materials adhere well to a substrate when their impact velocity is above the critical velocity, which can be manipulated by varying the pressure and temperature of the compressed gas as well as the geometry of the nozzle.

While the adhesion mechanism of micrometer-size metal particles during cold spraying has been significantly explored over the past decades,^[17,22] that of multidimensional sub-micrometer materials (i.e., graphene, carbon nanotubes (CNTs), silver nanowires (AgNWs), polymers, hybrid materials, etc.) has rarely been considered, and thus still remains an open issue. In general, at the moment when metal particles are supersonically deposited onto a substrate, they undergo plastic deformation resulting from the high impact energy of cold spraying (cf. Figure 2b). Despite the fact that the processing temperature during cold

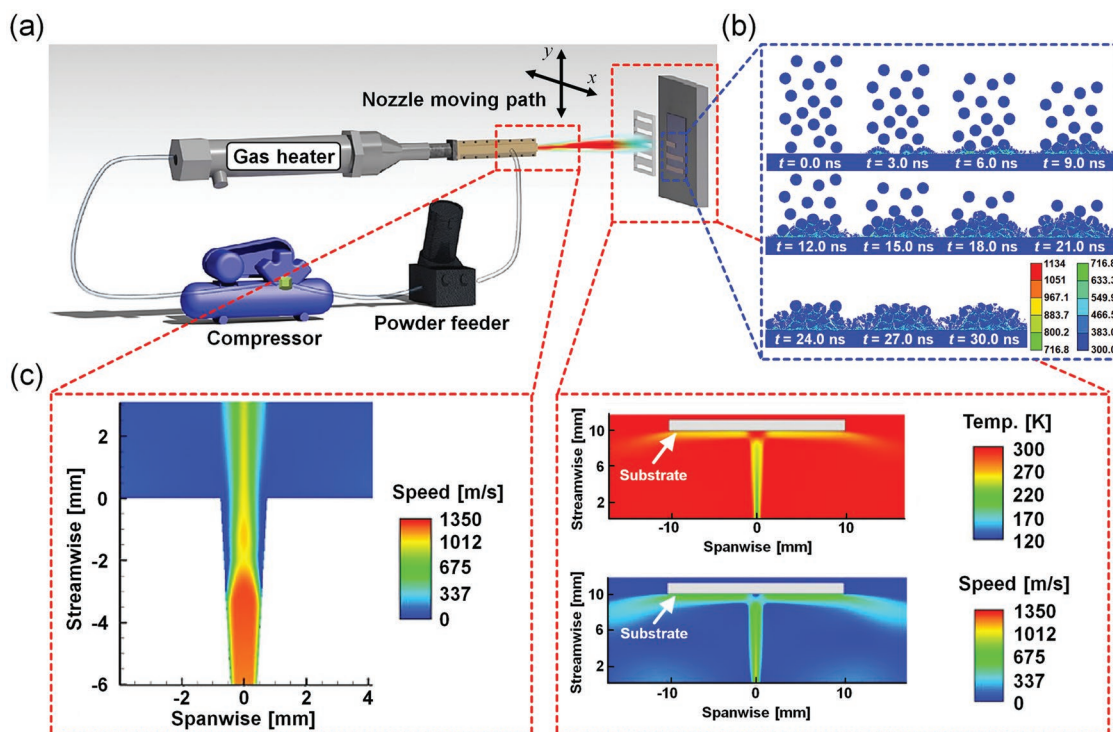


Figure 2. a) Schematic of the cold spraying process. b,c) Simulation results: b) the temperature distribution of cold-sprayed particles upon impact onto a substrate (where the inset bars indicate the temperature range) and c) the velocity of the gas stream issued from the exit of de Laval nozzle. a) Reproduced with permission.^[80] Copyright 2015, Elsevier. b) Reproduced with permission.^[35] Copyright 2015, Elsevier. c) Reproduced with permission.^[34] Copyright 2011, Springer Nature.

spraying is lower than in other thermal spraying techniques (Figure 1b), interfacial sintering between the metal particles and substrate naturally occurs as most of the impact energy is converted into heat due to adiabatic shear instabilities (ASI).^[24,25]

The underlying adhesion principles associated with multi-dimensional nanomaterials have not been elucidated in detail by combined numerical simulations and experiments because of the complexity of the coupled properties of nanomaterials. Nonetheless, higher viscoelasticity of nanomaterials compared with micrometer-size metal particles can enable them to be readily and strongly bonded to a substrate even at low pressure and with low preheating temperature of the carrier gas. Moreover, the low operating pressures and temperatures of the supersonic gas stream help to minimize oxidation, which has been a challenge in conventional thermal spraying methods. Reducing oxidation also served to improve adhesion of the nanomaterials to the substrate and to one another.

2.1. Studies on Supersonic Carrier Gas and Micrometer-Size Metal Coatings

Before the available coating materials for the cold spraying approach and their practical applications are discussed, we first emphasize that most theoretical and experimental studies before the mid-2000s focused on understanding how to generate and control the supersonic carrier gas (especially in the study of critical velocities (see Section 1.1)) for coating micrometer-scale

metal particles.^[26] Accordingly, these studies mainly explored the fundamentals of cold spraying technology rather than its potential applications. Although some reports did discuss applications,^[27] most of these were directed at specific needs of the aerospace and automotive industries, such as TBCs (thermal barrier coatings) and corrosion protection (see Section 1.1). Over the past 6 years, our group has begun to systematically explore the wide range of energy and environmental applications that can benefit from the cold spraying of nanometer-scale materials. Accordingly, this section focuses on studies performed before the mid-2000s while those related to energy and environmental applications are described in the subsequent sections.

The velocity of the supersonic gas stream and the resulting particle velocities are important, as foreign-object damage (FOD) can result from either deficient or excessive particle momentum. At the end of the 1990s, Smith and co-workers developed an analytical model to predict cold-sprayed particle velocities by assuming a 1D isentropic flow with constant gas properties and experimentally tested this model by cold-spraying micrometer-scale Cu powder (see Tables 1 and 2) and using a laser-based system for particle velocity measurement.^[28,29] They demonstrated that the velocities of Cu particles accelerated in He gas were higher than in air, and also found that the presence of the substrate in the setup practically did not influence the particle velocities. They also explored the geometrical changes of the Cu particles upon impact, at the interface between the supersonically accelerated particles and the fixed, polished stainless-steel substrate (cf. Table 2).^[30] As the

Table 1. Detailed geometric dimensions of converging–diverging de Laval nozzles used in studies of cold spraying. Note that only results based on experimental studies are listed.

| Material ^{a)} | Inlet-to-throat distance [mm] | D of circular throat ^{a)} [mm] | Throat-to-exit distance [mm] | Dimension at exit ^{a)} | Refs. |
|------------------------|-------------------------------|---|------------------------------|---|--|
| Steel | – | 2 | 80 | 2 × 10 mm ² (rectangle) | [29,30] |
| – | – | 3 | – | 6.5 mm (D of circular exit) | [32] |
| – | – | 2.7 | – | 8.1 mm (D of circular exit) | [38–42,46] |
| – | 20 | a (N ₂) | 130 | 5.6 × a (N ₂ , D of circular exit) | [43,44] |
| – | – | b (He) | – | 2.3 × b (He, D of circular exit) | – |
| – | – | 2 | 100 | 6 mm (D of circular exit) | [49,50,53] |
| – | 10 | 2 | 40 | 5 mm (D of circular exit) | [51] |
| – | – | 2 | 100 | 6 mm (D of circular exit) | [52,54] |
| – | – | c | 170 | 4.9 × c (D of circular exit) | [55] |
| – | 10 | 2 (He) | – | – | [57] |
| – | – | 2.7 (N ₂) | – | – | – |
| Steel | 30 | 2 | 180 | 6 mm (D of circular exit) | [58] |
| – | – | 3 | – | 6.5 mm (D of circular exit) | [60] |
| Al | 40 | 6 | 100 | 8.8 mm (D of circular exit) | [24,62–64,80,82,83,85–88,91,103,104,107,126–128,146,149,153–155,162–164] |
| – | 7.5 | 2.8–3.0 | 84 | 2.8 × 10 mm ² (rectangle) | [65] |
| – | – | 2.6 | – | – | [66] |
| Martensitic steel | – | 1.35 | – | 9.32 mm ² | [68] |
| – | – | 2 | 100 | 5 mm (D of circular exit) | [70] |
| – | – | 3 | – | 2 × 10 mm ² (rectangle) | [74] |
| – | – | 2 | – | 6.3 mm (D of circular exit) | [77] |
| Stainless-steel | – | – | – | 7.3 mm (D of circular exit) | [78] |
| Al | – | 6 | – | 8 mm (D of circular exit) | [102,106,156] |
| Al | – | 3 | – | 4.5 mm (D of circular exit) | [136] |
| Al | 40 | 3.5 | 90 | 4.5 mm (D of circular exit) | [137] |
| – | – | – | – | 4.8 mm (D of circular exit) | [141] |
| Al | – | – | – | 10 mm (D of circular exit) | [147,148] |

^{a)}D, diameter; N₂, nitrogen; He, helium; Al, aluminum.

velocity of the supersonic gas stream increased, the craters that formed on the substrate were found to be deeper and the radius of the resulting Cu splats increased.

In contrast to the work of Smith and Dykhuizen,^[28] Kwon et al.^[31] examined the 2D temperature and velocity distributions of supersonically blown nitrogen (N₂) gas using a computational fluid dynamics (CFD) code, PHOENICS. They investigated the detailed velocity profiles of N₂ propelling gas throughout the converging–diverging nozzle. In particular, they demonstrated that, under certain conditions, the corresponding particle velocities increased by 16% when the pressure of the N₂ carrier gas was doubled. Huang et al.^[32] also explored Cu particle velocities within a supersonic gas stream using a different CFD code, FLUENT. They compared their numerical results with experimental observations acquired using a DPV-2000 online diagnostic system (Tables 1 and 2). They investigated the effect of varying particle velocity on the particle adhesion to a substrate and demonstrated that spraying with He gas resulted in a higher adhesion strength than spraying with N₂ gas.

Our group also conducted numerical simulations to further understand the effects of shock waves, nozzle geometry, pressure, temperature, and substrate location on gas dynamics of the supersonic gas flow (cf. Figure 2c).^[33,34] We also used the FLUENT CFD code to computationally simulate and study the supersonic flow based on the nonlinear compressible Navier–Stokes equations. For this, the supersonic flows from different nozzle types (i.e., under-, properly-, and overexpanded) were simulated, and the shock-free operating conditions were explored. Furthermore, we have computationally investigated the deposition mechanism of cold-sprayed copper–indium–gallium–selenide (CIGS) particles (Figure 2b).^[35] In particular, we characterized the impact physics—the energy exchange, and substrate damage—and the optimal operating conditions for maximizing the growth rates of the deposited CIGS particles on molybdenum substrates. We note that, prior to this work, Grujicic et al.^[36,37] reported some numerical simulations (using the CFD codes CTH and ABAQUS) of the interfacial bonding mechanism between various micrometer-scale metal particles and metal substrates.

Table 2. Summary of studies of cold spraying of micrometer-size metal coatings. Note that only results based on experimental studies are listed.

| Material ^{a)} | Experimental parameter | | | | | | Application | Refs. | |
|------------------------|------------------------|-----------------------------|--|-------------------------|---------------------------------------|--------------------------------------|-------------|------------------------|-----------------------------------|
| | Carrier gas | | | Coating material | | | | | |
| | Pressure [MPa] | Preheating temperature [°C] | Max exit velocity [m s ⁻¹] | Material ^{a)} | Type ^{a)} | Feed rate | | | Nozzle-to-substrate distance [mm] |
| Air, He | 1.4–2.8 | 25–500 | 600 (air, 2.1 MPa, 27 °C) | Cu | Powder (<i>D</i> : 19, 22 μm) | 69 kPa | – | – | [29] |
| He | 3.4 | 500 | – | Cu | Powder (<i>D</i> : ≈22 μm) | – | – | – | [30] |
| N ₂ | 3, 4 | 200–1000 | 1200 | Cu | Powder (<i>D</i> : 5–45 μm) | 200 g min ⁻¹ | 30 | – | [32] |
| He | 2 | 600 | – | – | – | – | – | – | – |
| N ₂ | 2.5 | 300 | 990 | Cu | Powder (<i>D</i> : 5–25 μm) | 3 kg h ⁻¹ | 30 | – | [38] |
| N ₂ , He | 15–35 | 320 | – | Cu | Powder (<i>D</i> : 5–25 μm) | – | – | – | [39] |
| – | – | – | – | Al | Powder (<i>D</i> : <45 μm) | – | – | – | – |
| N ₂ | 2.5 | 380 | – | Cu | Powder (<i>D</i> : 5–25 μm) | – | – | – | [40] |
| – | – | – | – | Cu | Powder (<i>D</i> : 5–25 μm) | – | – | – | [41] |
| – | – | – | – | Al | Powder (<i>D</i> : <45 μm) | – | – | – | – |
| – | – | – | – | Ni | Powder (<i>D</i> : <25 μm) | – | – | – | – |
| N ₂ | 3 | 300 | – | Cu | Powder (<i>D</i> : 5–25 μm) | – | – | – | [42] |
| N ₂ | 3 | 305 | – | Cu | Powder (<i>D</i> : 5–35 μm) | 8.7 N m ³ h ⁻¹ | 30 | – | [43] |
| He | 2.5 | 305 | – | – | – | 7.2 N m ³ h ⁻¹ | – | – | – |
| N ₂ | 3 | 300 | – | Cu | Powder (<i>D</i> : 5–22 μm) | 8.7 N m ³ h ⁻¹ | 30 | – | [44] |
| He | 2.5 | 305 | – | – | – | 7.2 N m ³ h ⁻¹ | – | – | – |
| N ₂ | 3 | 800 | – | Cu | Powder (<i>D</i> : 5–25, 11–38 μm) | – | – | – | [45] |
| N ₂ | 2 | 204–268 | – | Ti | Powder (<i>D</i> : 38–44 μm) | – | 15 | – | [49] |
| He | 1 | 255 | – | – | – | – | – | – | – |
| N ₂ | 2 | 320, 410 | – | Zn | Powder (<i>D</i> : 5–25 μm) | – | 20 | – | [50] |
| N ₂ | 2 | 300 | – | Cu | Powder (<i>D</i> : 5–48 μm) | – | 30 | – | [51] |
| N ₂ , He | 1–2 | 165–320 | – | Cu | Powder (<i>D</i> : ≈56 μm) | – | 20 | – | [52] |
| N ₂ | 2 | 260 | – | Cu | Powder (<i>D</i> : 10–50 μm) | – | 20 | – | [53] |
| He | 2 | 390 | – | – | Powder (<i>D</i> : 26–68 μm) | – | – | – | – |
| N ₂ | 2 | 265 | – | Cu | Powder (<i>D</i> : ≈56.2 μm) | – | 20 | – | [54] |
| He | 1.5 | 495 | – | 316L stainless-steel | Powder (<i>D</i> : ≈9.6 μm) | – | – | – | – |
| He | 2 | 530 | – | Monel alloy | Powder (<i>D</i> : ≈20.8 μm) | – | – | – | – |
| Air | 2.7 | 513 | – | Annealed Cu | Powder (<i>D</i> : ≈99 μm) | 2.9 kPa | 30 | – | [55] |
| He | 0.15 | 20 | 833 | Al | Powder (<i>D</i> : 1–50 μm) | 20 g min ⁻¹ | 20 | – | [56] |
| He | 2 | 20 | – | Al | Powder (<i>D</i> : 10–53 μm) | – | 10–50 | – | [57] |
| – | – | – | – | Cu | Powder (<i>D</i> : 11–38 μm) | – | – | – | – |
| N ₂ | 3 | 300 | – | Ti | Powder (<i>D</i> : 10–50 μm) | – | – | – | – |
| N ₂ | 0.5–3 | RT | 650 | Al | Powder (<i>D</i> : 10–53 μm) | – | 30 | – | [58] |
| – | – | – | – | Cu, Sn | Powder (<i>D</i> : 10–32 μm) | – | – | – | – |
| N ₂ | 2 | 100 | – | Cu | Powder (<i>D</i> : ≈27 μm) | – | 30 | Antifouling | [59] |
| N ₂ | 3 | 300 | – | Al | Powder (<i>D</i> : ≈25 μm) | – | 25.4 | Heat exchanger | [60] |
| – | – | 900 | – | Stainless-steel | Powder (<i>D</i> : ≈14 μm) | – | – | – | – |
| N ₂ | 1.7 | 350 | – | Al | Powder (<i>D</i> : ≈25 μm) | – | – | Heat exchanger | [61] |
| Air, N ₂ | 0.4 | 227 | 569–923 | Cu | Powder (<i>D</i> : ≈10, 2.5, 0.8 μm) | 3 g min ⁻¹ | 50 | Electrode (solar cell) | [63] |
| – | 0.2–0.5 | 327–727 | – | Ni | Powder (<i>D</i> : ≈1.6 μm) | – | 30 | – | – |

Table 2. Continued.

| | | Experimental parameter | | | | | | Application | Refs. |
|------------------------|----------------|-----------------------------|--|--------------------------------------|--|--------------------------|-----------------------------------|----------------------|-------|
| | | Carrier gas | | Coating material | | | Nozzle-to-substrate distance [mm] | | |
| Material ^{a)} | Pressure [MPa] | Preheating temperature [°C] | Max exit velocity [m s ⁻¹] | Material ^{a)} | Type ^{a)} | Feed rate | | | |
| Air | 0.4 | 450–650 | 690–780 | Cu–Ni | Mixed powder (D_{Cu} : $\approx 6 \mu\text{m}$, D_{Ni} : $< 1 \mu\text{m}$) | – | – | Heater | [64] |
| Air | – | 315 (Al) 482 (Cu) | 1000 | Al Cu | Powder (D : $< 45 \mu\text{m}$) Powder (D : $< 45 \mu\text{m}$) | 4 g s^{-1} | – | – | [65] |
| N ₂ | 0.2–1 | 150 | – | Cu | Powder (D : 10–33 μm) | 5–10 g min ⁻¹ | 30 | – | [66] |
| Air | 1.4–2.2 | 300–450 | – | Cu | Powder (D : 10–45 μm) | – | 5–25 | – | [67] |
| He | 2.9 | RT | – | Cu | Powder (D : 5–25 μm) | 3.0 MPa | 20 | – | [68] |
| Air | 1.4–2.2 | 300–450 | – | Cu | Powder (D : $\approx 22 \mu\text{m}$) | – | – | – | [69] |
| He | 1.7 | 325 | – | Al | Powder (D : $\approx 25, 26 \mu\text{m}$) | 11 g min ⁻¹ | 25.4 | – | [70] |
| N ₂ | 2.5 | 350 | – | Al | Powder (D : 4–9, 20–37 μm) | – | 20 | – | [71] |
| N ₂ | 3 | 500 | – | Ni | Powder (D : 5–22 μm) | – | – | – | [72] |
| N ₂ | 2.1 | 540 | – | WC–Co | Powder (D : 10–43 μm) | – | 25 | – | [73] |
| N ₂ | 37.27 | 350–750 | – | Ti–Cu | Mixed powder (D : $< 75 \mu\text{m}$) | – | 10 | – | [74] |
| He | 3 | 600 | – | WC–Co | Powder (D : 5–45 μm) | 30 rpm | 15 | – | [75] |
| He | 1.7 | RT | – | Al alloy | Powder (D : $\approx 50 \mu\text{m}$) | 80 kPa | – | – | [76] |
| N ₂ | 1.6 | 350 | – | Al alloy | Powder (D : 15–20 μm) | – | 20 | – | [77] |
| | | 500 | – | | | | 15 | | |
| He | 0.98 | 300 | – | Al–Mg ₁₇ Al ₁₂ | Mixed powder (D_{Al} : $< 45 \mu\text{m}$, $D_{Mg17Al12}$: 48.5 μm) | 1030 kPa | 10 | Corrosion protection | [78] |
| N ₂ , He | 1–4 | 25–800 | 580–1140 | Ti Ti alloy | Powder (D : $\approx 29 \mu\text{m}$) | 1–2 g min ⁻¹ | – | – | [79] |

^{a)}He, helium; Cu, copper; D , diameter; N₂, nitrogen; Al, aluminum; Ni, nickel; Ti, titanium; Zn, Zinc; RT, room temperature; Sn, tin; WC, tungsten carbide, Co, cobalt.

Kreye and co-workers^[38–48] examined the cold spraying process employing both numerical simulations and experiments, mainly using Cu powder in the 5–38 μm diameter range. Using FLUENT, they found that the critical velocity for cold spraying Cu powder within the 5–25 μm diameter range was 570 m s⁻¹.^[38] They also investigated the effect of particle velocity on the flattening ratio of the deposited particles through finite element modeling of plastic deformation using ABAQUS.^[39,48] They studied the microstructural and macroscopic properties of different cold-sprayed metal powders, including Cu, Al, and Ni, by means of scanning and transmission electron microscopies (SEM and TEM, respectively, cf. Tables 1 and 2).^[40–42] They also compared the cold-sprayed metal coatings with those fabricated by other thermal spraying techniques.^[43,44] While the electrical conductivity and mechanical properties of the cold-sprayed Cu layers were comparable to those of bulk Cu, the properties resulting from the other thermal spraying methods were inferior.

As listed in Tables 1 and 2, Li and co-workers also studied the cold spraying method using different micrometer-size metal powders including Ti,^[49] Zn,^[50] Cu,^[51–54] steel,^[54] Monel alloy (a Ni–Cu alloy with high strength and outstanding corrosion resistance in a range of aggressive media),^[54] and annealed Cu,^[55] and also varied the geometric design of the de Laval nozzle.^[51] They compared their experimental results on particle

deformation with the numerical investigation conducted using both Lagrangian and arbitrary Lagrangian–Eulerian methods.^[53] Notably, the critical velocity for the deposition of Cu particles in the work of Li and co-workers ranged from 298 to 356 m s⁻¹,^[52] which is somewhat below the range obtained by Stoltenhoff et al.^[38] owing to differences in the size of the Cu particles and the operating conditions (Table 2).

O’Neill and co-workers^[56–58] also undertook notable research on cold spraying technologies (cf. Tables 1 and 2) to explore the effects of bow shock phenomena with varying nozzle standoff distances (i.e., nozzle-to-substrate distances). Using CFD, particle image velocimetry, and Schlieren imaging, they found that the backward effect of bow shock negatively influenced particle velocities within the supersonic gas.^[57] Subsequently, they investigated the use of cold spraying to form metallic coatings on polymer substrates (Table 2) including polycarbonate/ABS (PC/ABS), polystyrene (PS), nylon 6, polypropylene (PP), and glass fiber composites.^[58] Contrary to previous studies, they set the preheating temperature of the propelling gas to RT to prevent damage to the polymer substrates from the supersonically accelerated metal particles. Nevertheless, cold spraying of Cu and Al powders caused issues through the erosion of the polymer substrates and low critical velocities, respectively. However, polymer substrates could be effectively coated with Sn

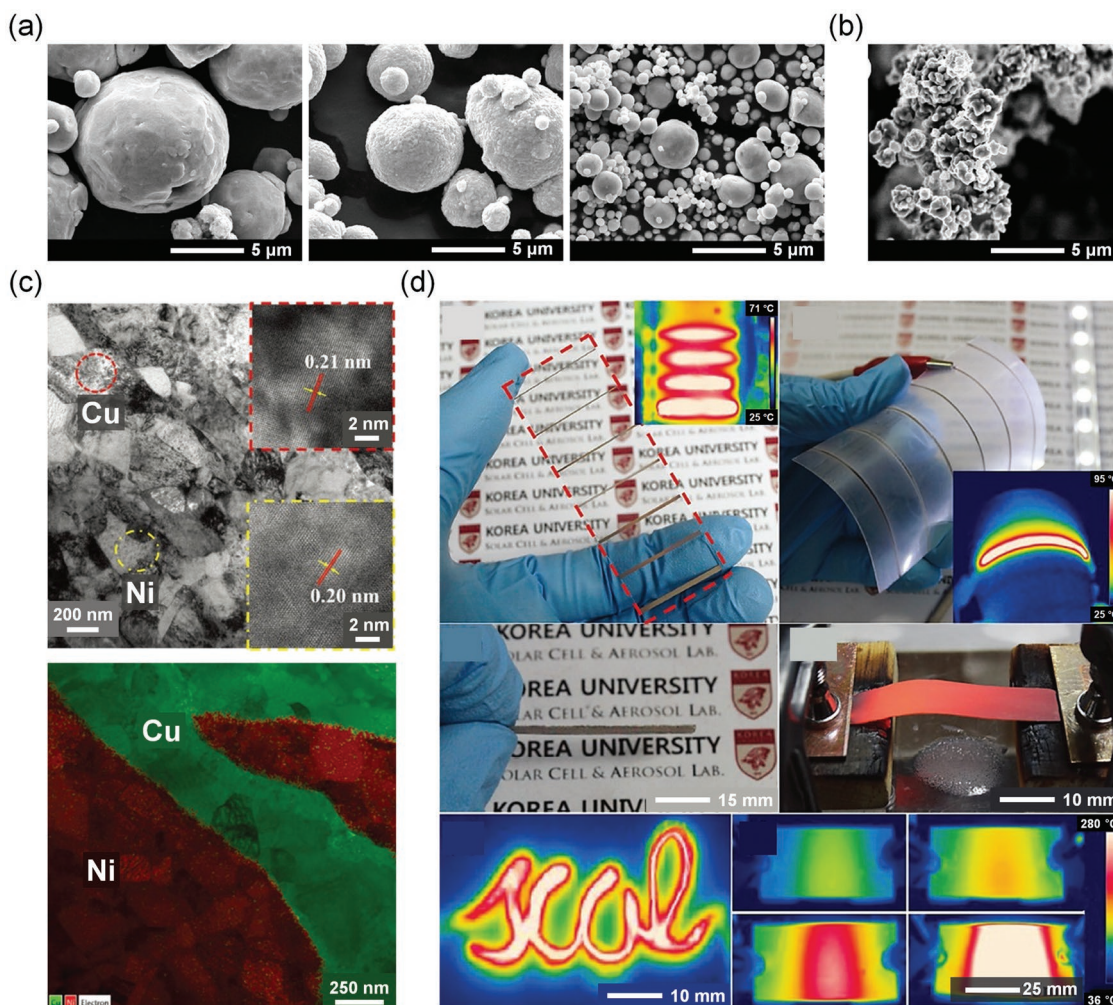


Figure 3. a,b) Scanning electron microscopy (SEM) images of Cu (a) and Ni (b) particles of different diameters for cold spraying. c) Transmission electron microscopy (TEM) and the corresponding energy-dispersive X-ray (EDX) images of Cu–Ni electrodes fabricated by cold spraying with Cu–Ni mixed powder. d) Photographs showing heating performance of cold-sprayed Cu–Ni electrodes. a,b) Reproduced with permission.^[63] Copyright 2017, Elsevier. c,d) Reproduced with permission.^[64] Copyright 2017, Wiley-VCH.

powder with particle diameters in the 10–32 μm range without such issues. Vucko et al.^[59] also demonstrated the deposition of Cu particles onto thermoplastic polymers, including high-density polyethylene (HDPE) and nylon. Contrary to the work of the O'Neill group, they showed an application of cold-sprayed Cu films on polymer substrates, which targeted antifouling technology. The Cu films (deposited on HDPE) revealed an antifouling effect for the duration of the 250-day field trial, while coated nylon was heavily fouled. This indicates that the physical interaction between the metal particles and polymer substrate is highly dependent on the physical properties of the polymer substrate (e.g., its elastic modulus and hardness).

In subsequent works by Cormier et al.^[60,61] and Dupuis et al.,^[60,61] the use of cold spraying in energy applications, specifically for efficient heat transfer, was also demonstrated (see Section 3.1.2). The coating materials used in these studies were tens of micrometers in size, and the technique was inapplicable to the fabrication of ultrathin materials (Tables 1 and 2). Specifically, they manufactured pyramidal pin fin arrays

by cold spraying Al and stainless-steel powders with a diameter range of 14–25 μm (Table 2), where the patterned fin arrays were formed through masking with meshes. Furthermore, they explored the heat transfer performance achievable by varying the structure and pattern of the cold-sprayed Al fin arrays (Section 3.1.2). Prior to this work, our group demonstrated the feasibility of using the cold spraying method with sub-micrometer metal powders (Cu particles)^[62] for the fabrication of pyramid-shaped electrodes and their potential use in photovoltaic solar cells (see Sections 2.2 and 3.1.1).

Additionally, our group fabricated Cu–Ni electrodes using the cold spraying method with micrometer-scale Cu and Ni powders (Figure 3 and Table 2), and considered their potential use as front electrodes in photovoltaic solar cells (see Section 3.1.1) and thin-film heaters (cf. Section 3.1.4).^[63,64] Note that the pressure range of the carrier gas used in these studies was lower (0.2–0.5 MPa) than those previously reported for cold spraying using micrometer-scale metal particles (typically in the order of 1 MPa, see Table 2). This was because the overall sizes of the Cu and Ni particles

used were smaller than in previous studies (see Figure 3a, b, and Table 2). We also employed different approaches to fabricate the Cu–Ni electrodes. Specifically, while we sequentially deposited Ni and Cu layers in the first instance, which resulted in double-layered Cu–Ni electrodes,^[63] we simultaneously sprayed mixed Cu and Ni particles to yield heterogeneous Cu–Ni composites (see Figure 3c).^[64] The ductile nature of the metal particles enabled the supersonically accelerated particles to be inelastically deformed and spread over the substrates, thereby forming distinct grain boundaries between the Cu and Ni clusters (see Figure 3c).

In addition to the above-mentioned works, many other groups have studied cold-spraying and mechanical properties of various micrometer-scale metal particles including Cu,^[65–69] Al,^[65,70,71] Ni,^[72] and alloys^[73–79] (Figure 4 and Table 2). While these additional studies have led to significant progress in metal cold-spraying techniques, the methods used to analyze cold-sprayed metal coatings have been similar to the previous studies. Accordingly, the details of these reports are not further reviewed here, but the corresponding operating conditions and adopted supersonic nozzle geometries are listed in Tables 1 and 2.

2.2. Sub-Micrometer Metal Coatings

Our group first reported the deposition of sub-micrometer-scale metal particles (which have an average diameter of

less than 1 μm) via the cold spraying technique to fabricate front electrodes for solar cells (Figure 5 and cf. Section 3.1.1).^[62,80] We emphasize that this study demonstrated the feasibility of the cold spraying technique as a new class of coating methods for next-generation energy and environmental applications. In this work, a newly developed Al-based de Laval nozzle with a throat diameter of 6 mm (Table 1)^[62] was used. It optimized the cold spraying operating conditions allowing one not only to employ sub-micrometer-scale metal particles (Figure 5a and Table 3) but also to obtain thin metallic lines with widths of 150–1500 μm (Figure 5b).^[62,80] The exit velocity (V_e) from the de Laval nozzle was 779 m s^{-1} , which was found as $V_e = M_e(\gamma RT_e)^{1/2}$, where M_e and T_e are the exit Mach number and exit static temperature, respectively (cf. Table 3). A masking slit in the cold spraying process was employed, which resulted in unique pyramid-shaped electrodes (see Figure 5b inset) owing to the formation of a so-called recirculation zone (Figure 5c).^[62]

In subsequent work, Jo et al.^[81] also used steel masks to form multiple Cu lines on Cu substrates for heat transfer applications (Figure 6a, Table 3, and cf. Section 3.1.2), where each Cu line was identical with a height and width of 128 and 348 μm , respectively (an aspect ratio of 0.37). To vary the number of patterned Cu lines, different masks were used with different numbers of slits. In addition to the Cu lines, Jo et al.^[82] also demonstrated the formation of frustum pyramid-shaped Cu pillars, with

Table 3. Summary of studies of cold spraying of sub-micrometer metal coatings. Note that only results from experimental studies are listed.

| | | Experimental parameter | | | | | | Application ^{a)} | Refs. |
|-------------|----------------|-----------------------------|---|--|--|---------------------------------|-----|---------------------------|-------|
| Carrier gas | | Coating material | | | Nozzle-to-substrate distance [mm] | | | | |
| Material | Pressure [MPa] | Preheating temperature [°C] | Max exit velocity [m s^{-1}] | Material ^{a)} | Type ^{a)} | Feed rate | | | |
| Air | 0.6 | 320 | 779 | Cu | Powder ($D: \approx 1 \mu\text{m}$) | 3 g min^{-1} | 55 | Electrode (solar cell) | [62] |
| Air | 0.4 | 350 | – | Ni | Powder ($D: \approx 1.64 \mu\text{m}$) | 0.01 g s^{-1} | – | Electrode (solar cell) | [80] |
| | | | | Cu | Powder ($D: \approx 0.8 \mu\text{m}$) | | | | |
| Air | 0.6 | 320 | – | Cu | Powder ($D: \approx 1 \mu\text{m}$) | 25 L min^{-1} | 55 | Cooling | [81] |
| Air | 0.6 | 320 | – | Cu | Powder ($D: \approx 1 \mu\text{m}$) | 25 $\text{m}^3 \text{min}^{-1}$ | 66 | Cooling | [82] |
| Air | 0.5 | 447 | 730 | Cu | Powder ($D: \approx 0.8 \mu\text{m}$) | 10 L min^{-1} | – | – | [24] |
| Air | 0.45 | 250–400 | 730–830 | Cu | Powder ($D: \approx 0.72 \mu\text{m}$) | 3 g min^{-1} | 40 | Electrode (solar cell) | [83] |
| Air | 0.4 | 550 | – | Cu | Powder | 3 g min^{-1} | 30 | Cooling | [84] |
| | | | | AgNW (dispersed in IPA) | Suspension | – | | | |
| Air | 0.15–4 | 100, 220, 300, 400 | 266–677 | AgNW (dispersed in IPA and ethanol) | Suspension | 1.2 mL min^{-1} | – | TCF | [85] |
| Air | 0.1–0.4 | 200–300 | 690–780 | AgNW (dispersed in IPA) | Suspension | 1.2 mL min^{-1} | 50 | Transparent heater | [86] |
| Air | 0.4 | 220 | – | AgNW (dispersed in IPA) | Suspension | 1.2 mL min^{-1} | 200 | Self-cleaning | [87] |
| | 0.4 | 250 | | SiO ₂ (dispersed in PAN-DMF, cf. Table 5) | | 1.5 mL min^{-1} | | | |
| | 0.3 | 350 | | PS (dissolved in DMF, cf. Table 6) | Solution (0.11 wt%) | 1.2 mL min^{-1} | | | |
| Air | 0.4 | 220 | – | AgNW (dispersed in IPA) | Suspension | 1.2 mL min^{-1} | – | Cooling | [88] |
| Air | 0.4–0.6 | 60–220 | – | AgNW (dispersed in IPA) | Suspension | 1.2 mL min^{-1} | 180 | TCF | [89] |

^{a)}Cu, copper; D, diameter; Ni, nickel; AgNW, silver nanowire; IPA, isopropyl alcohol; TCF, transparent conducting film; SiO₂, silicon dioxide, PAN, polyacrylonitrile, DMF, dimethylformamide, PS, polystyrene.

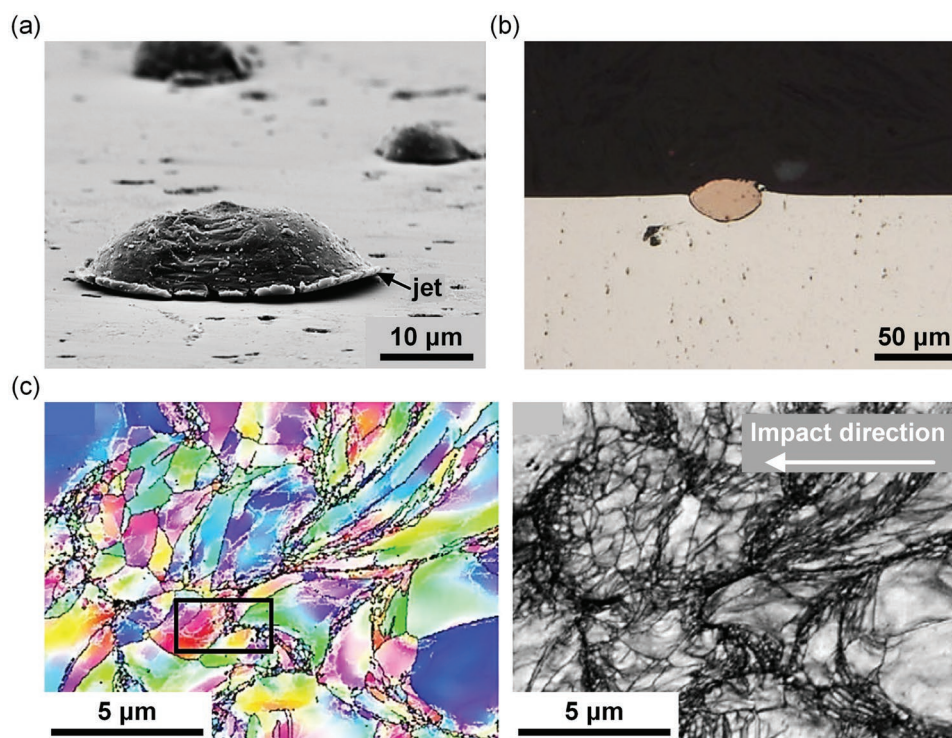


Figure 4. a) Scanning electron microscopy (SEM) image of Al particles deposited on a lead zirconate titanate substrate. b) Cross-sectional photograph of a Cu splatter on a substrate. c) Electron backscatter diffraction (EBSD) and the corresponding SEM image of a cold-sprayed Ni layer. a) Reproduced with permission.^[71] Copyright 2010, Elsevier. b) Reproduced with permission.^[32] Copyright 2011, Springer Nature. c) Reproduced with permission.^[72] Copyright 2009, Elsevier.

different sizes and patterns, on Cu substrates by cold spraying and masking through wire meshes (Figure 6b and Table 3).

Also, multilayered Ni–Cu electrodes, with a thickness of 1–30 μm , were fabricated by conducting consecutive cold spraying while controlling the number of nozzle scans and the corresponding scanning speed, as well as varying the operating conditions (Tables 1 and 3).^[80] To further understand the deposition mechanisms of layered metal clusters by consecutive cold spraying, numerical simulations were conducted and the results were compared with experimental observations (cf. Tables 1 and 3).^[24] This revealed deposition phenomena in detail including the impacts, flattening, sintering, and growth of metal particles (Figure 5d,e). The ANSYS Autodyn software package (Canonsburg, PA, USA) was used to simulate the physicochemical behavior of metal particle deposition, where the flattening of particles was simulated via smoothed particle hydrodynamics (SPH) using a stress-failure model. The corresponding thermodynamic properties were obtained using equations of state (EOS).

Variations in the electrical properties and morphologies of cold-sprayed metal layers on substrates were explored by varying the gas preheating temperature between 250 and 400 $^{\circ}\text{C}$ (Tables 1 and 3, and cf. Section 3.1.1) while keeping other operating conditions fixed.^[83] In these experiments, the diameter of Cu particles was 0.72 μm and these were patterned as grids on a Si wafer (Table 3). The exit gas and particle velocities in supersonic flow increased with the preheating temperature, which resulted in an increase in the thickness of the cold-sprayed Cu grids from 9 to 30 μm .

Apart from long and thin Cu lines for electrodes, large-area Cu layers were also fabricated via cold spraying for electronic cooling applications (cf. Section 3.1.2).^[84] For this, the cold-sprayed Cu layers were also nanotextured by sandblasting with kanthal (Mo_2Si) nanoparticles (which have a high hardness of 8500 MPa). The sandblasting process contributed to dimpling of the surface of the Cu layers at the nanometer scale, resulting in a significant increase in the overall surface area. The sandblasting was also conducted using the cold spraying system, for which kanthal powder was sprayed instead of the Cu powder. Because of their extremely high hardness, the kanthal particles were deflected upon impact rather than being deposited on the Cu layers. This facilitated the nanotexturing of the Cu layers.

In addition, the cold spraying of 1D metallic nanomaterials was reported. In particular, the deposition of silver nanowires (AgNWs) on flexible large-area substrates was demonstrated by introducing a roll-to-roll system into the cold spraying setup (Figure 7, Tables 1 and 3).^[85] This study was not only the first example of cold-spraying of AgNWs, but was also novel in employing a suspension-type material in cold-spraying (Figure 7a and Table 3). For cold spraying of a suspension, new converging–diverging nozzle geometries were designed, in which the AgNW suspension was supplied within the nozzle via downstream injection (see Figure 7a). The moment the sprayed AgNWs impacted the substrate, the kinetic energy of the supersonic air-stream was converted into thermal energy, which enabled the solid AgNWs to self-fuse (Figure 7b). As a

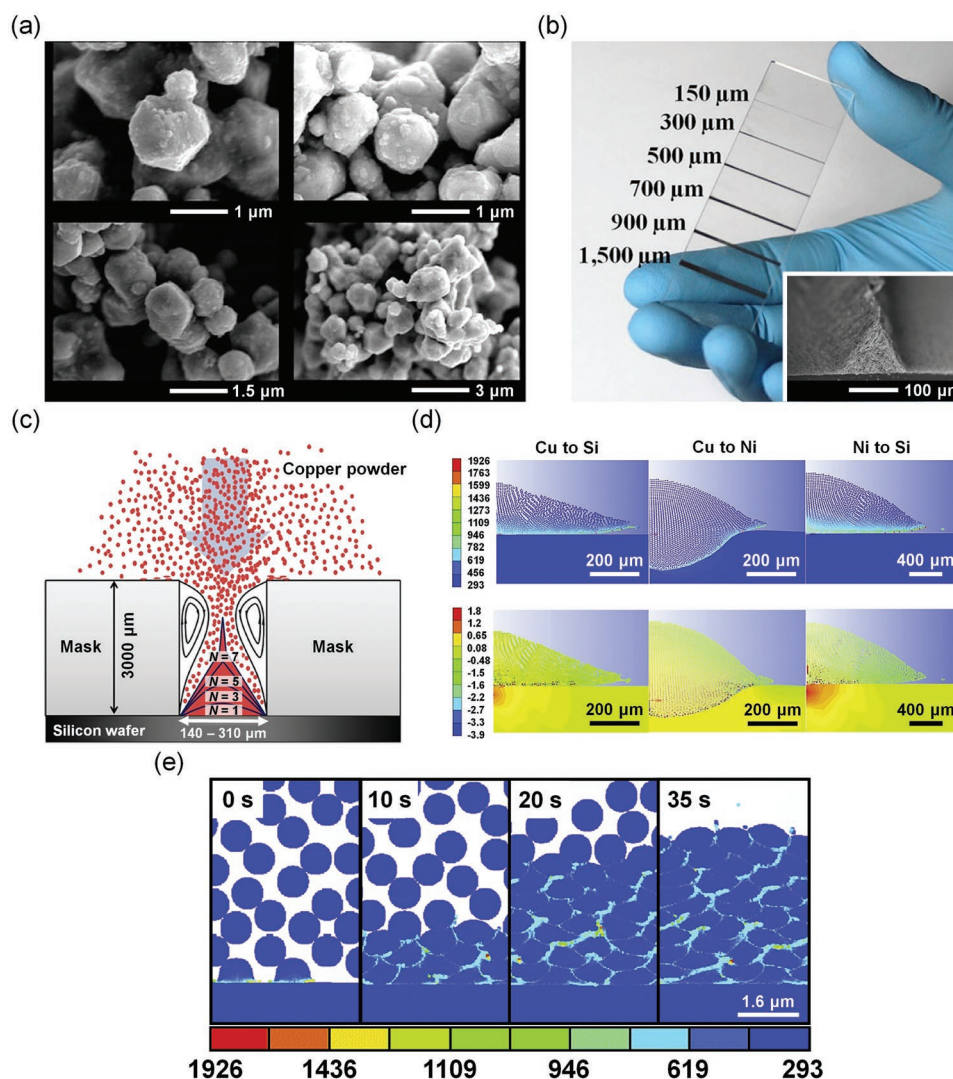


Figure 5. a) Scanning electron microscopy (SEM) images of Cu particles with diameters of 0.5–1.5 μm . b) Photograph of Cu electrodes on glass produced by cold spraying. Inset is an SEM image of the Cu electrode with a width of 150 μm . c) Sketch of the formation of pyramid-shaped Cu electrodes. d,e) Results of numerical simulations of the deposition of metal particles onto a substrate: d) temperature and pressure distributions with different materials and e) deformation patterns and temperature profile as a function of time. a–c) Reproduced with permission.^[62] Copyright 2013, Springer Nature. d,e) Reproduced with permission.^[24] Copyright 2015, Elsevier.

result, a percolative network of sintered AgNWs facilitated electron transport, thereby yielding remarkable electrical performance as flexible transparent conducting films (TCFs, cf. Figure 7c and Section 3.1.3).

In another study, a slightly different method of cold spraying AgNWs was proposed, whereby the AgNW suspension was introduced into a supersonic gas flow using an ultrasonic atomizer (see Figure 8a and cf. Tables 1 and 3).^[84,86–89] We emphasize that the use of a suspension with the atomizer reduced the potential for aggregation of AgNWs during the cold spraying process. Moreover, the atomizer allowed the solvent in the AgNW suspension to rapidly evaporate in the supersonic air-stream, so that the airborne AgNWs could be coated in a dry state on the substrates (e.g., Cu,^[84,88] Ecoflex,^[85] poly(ethylene terephthalate) (PET),^[85,86] polyimide (PI),^[89] soda-lime glass,^[86] and others^[86]).

2.3. Nanoscale Carbon Material Coatings

Graphene has a unique combination of physicochemical and electrical properties among many types of carbon-based nanomaterials. For example, it not only has an ultrahigh specific surface area of 2630 $\text{m}^2 \text{g}^{-1}$ but also ultrafast electron mobility of $2.5 \times 10^5 \text{ cm}^2 \text{V}^{-1} \text{s}^{-1}$ and high thermal conductivity of $5000 \text{ W m}^{-1} \text{K}^{-1}$.^[90] However, significant challenges still remain before graphene can be practically employed in commercial products in various industrial applications. One of the major issues is that there are no economically feasible, industrially viable, and cost-effective fabrication/deposition methods for graphene that maintain its favorable properties.^[91]

To address these issues, numerous approaches have been proposed to achieve efficient fabrication/deposition methods for graphene including adhesive-tape-peeling,^[92,93] chemical

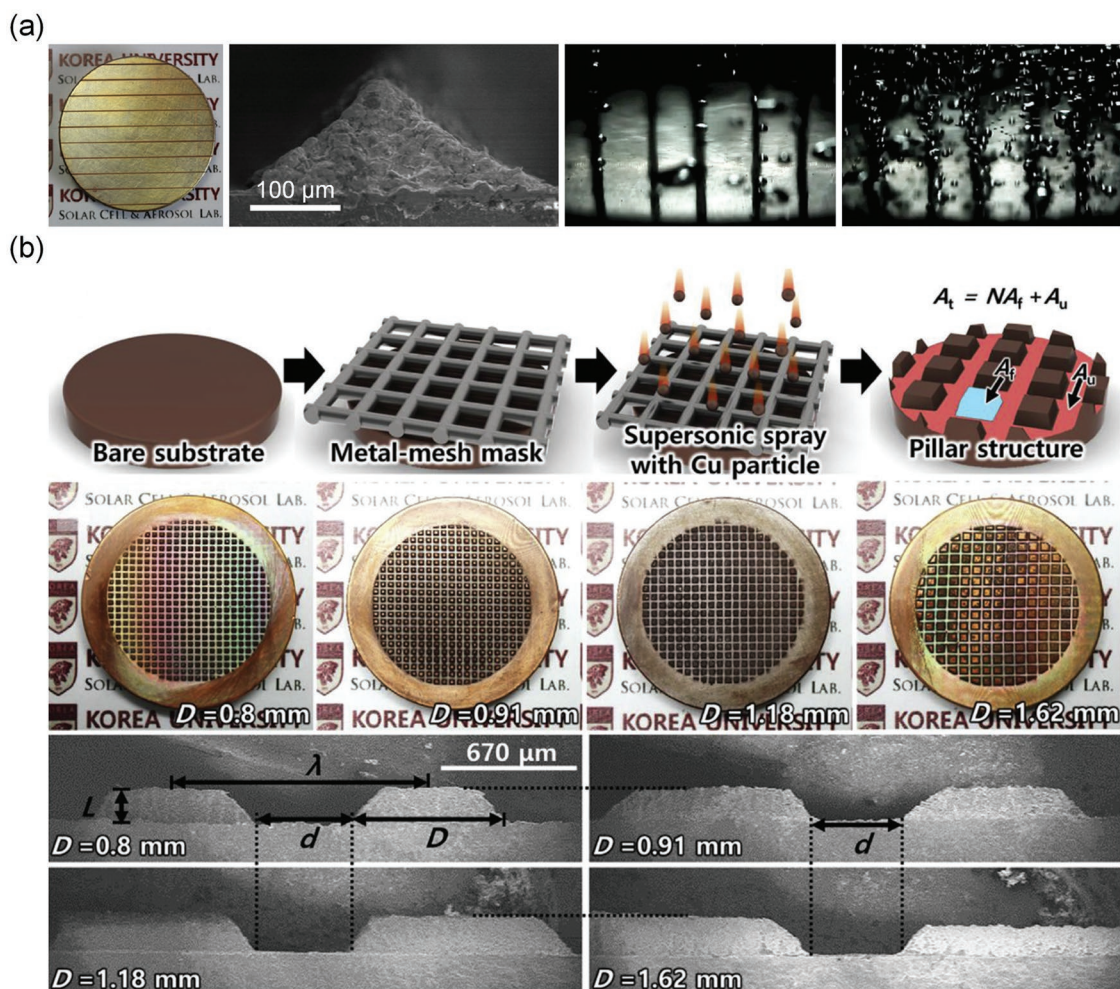


Figure 6. a) Photograph and scanning electron microscopy (SEM) images of pyramid-shaped Cu lines on a Cu substrate (the first and second images). High-speed camera snapshots in a pool boiling test of the corresponding specimen, with increasing saturated temperature (the third and fourth images). b) Schematic, photographs, and SEM images of cold-sprayed frustum pyramid-shaped Cu pillars on Cu substrates. a) Reproduced with permission.^[81] Copyright 2017, Elsevier. b) Reproduced with permission.^[82] Copyright 2018, Elsevier.

vapor deposition (CVD),^[94,95] and various solution-based deposition methods (i.e., dip coating,^[96,97] spin coating,^[98,99] and spray coating^[91,100,101]). Among these methods, the supersonic cold spraying technique recently demonstrated the most promise for large-scale graphene coating, as post-treatments are not required to eliminate defects in the deposit that would otherwise degrade its physicochemical properties.^[87] In addition, cold spraying deposition can be performed on nearly any substrates.

The investigation of the deposition of graphene using the cold spraying method employed reduced graphene oxide (rGO) dispersed in different solvents, including ethanol, toluene, methylethyl ketone (MEK), butyl-carbitol acetate (BCA), isopropyl alcohol (IPA), and dimethylformamide (DMF) (see Table 4).^[91,102–104] While large-scale production of pristine graphene remains difficult and expensive, rGO has become one of the most promising graphene-like materials due to its relatively low-cost and scalable production combined with properties comparable to pure graphene. The deposition of rGO on both stiff and soft substrates via cold spraying of a suspension (cf. Figures 9, 10, and 11) was successful. Moreover, an

interesting self-healing effect of cold-sprayed rGO was reported, which was achieved by stretching of the rGO structure upon impact onto the substrate during cold spraying.^[91] Namely, the energy generated at the impact of the supersonically sprayed rGO with a substrate was naturally converted to elastic energy of the rGO structure. This facilitated the healing of Stone–Wales defects^[105] in rGO by rearranging (or stretching) defective pentagonal and heptagonal carbon structures into regular hexagonal carbon structures (see Figure 9c). Indeed, the ratio of the intensity of the D peak to that of the G peak in Raman spectra (which indicates the degree of defects in graphene) was reduced from 0.62 to 0.22 after cold spraying, indicating a reduced number of defects in the cold-sprayed rGO (see Figure 9d). This unique self-healing phenomenon, which was reported in ref. [91] for the first time, endows the cold spraying method with great promise as a cost-effective and scalable application method for graphene and graphene-like materials deposition on surfaces in industry.

To develop water purification membranes consisting of highly concentrated rGO (cf. Section 3.2.1), cold spraying of

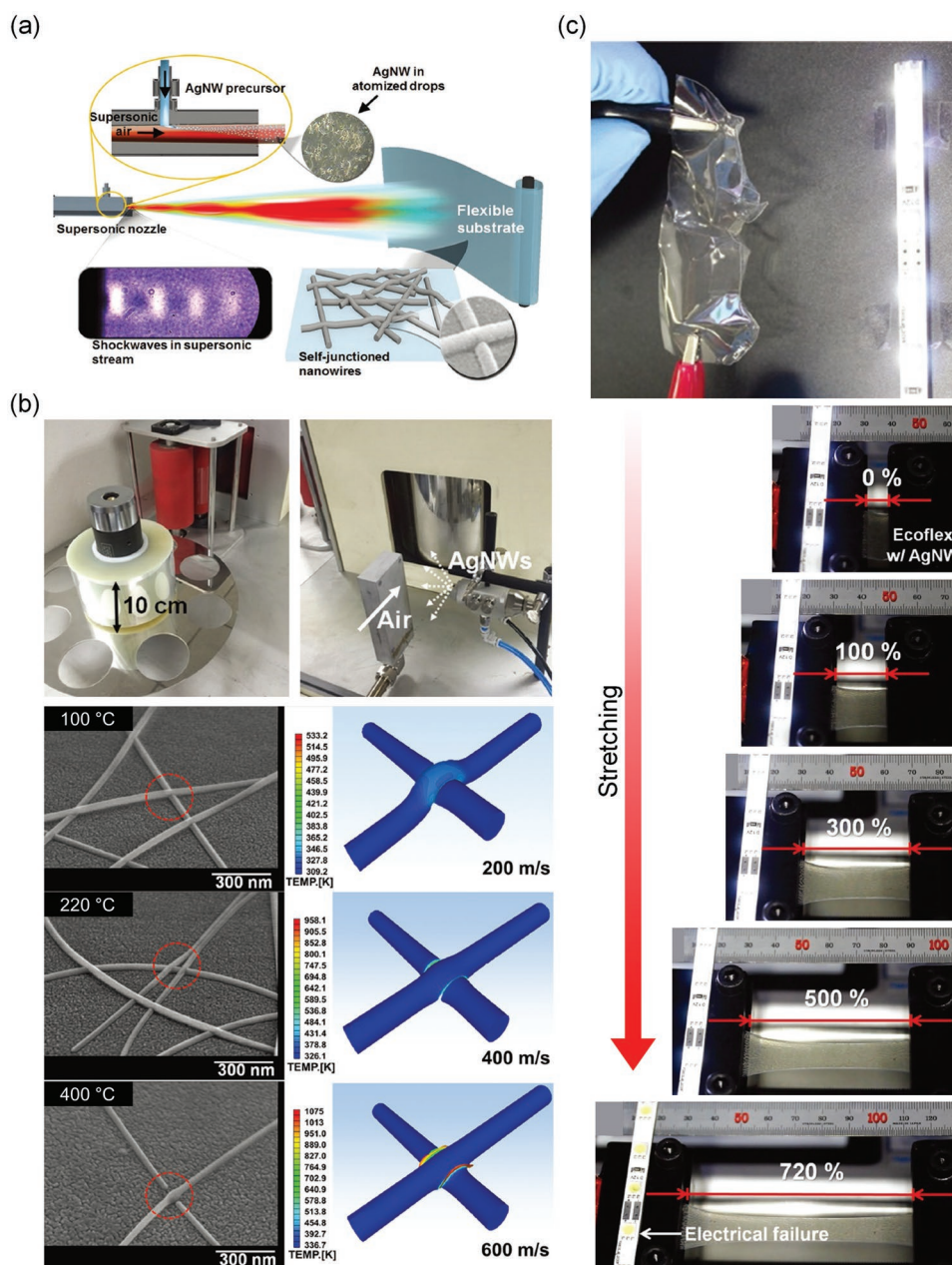


Figure 7. a) Schematic of a cold spraying system for AgNW suspension. b) Photographs of the roll-to-roll cold spraying setup (top), scanning electron microscopy (SEM) images of cold-sprayed AgNWs on substrates for different preheating temperature (left), and numerical simulation results obtained by setting different impact velocities of AgNWs (right). c) Photograph of a wrinkled AgNW film and snapshots of an AgNW film in a stretching test. a–c) Reproduced with permission.^[85] Copyright 2016, Wiley-VCH.

dried rGO flakes with polymer solutions was demonstrated to produce a firm rGO membrane held together by highly entangled polymer nanofibers (see Figure 11a,b).^[106] Nylon 6 dissolved in formic acid (concentration = 15 wt%) was used as the polymer solution. The rGO powder and the nylon 6 solution were separately supplied to the supersonic air-stream by a powder feeder and a syringe pump, respectively (see Figure 11a and Table 4; cf. Table 1). As the rGO flakes were deposited on a substrate, the viscoelastic spinnable nylon 6 solution supplied to the supersonic stream underwent ultrahigh stretching that

allowed the spun nanofibers to lock the dried rGO flakes in place effectively and securely, without any additional binders.

Cold spraying was not only employed for coating rGO but also for graphene quantum dots (GQDs).^[107] These are a type of carbon dots (CD) that is known to possess better crystallinity than other inorganic CDs.^[108] Unlike 2D graphene, GQDs are recognized as a 0D material with size-tunable bandgaps owing to their unique sp²- and sp³-hybridized carbon atom structure.^[109] Because GQDs have shown highly favorable properties, such as stability, low toxicity, and bright

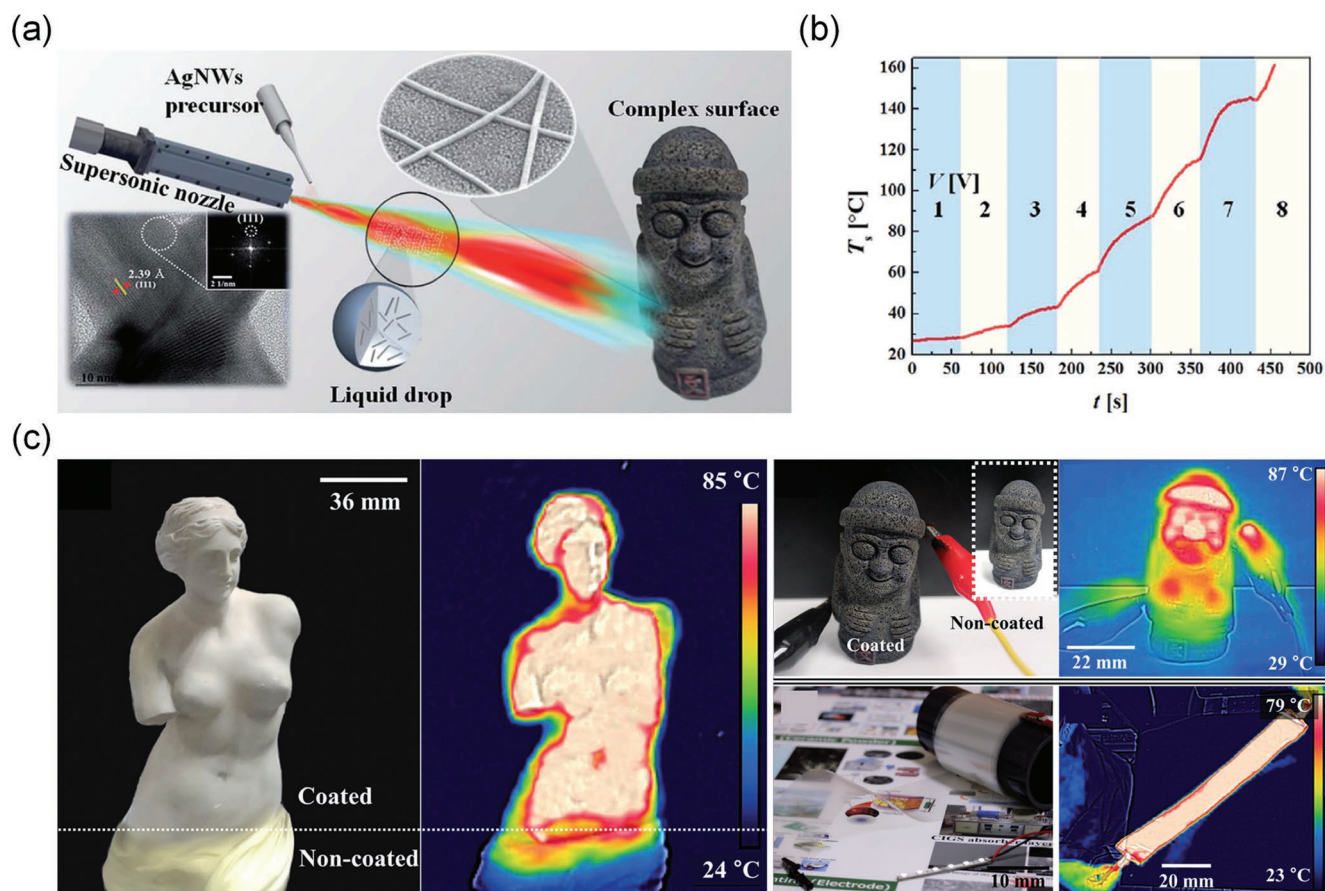


Figure 8. a) Schematic of the cold spraying method using an ultrasonic atomizer for an AgNW suspension. b) Variation in heating temperature of an AgNW film with varying applied voltages. c) Photographs and IR images of AgNWs deposited on various complex surfaces and large flexible substrates. a–c) Reproduced with permission.^[86] Copyright 2017, Royal Society of Chemistry.

Table 4. Summary of studies of cold spraying of nanoscale carbon materials. Note that only the results of experimental studies are listed.

| Material | Carrier gas | | | Coating material | | | Nozzle-to-substrate distance [mm] | Application ^{a)} | Refs. |
|----------|----------------|-----------------------------|--|---|--------------------|----------------------------|-----------------------------------|---------------------------|-------|
| | Pressure [MPa] | Preheating temperature [°C] | Max exit velocity [m s ⁻¹] | Material ^{a)} | Type ^{a)} | Feed rate | | | |
| Air | 0.6 | 350 | – | rGO (dispersed in ethanol, toluene, MEK, BCA) | Suspension | 10–20 mL min ⁻¹ | 60 | TCF | [91] |
| Air | 0.4 | 250 | – | rGO (dispersed in IPA, DMF) | Suspension | 6 mL min ⁻¹ | 90 | Cooling | [102] |
| Air | 0.6 | 350 | – | rGO (dispersed in DMF) | Suspension | 10–20 mL min ⁻¹ | 60 | Cooling | [103] |
| Air | 0.4 | 300 | – | rGO (dispersed in IPA, DMF) | Suspension | 3.0 mL min ⁻¹ | – | Anode (LIB) | [104] |
| Air | 0.3 | 200 | – | rGO | Powder (D: ≈25 μm) | 0.01 g min ⁻¹ | 70 | Water purification | [106] |
| Air | 0.3–0.5 | 220 | – | Nylon 6 (dissolved in FA, cf. Table 6) | Solution (15 wt%) | 0.6 mL min ⁻¹ | – | GQD layer (solar cell) | [107] |
| Air | 0.3–0.5 | 220 | – | GQDs (dispersed in water) | Suspension | 1 mL s ⁻¹ | – | GQD layer (solar cell) | [107] |

^{a)}rGO, reduced graphene oxide; MEK, methylethyl ketone; BCA, butyl carbitol acetate; TCF, transparent conducting film; IPA, isopropyl alcohol; DMF, dimethylformamide; LIB, lithium-ion battery; D, diameter, FA, formic acid, GQDs, graphene quantum dots.

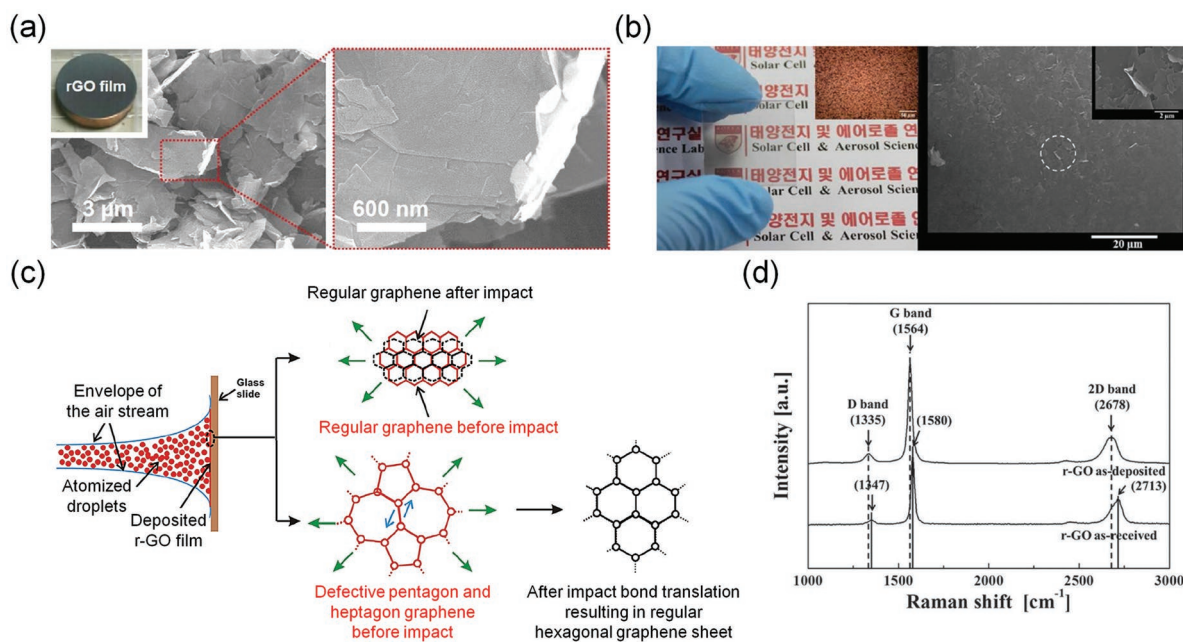


Figure 9. a) Scanning electron microscopy (SEM) images of cold-sprayed rGO on a Cu substrate. b) Photograph and corresponding SEM image of cold-sprayed rGO. The inset SEM image shows an enlarged view of the dashed circle area. c) Schematic of the self-healing phenomenon during cold spraying of rGO. d) Raman spectra of bare rGO and cold-sprayed rGO. a) Reproduced with permission.^[102] Copyright 2016, Elsevier. b–d) Reproduced with permission.^[91] Copyright 2014, Wiley-VCH.

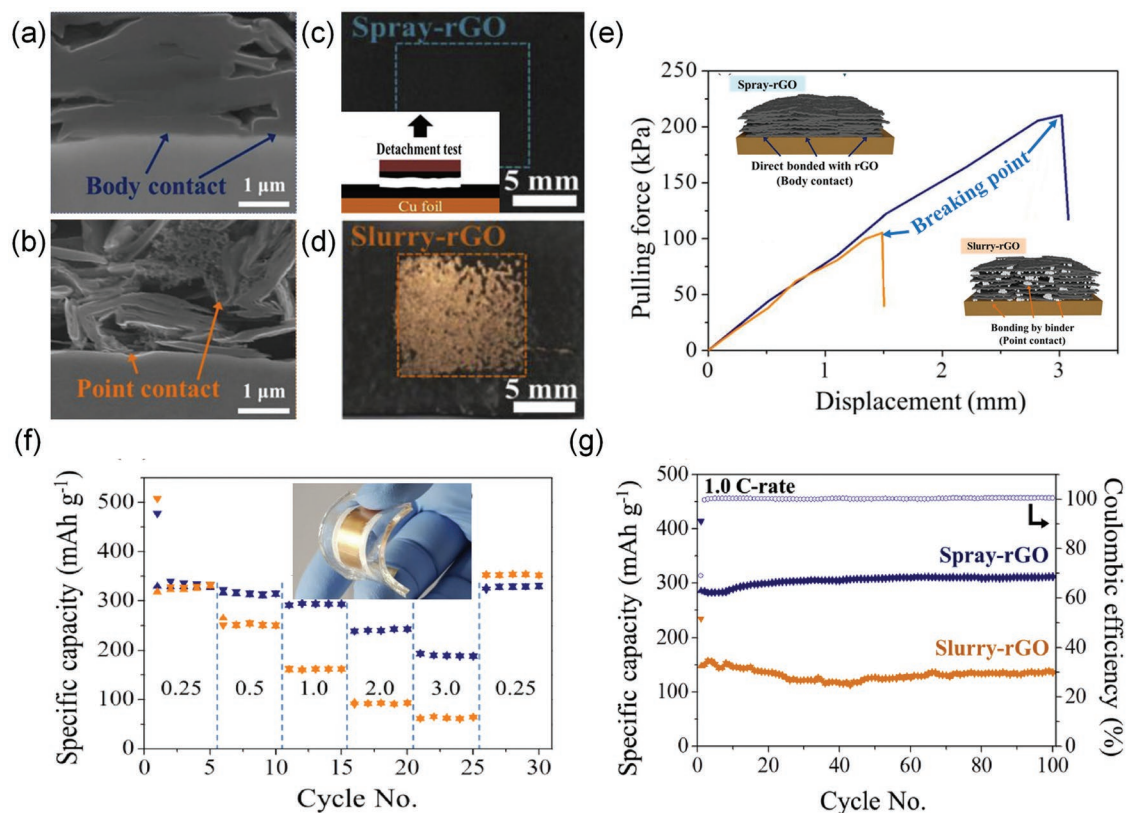


Figure 10. a,b) Cross-sectional scanning electron microscopy (SEM) images of cold-sprayed (a) and slurry-deposited (b) rGO films. c,d) Optical images of the corresponding specimens after adhesion tests. e) Results of adhesion measurements (insets indicate the deposition structures in each case). f) Rate capability of cold-sprayed and slurry-deposited rGOs (inset shows a flexible LIB with cold-sprayed rGO). g) Cycle performance of cold-sprayed and slurry-deposited rGOs. Note that blue and orange lines in (e–g) are results for cold-sprayed and slurry-deposited rGO, respectively. a–g) Reproduced with permission.^[104] Copyright 2018, Elsevier.

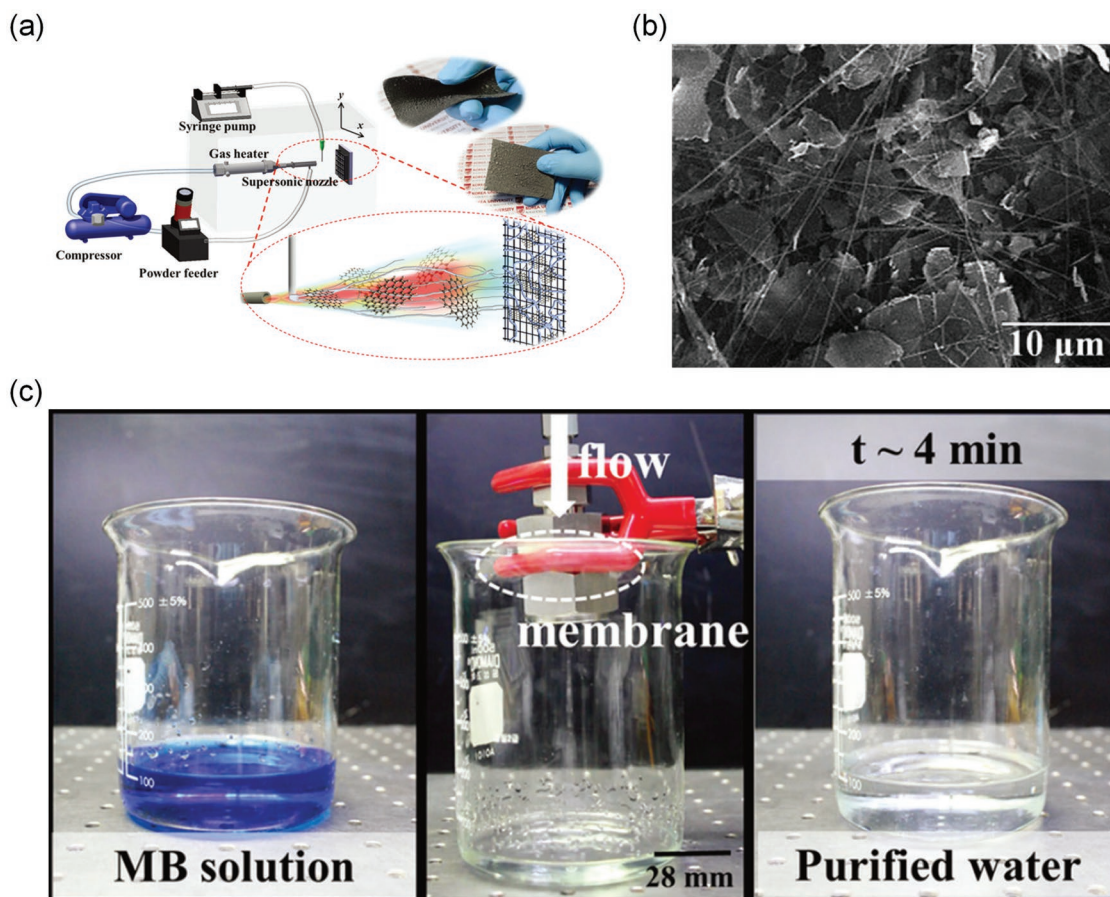


Figure 11. a) Schematic of cold spraying for a rGO–nylon composite. b) Scanning electron microscopy (SEM) image of cold-sprayed rGO–nylon membrane. c) Photographs showing the decoloration (or purification) process of a MB (methylene blue) solution by an rGO–nylon membrane. a–c) Reproduced with permission.^[106] Copyright 2015, Royal Society of Chemistry.

photoluminescence, they have attracted significant attention in relation to potential use in various applications, especially optoelectronic devices. GQDs were synthesized from rGO (prepared using a modified Hummer's method) by treatment with nitric and sulfuric acids, followed by extensive washing.^[107] Then, the GQD suspension was cold-sprayed under fixed operating conditions while varying the nozzle scan speed (cf. Tables 1 and 4), to produce GQD layers of different thicknesses. An ultrasonic atomizer was used to produce minute GQD droplets. During cold spraying, the atomized GQD suspension was rapidly evaporated and dispersed in the supersonic air-stream, reducing aggregation of the GQDs and producing a uniform GQD layer on the substrate. Accordingly, the GQDs could be deposited on the hydrophilic surface of a crystalline silicon (c-Si) solar cell without any damage to the surface.

2.4. Nanoscale Ceramic Coatings

Semiconducting ceramics, which are mostly composed of transition metal oxides, such as zinc oxide (ZnO) and indium tin oxide (ITO), have undergone significant development and found numerous practical applications since the late twentieth century, because of their outstanding optoelectronic and piezoelectric

properties.^[110–113] Among them, copper oxide (Cu_2O) and cupric oxide (CuO) have been widely studied for various optoelectronic applications in photovoltaic devices,^[114–116] secondary batteries,^[117,118] and sensors^[119] because of their low toxicity and low cost. The bandgap of CuO (0.7–1.6 eV) is significantly lower than that of Cu_2O (2.0–2.2 eV), leading to a much higher absorbance coefficient at visible wavelengths.^[120] Given the advantages of CuO , researchers have reported various fabrication methods of CuO films including sputtering,^[121] spin coating,^[122,123] direct anodization,^[124] physical vapor deposition (PVD),^[125] and hybrid microwave annealing.^[116]

The cold spraying technique was recently employed to produce high-surface-area CuO films, focusing on their potential use as a photocathode for photoelectrochemical (PEC) water splitting (Figures 12 and 13, and cf. Section 3.1.6). In this process, Cu_2O particles with an average diameter of $<1 \mu\text{m}$ were deposited onto an ITO substrate without any binders (cf. Tables 1 and 5).^[126] The Cu_2O films were subsequently annealed at 400–600 °C to convert them to CuO films. The dry Cu_2O particles were ball-milled before cold spraying because large particles are not efficiently accelerated by the supersonic flow. Cu_2O films of different thicknesses (ranging 1–3 μm) were obtained by varying the number of sweeps of the supersonic nozzle with a fixed scan speed of 10 mm s^{-1} . The

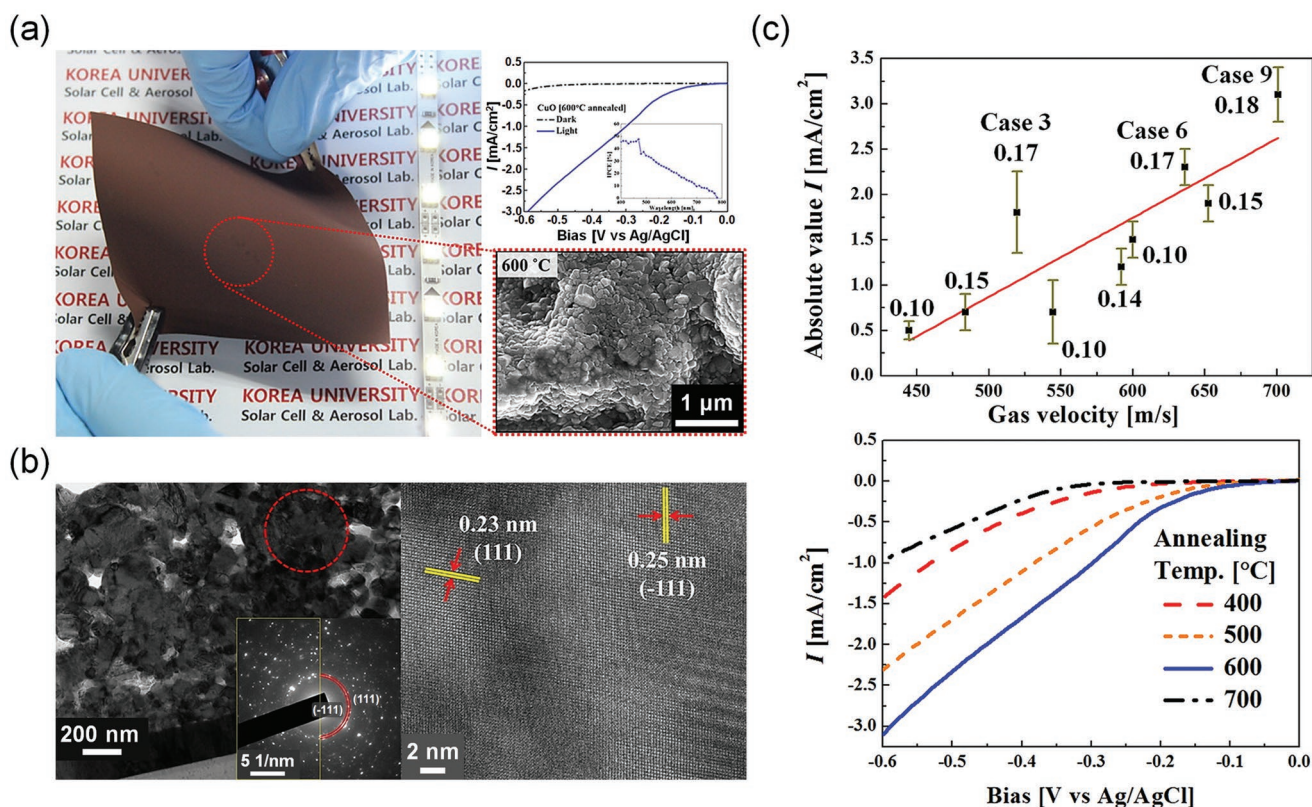


Figure 12. Cold-sprayed CuO films after annealing: a) photograph, scanning electron microscopy (SEM) image, and results of the PEC water splitting test. b) Transmission electron microscopy (TEM) images and c) results of the PEC water splitting tests with different annealing temperatures. a–c) Reproduced with permission.^[126] Copyright 2016, American Chemical Society.

cold-sprayed particles were pulverized upon impact, which led to in situ sintering between adjacent particles that produced a self-assembled unique honeycomb structure.

The potential of the cold spraying as an industrially scalable fabrication process for photoanode materials was also demonstrated recently (Figures 12 and 13, and cf. Section 3.1.6).^[127] For example, to deposit Fe₂O₃ particles, a colloidal suspension of Fe₂O₃ was prepared by mixing it with viscoelastic polyacrylonitrile (PAN)/dimethylformamide (DMF) solutions. Then, the suspension was atomized into the supersonic air-stream under fixed conditions (Tables 1 and 5) and deposited onto an ITO substrate. Note that additional annealing was conducted at 500 °C for 120 min to remove impurities in the deposited Fe₂O₃ film. Atomic layer deposition (ALD) of ZnO and titanium dioxide (TiO₂) on the surface of the annealed hematite (Fe₂O₃) layer was also employed to form passivation layers, highlighting the compatibility of cold-sprayed materials with other coating methods.

Using a cold-spraying system equipped with an atomizer, an ultrathin thermally insulating layer composed of silicon dioxide (SiO₂) was fabricated with a thickness of 1.1 μm (Tables 1 and 5).^[87] For this, a SiO₂ suspension was prepared by dispersing SiO₂ nanoparticles (with an average diameter of 15 nm) in a viscoelastic PAN/DMF solution, which was then atomized into the supersonic air-stream. This was deposited onto the surface of cold-sprayed AgNWs and covered by a subsequent cold-sprayed PS (polystyrene) layer (cf. Section 2.5). Not only could the SiO₂ be readily clustered by cold spraying,

but minute pores were also created between the clusters, which contributed to good thermal insulation performance.

In addition to the deposition of QDs as described in Section 2.3, lead (II) sulfide (PbS) QD films were produced via the cold spraying technique (Tables 1 and 5).^[128] For this, a PbS QD suspension was prepared by a ligand-exchange process,^[129] then injected into the supersonic air-stream through an ultrasonic atomizer. The high kinetic energy of the supersonic air-stream facilitated the secondary fragmentation of the PbS QDs with rapid evaporation of the solvent. This meant that completely dry PbS QDs were deposited onto the TiO₂ substrate. The one-step cold spraying deposition allowed production of high-quality n-type PbS QD films with a thickness of 300 nm over an area of 2.5 cm × 2.5 cm, within tens of seconds, and without any thermal post-treatment for solvent removal, as required by other methods.

2.5. Polymer Coatings

Polymer fibers, including those composed of both natural and synthetic materials, are essential for many modern technologies, from everyday clothes to various state-of-the-art smart materials.^[130–135] Accordingly, numerous fiber-forming methods, such as electrospinning, solution blowing, meltblowing, wet spinning, and force spinning, have been actively studied and widely employed in both academia and industry to fabricate various macro-, micro-, and nanoscopic polymer fibers.^[131]

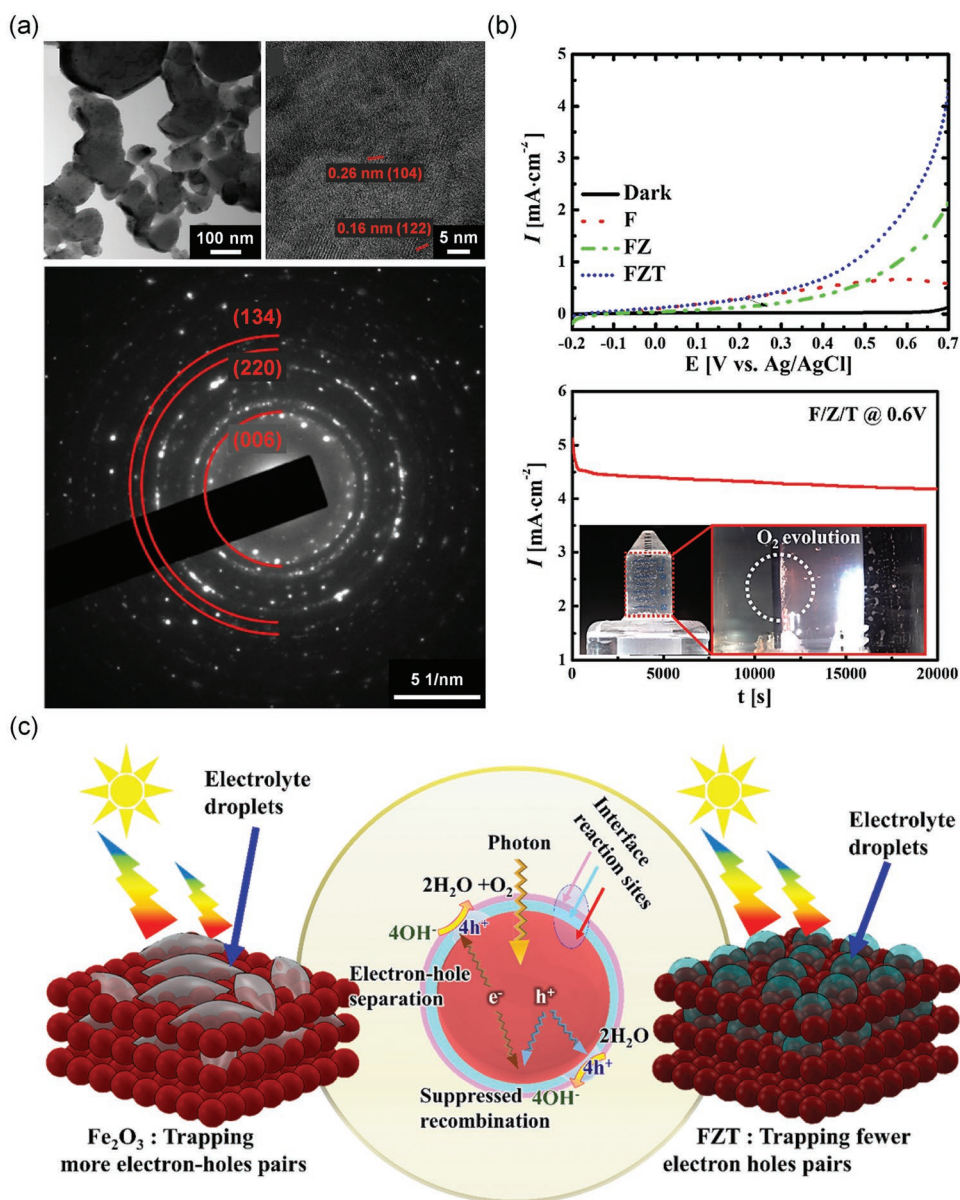


Figure 13. Cold-sprayed Fe₂O₃ photoanode passivated by ALD of ZnO and TiO₂. a) Transmission electron microscopy (TEM) images and selected area electron diffraction (SAED) pattern. b) Results of PEC water splitting tests and c) the working mechanism as a photoanode. a–c) Reproduced with permission.^[127] Copyright 2019, Elsevier.

In 2013, the feasibility of supersonic spraying (or blowing) systems for fabricating ultrathin polymer nanofibers was demonstrated (Figure 14, Tables 1 and 6).^[136] The supersonic flow accelerated by a converging-diverging de Laval nozzle enabled the polymer solution jet (entrained into the supersonic jet by an electric force) to be aerodynamically stretched and bent and solidified (see Figure 14b), thereby forming polymer nanofibers with a diameter of less than 50 nm (Figure 14c).^[136,137] In contrast to the solution-blowing approach, which is driven by subsonic blowing, supersonic nanoblowing produced polymer fibers with ultrathin diameters that are unattainable by solution blowing and electrospinning. In experiments using nylon 6 solution, the strong thinning and stretching by an extremely high aerodynamic effect (with a stretching ratio in the order

of 10⁷–10¹⁰) caused the macromolecular sheets in the nylon 6 nanofibers to be tightly rearranged. This resulted in significantly enhanced hydrogen bonding and, thus, yielded a new phase of nylon 6—the χ -phase.^[136]

In subsequent work, supersonically blown nylon 6 nanofibers (described in Section 2.3) were used to lock in place otherwise easily separated rGO flakes (Figure 11, Tables 4 and 6).^[106] Unlike the electrically assisted supersonic blowing performed by Sinha-Ray et al.^[136] and An et al.,^[137] the polymer solution jet used in ref. [106] could be entrained into the supersonic flow without applying an electric force. This was achieved by applying a high pumping force in the syringe pump (Figure 11a), which resulted in a higher flow rate ($Q = 0.6 \text{ mL min}^{-1}$) than in the electrically assisted case (see Table 6). In other words, the high

Table 5. Summary of studies of cold spraying of nanoscale ceramic coatings. Note that only results based on experimental studies are listed.

| Material | Experimental parameter | | | | | | Application ^{a)} | Refs. | |
|----------------|-----------------------------|--|------------------------|---|----------------------|-----------------------------------|---------------------------|------------------------------------|-------|
| | Carrier gas | | | Coating material | | Nozzle-to-substrate distance [mm] | | | |
| Pressure [MPa] | Preheating temperature [°C] | Max exit velocity [m s ⁻¹] | Material ^{a)} | Type ^{a)} | Feed rate | | | | |
| Air | 0.2–0.4 | 250–450 | 553–829 | Cu ₂ O | Powder (D: ≈1 μm) | – | 50 | Photocathode (PEC water splitting) | [126] |
| Air | 0.4 | 220 | – | AgNW (dispersed in IPA, cf. Table 3) | Suspension | 1.2 mL min ⁻¹ | 200 | Self-cleaning | [87] |
| | 0.4 | 250 | – | SiO ₂ (dispersed in PAN–DMF) | | 1.5 mL min ⁻¹ | | | |
| | 0.3 | 350 | – | PS (dissolved in DMF, cf. Table 6) | Solution (0.11 wt%) | 1.2 mL min ⁻¹ | | | |
| Air | 0.4 | 250 | – | Fe ₂ O ₃ (dispersed in PAN–DMF) | Suspension | 1.5 mL min ⁻¹ | – | Photoanode (PEC water splitting) | [127] |
| Air | 0.4 | 250 | – | PbS QDs (dispersed in PC) | Suspension | 2 mL min ⁻¹ | – | Solar cell | [128] |

^{a)}Cu₂O, cuprous oxide; D, diameter; PEC, photoelectrochemical; AgNW, silver nanowire; IPA, isopropyl alcohol; SiO₂, silicon dioxide; PAN, polyacrylonitrile; DMF, dimethylformamide; PS, polystyrene; Fe₂O₃, hematite; PbS, lead(II) sulfide quantum dots; PC, propylene carbonate.

momentum of the polymer solution jet allowed the issued solution to enter the supersonic jet.

In addition to forming nonwoven polymer nanofibers via the cold spraying method, a thin polymer layer was fabricated by manipulating the operating conditions and the concentration of the polymer solution (Figure 15, and Tables 1 and 6).^[87] Contrary to other studies on cold spraying polymers (see Table 6), the operating (or stagnation) pressure was reduced from 0.6 to 0.3 MPa to attenuate the kinetic energy of the supersonic jet^[34] and polymer concentration was reduced to 0.11 wt% to decrease the elastic forces and thus, spinnability (see Table 6). This facilitated formation of a thin polymer layer by preventing fiber formation. As a result, a

uniformly deposited thin PS layer (thickness = 0.5 μm) could be achieved which, owing to its high water contact angle of 120°, was explored for self-cleaning applications (Section 3.2.1).

2.6. Nanoscale Hybrid Material Coatings

There have been several studies on the fabrication of hybrid coatings from different types of materials. However, these studies have tended to either employ micrometer-scale materials with sizes on the order of 1 to 10 μm or have mainly focused on their mechanical properties without discussing applications.^[138–144]

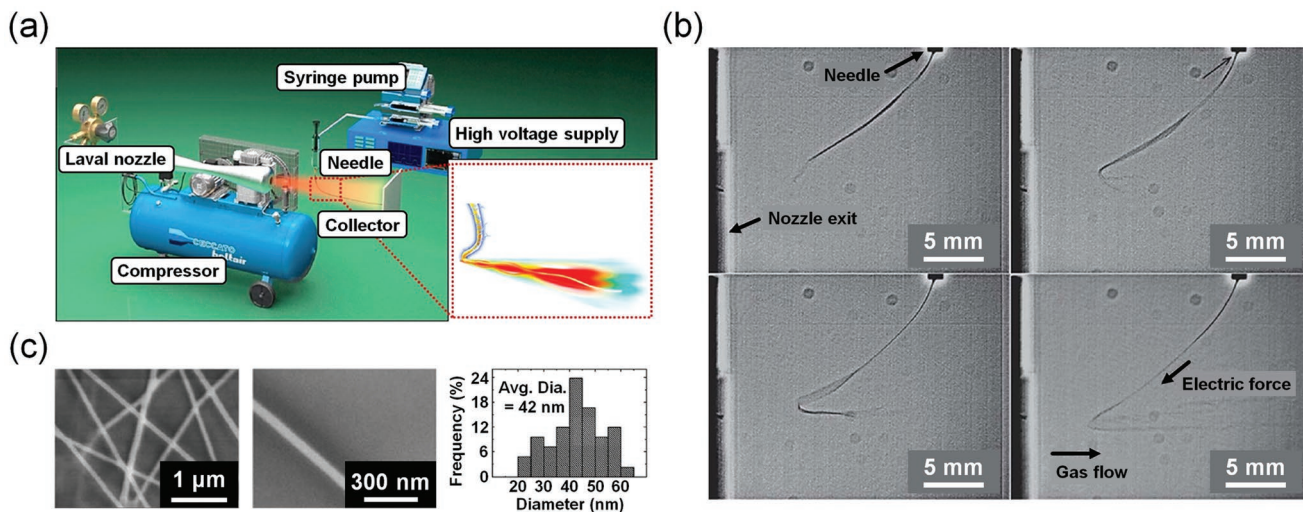


Figure 14. a) Schematic of the supersonic nano-blowing setup. The inset image indicates polymer solution jet bending and stretching in the supersonic air flow. b) Snapshots from a high-speed camera, taken when a nylon 6 solution jet was electrically issued from the needle and attracted to the exit of the de Laval nozzle by the electric force, thereby being entrained into the supersonic air stream. c) Scanning electron microscopy (SEM) images indicating the fiber distribution resulting from the supersonic blowing of nylon 6 fibers. a) Reproduced with permission.^[137] Copyright 2014, American Chemical Society. b,c) Reproduced with permission.^[136] Copyright 2013, Royal Society of Chemistry.

Table 6. Summary of studies of cold spraying of polymer coatings. Note that only results based on experimental studies are listed.

| Material | Carrier gas | | | Coating material | | | Nozzle-to-substrate distance [mm] | Application | Refs. |
|----------|----------------|---|--|--|--|------------------------------|-----------------------------------|--------------------|-------|
| | Pressure [MPa] | Preheating temperature ^{a)} [°C] | Max exit velocity [m s ⁻¹] | Material ^{a)} | Type | Feed rate | | | |
| Air | 0.6 | RT | 558 | Nylon 6 (dissolved in FA) | Solution (15 wt%) | 100–200 $\mu\text{L h}^{-1}$ | 235 | – | [136] |
| Air | 0.6 | 30 | 470 | PAN (dissolved in DMF) | Solution (6 wt%) | 150 $\mu\text{L h}^{-1}$ | 100 | Cooling | [137] |
| Air | 0.3 | 200 | 933 | rGO (cf. Table 4) | Powder ($D: \approx 25 \mu\text{m}$) | 0.01 g min^{-1} | 70 | Water purification | [106] |
| Air | 0.4 | 220 | – | AgNW (dispersed in IPA, cf. Table 3) | Suspension | 1.2 mL min^{-1} | 200 | Self-cleaning | [87] |
| | 0.4 | 250 | – | SiO ₂ (dispersed in PAN-DMF, cf. Table 5) | | 1.5 mL min^{-1} | | | |
| | 0.3 | 350 | – | PS (dissolved in DMF) | Solution (0.11 wt%) | 1.2 mL min^{-1} | | | |

^{a)}RT, room temperature; FA, formic acid; PAN, polyacrylonitrile; DMF, dimethylformamide; AgNW, silver nanowire; IPA, isopropyl alcohol; SiO₂, silicon dioxide; PS, polystyrene.

There have also been studies of the energy-related applications of these hybrid nanomaterial films, yet most depended on vacuum-based cold spraying techniques.^[145] Such vacuum-based methods are less suitable for energy and environmental applications—which require ultrathin materials produced by fast, cost-effective, and scalable methods—and are not discussed in this review.

The cold spraying method with a polymer–ceramic mixed material was employed to develop self-cleaning superhydrophobic films with tunable wettability (Table 7 and

cf. Section 3.2.1).^[146] Kim et al.^[146] reported preparation of polytetrafluoroethylene (PTFE)–titania (TiO₂) powders in different proportions by mixing them in a fluidized mixer, where the average diameters of PTFE and TiO₂ were 1 μm and 21 nm, respectively. The mixed hybrid sub-micrometer powder was deposited onto glass and stainless-steel mesh substrates by cold spraying (cf. Tables 1 and 7). The resulting PTFE film exhibited superhydrophobicity but became less hydrophobic (more hydrophilic) as the TiO₂ content in the mixed powder increased.

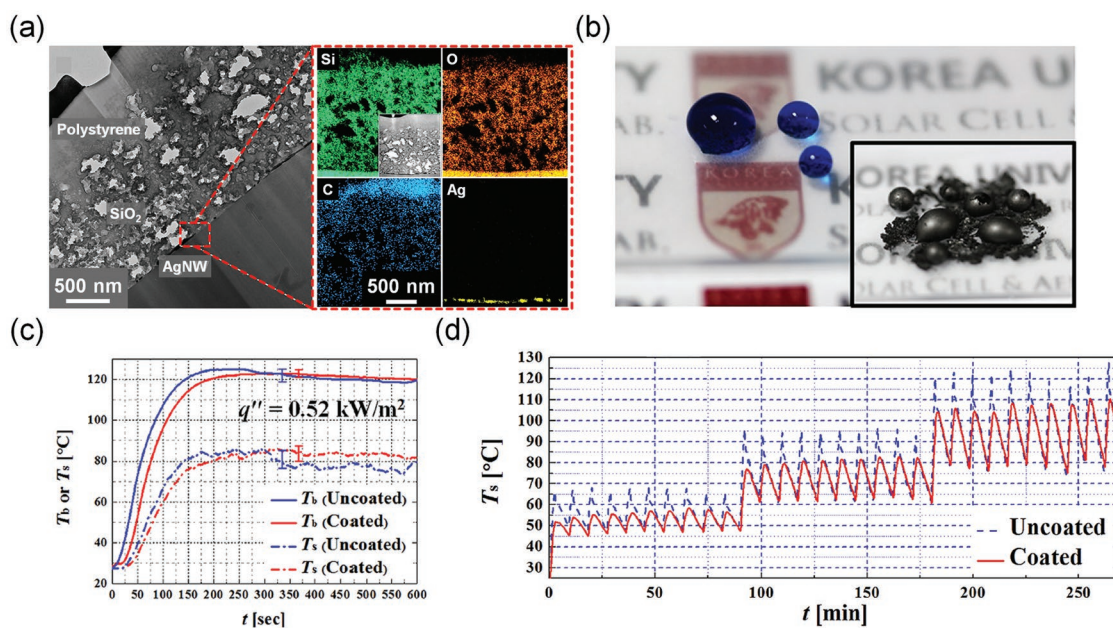


Figure 15. a) Transmission electron microscopy (TEM) image and corresponding elemental mapping images of an AgNW/SiO₂/PS film. b) Photograph of an AgNW/SiO₂/PS film with droplets on the surface. c) Time-dependent temperature variation on the bottom (T_b) and top surfaces (T_s) of an AgNW/SiO₂/PS film when the heat flux of $q'' = 0.52 \text{ kW m}^{-2}$ was applied. d) Cycle testing of an AgNW/SiO₂/PS film as a heater, where “Uncoated” indicates the film without SiO₂ and PS layers, and “Coated” corresponds to the complete AgNW/SiO₂/PS film. a–d) Reproduced with permission.^[87] Copyright 2017, American Chemical Society.

Table 7. Summary of studies of cold spraying of nanoscale hybrid material coatings. Note that only results of experimental studies are listed.

| Material | Carrier gas | | | Coating material | | | Nozzle-to-substrate distance [mm] | Application ^{a)} | Refs. |
|----------|----------------|-----------------------------|---|---|------------|--------------------------|-----------------------------------|---------------------------|-------|
| | Pressure [MPa] | Preheating temperature [°C] | Max exit velocity [m s ⁻¹] | Material ^{a)} | Type | Feed rate | | | |
| Air | 0.6 | 400 | – | PTFE–TiO ₂ | Powder | – | – | Self-cleaning film | [146] |
| Air | 0.4 | 247 | – | Kaolinite, bentonite, montmorillonite (dispersed in nylon-IPA) | Suspension | 3 mL min ⁻¹ | 90 | TBC, electrical insulator | [147] |
| | | | | | | | | | |
| Air | 0.2 | 250 | – | Montmorillonite (dispersed in nylon-IPA) | Suspension | 3 mL min ⁻¹ | 50 | TBC, electrical insulator | [149] |
| | | | Montmorillonite-SiO ₂ (dispersed in nylon-IPA) | | | | | | |
| | | | Montmorillonite-silica aerogel (dispersed in nylon-IPA) | | | | | | |
| Air | 0.4 | 250 | – | TiO ₂ -rGO (dispersed in PAN-DMF) | Suspension | 1.5 mL min ⁻¹ | 70 | Anode (LIB) | [153] |
| Air | 0.4 | 250 | – | Fe ₂ O ₃ -rGO (dispersed in PAN-DMF) | Suspension | 1.5 mL min ⁻¹ | – | Anode (LIB) | [154] |
| Air | 0.4 | 250 | – | Zn ₂ SnO ₄ -SnO ₂ -rGO (dispersed in PAN-DMF) | Suspension | 1.5 mL min ⁻¹ | 130 | Anode (LIB) | [155] |
| Air | 0.4 | 250 | – | rGO-Fe(C ₅ H ₇ O ₂) ₃ (dispersed in PAN-DMF) | Suspension | 2.4 mL min ⁻¹ | 70 | Anode (LIB) | [156] |
| | | | | Fe(C ₅ H ₇ O ₂) ₃ (dissolved in PAN-DMF) | | 0.8 mL min ⁻¹ | | | |
| Air | 0.4 | 250 | – | ZFCN (dispersed in PAN-DMF) | Suspension | 1.5 mL min ⁻¹ | 175 | Anode (LIB) | [158] |
| Air | 0.2–0.7 | 150–350 | 400–800 | ZIF-8 (dispersed in nylon-IPA, DMF) | Suspension | – | – | Multipurpose | [162] |
| Air | 0.2–0.7 | 150–450 | – | ZIF-7 (dispersed in nylon-IPA, DMF) | Suspension | – | – | Multipurpose | [163] |
| Air | 0.2, 0.4, 0.6 | 250 | 445, 600, 664 | MIL-100 (dispersed in PAN-DMF) | Suspension | 1.5 mL min ⁻¹ | 200 | Multipurpose | [164] |

^{a)}PTFE, poly(tetrafluoroethylene); TiO₂, titanium dioxide (titania); IPA, isopropyl alcohol; TBC, thermal barrier coating; PAN, polyacrylonitrile; DMF, dimethylformamide; LIB, lithium-ion battery; Fe₂O₃, hematite; rGO, reduced graphene oxide, Zn₂SnO₄, zinc stannate; Fe(C₅H₇O₂), iron(III) acetylacetonate; ZFCN, graphitic carbon nitride (g-CN) nanosheets hosting ZnFe₂O₄ nanoparticles; ZIF, zeolitic imidazolate framework; MIL, Materials of Institute Lavoisier.

Cold spraying of clay and clay minerals has recently been employed to produce thermally and electrically insulating nanomaterial films (cf. Section 3.1.3), (Tables 1 and 7).^[147,148] For example, bentonite (clay) and kaolinite and montmorillonite (clay minerals) dispersed in a nylon solution were cold-sprayed onto substrates (Figure 16). The use of a viscoelastic polymer solution improved the dispersion of clay within the suspension as well as the uniformity of the cold-sprayed clay layer on the substrate. The suspension, supplied by a separate syringe pump (flow rate = 3 mL min⁻¹), was atomized into the supersonic air-stream using an ultrasonic atomizer (see Figure 16a). This contributed to rapid evaporation of the polymer solution and prevented the aggregation of clay particles. Subsequently, insulating montmorillonite layers reinforced with SiO₂ and silica aerogel were also developed, and their thermally and electrically

insulating performance was explored (Section 3.1.3).^[149] These hybrid materials could be deposited on both rigid stainless-steel and flexible PET substrates by cold spraying (Figure 16d). The mixing of montmorillonite and silica aerogel not only improved the performance of the resulting layers in terms of thermal insulation, but also increased adhesion between the microscale aerogel particles (10–100 μm) and the substrate. This prevented particle detachment from the substrate that may otherwise result from the sharp and irregular shape of the silica aerogel.

Inspired by the economic feasibility of rGO, with its properties comparable to pure graphene, rGO has been studied for numerous applications (cf. Section 2.3).^[90] Although rGO has generally been used alone (cf. Section 2.3), combining rGO with other materials has also been explored as a means of improving properties, such as ion diffusion capacity and

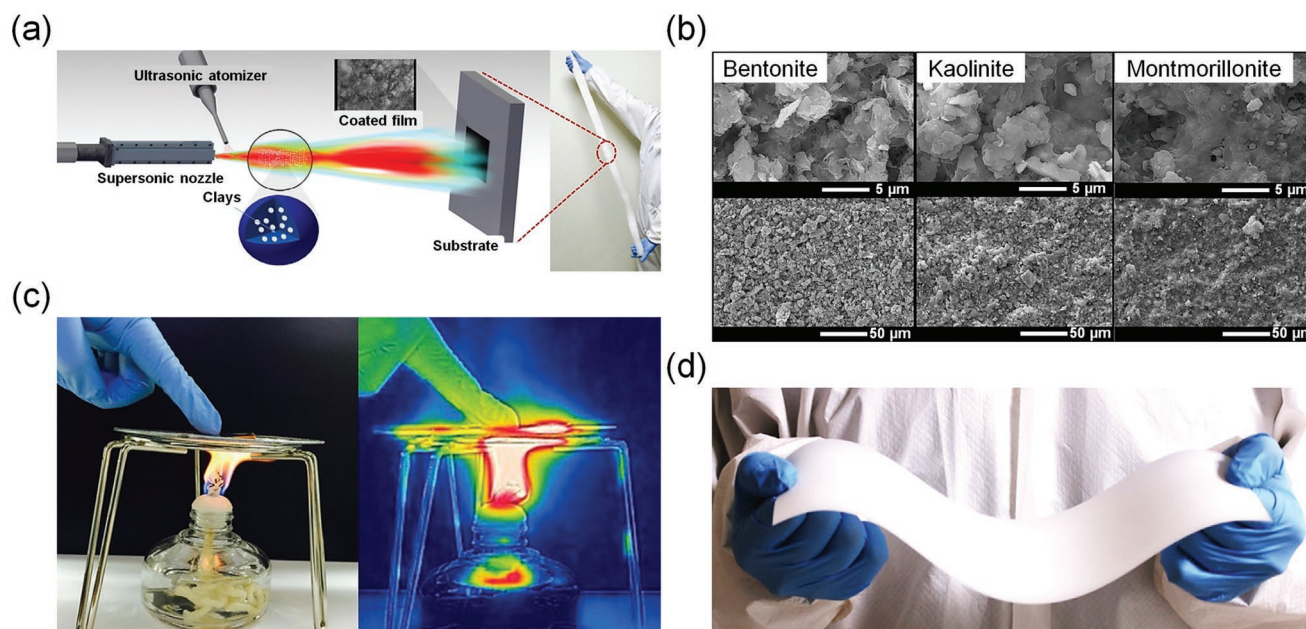


Figure 16. a) Schematic of cold spraying of clay (bentonite) and clay minerals (kaolinite and montmorillonite). b) Scanning electron microscopy (SEM) images of cold-sprayed clay and clay minerals. c) Thermal insulation test of a cold-sprayed montmorillonite layer (deposited on a Cu film) with thickness of 1 mm, wherein the flame from the lamp was ≈ 700 °C. d) Photograph of a large-scale thermally insulating film consisting of montmorillonite and aerogel fabricated by cold spraying. a,c) Reproduced with permission.^[147] Copyright 2016, Elsevier. b) Reproduced with permission.^[148] Copyright 2016, Springer Nature. d) Reproduced with permission.^[149] Copyright 2018, Elsevier.

electron conductivity.^[150–152] For example, hybrid rGO/TiO₂ films were formed using the cold spraying method (Tables 1 and 7) focusing on their potential use as anode materials for lithium-ion batteries (LIBs, cf. **Figure 17** and Section 3.1.5).^[153] In the latter work, the proportions of rGO and TiO₂ were varied by mixing them with a viscoelastic PAN/DMF solution. Although the suspension was sonicated to achieve sufficient dispersion, as the freshly mixed suspension was metastable, a short sonication time was employed (less than a few minutes) to prevent damage to rGO flakes and TiO₂ particles, and especially to the PAN macromolecules. The use of cold spraying reinforced the interfacial electrochemical activity between rGO and TiO₂, and this effect was attributed to the strong adhesion driven by high impact energy upon the substrate.

In addition to the combination of rGO and TiO₂, fabrication of hybrid films using metal oxides such as iron (III) oxide (hematite, Fe₂O₃), zinc stannate (Zn₂SnO₄), and tin (IV) oxide (SnO₂) was also demonstrated. Then, rGO/Fe₂O₃ and rGO/Zn₂SnO₄/SnO₂ hybrid films were employed in LIB anodes (Figure 17, Table 7, and cf. Section 3.1.5).^[154,155] Similar to the fabrication of rGO/TiO₂ hybrid films,^[153] both the rGO/Fe₂O₃ and rGO/Zn₂SnO₄/SnO₂ films were obtained by using cold-sprayed mixed transition metal oxides (Fe₂O₃, Zn₂SnO₄, and SnO₂) with rGO and PAN/DMF solution (see Table 7). Because the solvent (DMF) was fully evaporated during the cold spraying process, the hybridized and dried metal oxides could be efficiently deposited on the substrates. The small amount of PAN (<1 wt% in comparison to metal oxides) in the as-deposited films was carbonized in the subsequent annealing process (conducted at 700 °C for 2 h in an Ar atmosphere), which also slightly enhanced the electrical

conductivity of the hybrid film and removed impurities. With the exception of the nozzle-to-substrate distance, the operating conditions for the cold spraying of different metal oxides mixed with rGO and PAN/DMF solution were the same in all cases (see Tables 1 and 7).

Joshi et al.^[156] reported fabrication of iron carbide (Fe₃C) films hybridized (entangled) with rGO using the cold spraying method (Table 7). In contrast to the above studies of rGO/TiO₂, rGO/Fe₂O₃, and rGO/Zn₂SnO₄/SnO₂ hybrid films, both the concentration and amount of PAN/DMF solution in the suspension were increased to obtain a fibrous structure rather than a thin layer (as described in Section 2.5 for polymer fibers). In this case, the cold spraying method facilitated the formation of nanofibers with a high rGO loading in contrast to typical fiber-forming processes, such as electrospinning and solution blowing,^[131,157] in which the incorporation of rGO is limited by the needle size and flow rate.

By using the cold spraying method, a high-capacity LIB anode composed of graphitic carbon nitride (g-CN) nanosheets hybridized with ZnFe₂O₄ nanoparticles (Tables 1 and 7, and cf. Section 3.1.5) was subsequently developed.^[158] Based on the fact that g-CN not only exhibits good ion adsorption and diffusion but is also chemically stable and nontoxic,^[159,160] g-CN was hybridized with one of the transition metal oxides (ZnFe₂O₄) that has a high theoretical capacity of 1072 mA h g⁻¹.^[161] The g-CN/ZnFe₂O₄ (ZFCN, cf. Table 7) was mixed with PAN/DMF solution to form a suspension. The latter was then deposited onto a Cu foil by cold spraying with an ultrasonic atomizer. The cold-sprayed films were annealed at different temperatures of 400, 450, 500, and 560 °C in Ar atmosphere to remove impurities and improve their electrochemical properties.

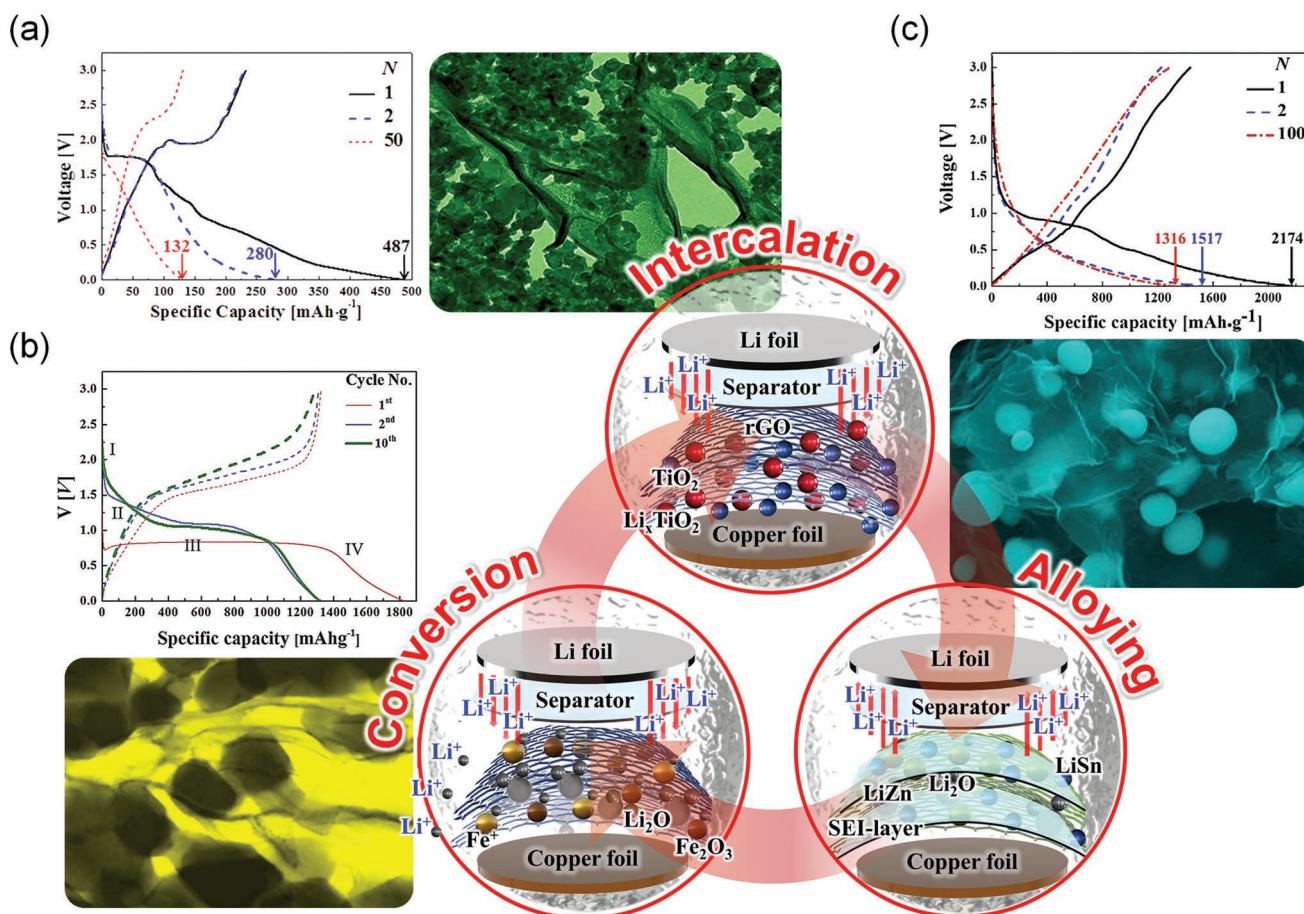


Figure 17. LIB performance and transmission electron microscopy (TEM) images of hybrid materials fabricated by the cold spraying technique: a) rGO/TiO₂ film, b) rGO/Fe₂O₃ film, and c) rGO/Zn₂SnO₄/SnO₂ film. Note that the central illustration depicts mechanisms pertaining to LIBs: a) intercalation, b) conversion, and c) alloying/dealloying. a) Reproduced with permission.^[153] Copyright 2017, Elsevier. b) Reproduced with permission.^[154] Copyright 2017, Elsevier. c) Reproduced with permission.^[155] Copyright 2018, Elsevier. The central scheme is adapted with permission.^[155] Copyright 2018, Elsevier.

Cold spraying can also be effective for the deposition of metal–organic frameworks (MOFs, see **Figure 18**, Tables 1 and 7, and cf. Section 3.2.2), such as zeolitic imidazolate frameworks (ZIF)-8,^[162] ZIF-7,^[163] and Materials of Institute Lavoisier (MIL)-100.^[164] Specifically, ZIF-8 nanoparticles with an average diameter of 150 nm, which were prepared by a microwave-irradiation method, were used to produce a colloidal suspension by mixing them with nylon 6 dissolved in IPA and DMF (Table 7).^[162] The use of viscoelastic nylon 6 solution promoted dispersion (in the suspension) and adhesion (onto the substrate) of ZIF-8 nanoparticles. Notably, large-area ZIF-8 films were fabricated with a roll-to-roll cold spraying system installed under open-air conditions, demonstrating that this one-step, scalable technique is an industrially viable method for the commercial production of MOF thin films. The deposition of ZIF-7^[163] was also explored via cold spraying. Note that ZIF-7 is distinct from ZIF-8 in terms of its hexagonal symmetry (Table 7 and cf. Section 3.2.2).^[165] Furthermore, the deposition of MIL-100 using the cold spraying method, which is one of the particular MOFs derived from trivalent metals linked with carboxylate ligands (Table 7 and cf. Section 3.2.2), has also been demonstrated.^[164] In this case, the iron-containing

MIL-100(Fe), which is known to have low toxicity and a particularly high water adsorption capacity, was investigated.^[166,167] As in the studies of ZIF-7 and ZIF-8,^[162,163] the MIL-100 nanoparticles were mixed with a viscoelastic polymer solution (PAN/DMF solution) and then cold-sprayed via atomization in a supersonic air-stream at velocities of 445–664 m s⁻¹. The atomized nanoparticles rapidly evaporated, resulting in the efficient deposition of MIL-100 nanoparticles onto solid glass substrates.

3. Applications of Supersonic Cold Spraying for Energy and Environmental Technologies

This section describes some of the potential applications of supersonic cold spraying with a focus on energy and environmental technologies. In contrast to existing bottom-up coating methods described in Sections 1 and 2, the cold spraying technique is capable of fabricating ultrathin items, i.e., films, filters, membranes, and electrodes, in a rapid, scalable, and cost-effective process. Therefore, this section introduces and details cold spraying studies for energy and environmental applications.

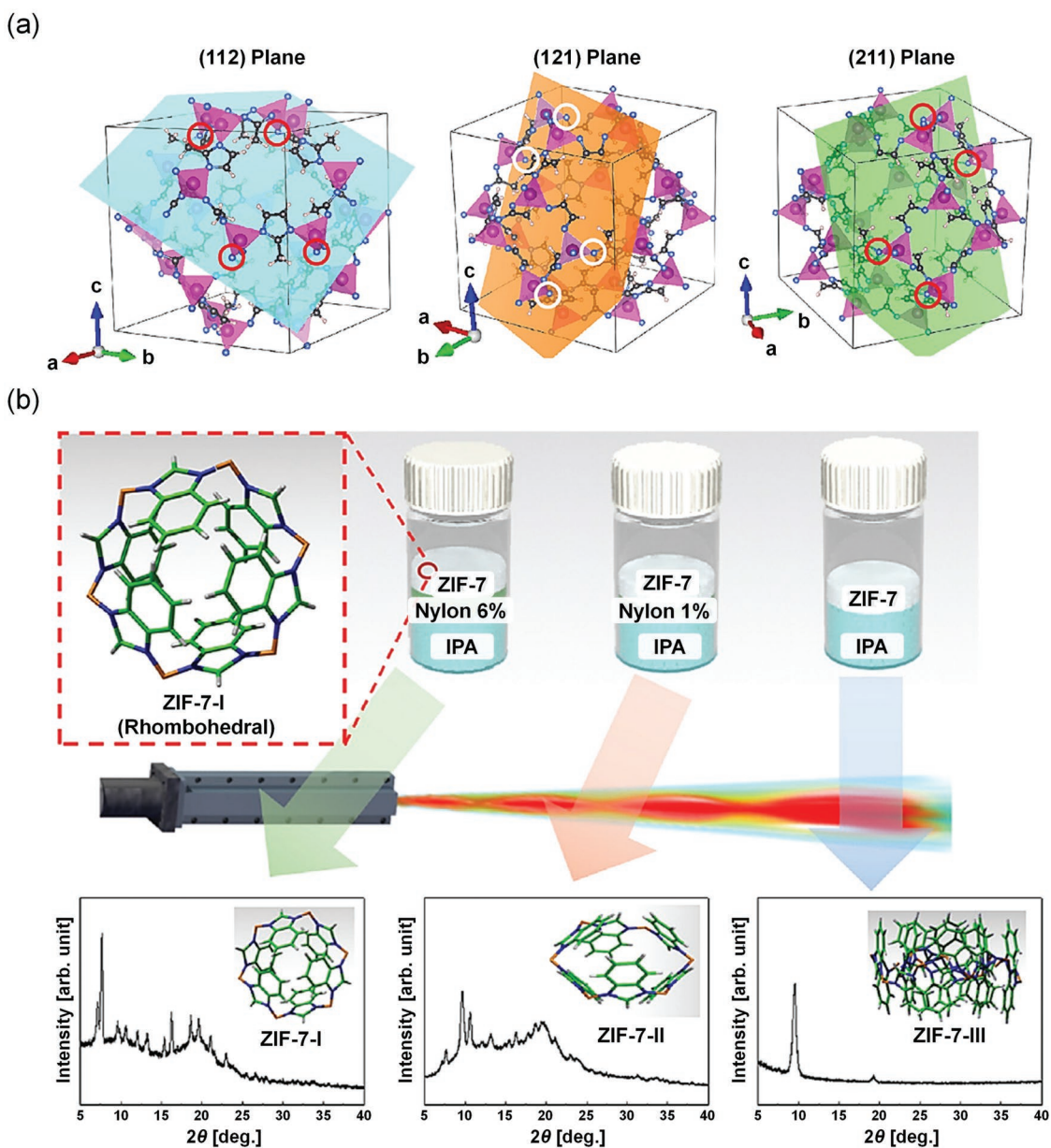


Figure 18. a) Illustrations of the potential cleavage planes of a ZIF-8 unit cell, which belong to the (112)-oriented family of lattice planes. Note that the purple tetrahedra indicate ZnN₄ and the corresponding circles represent weak points at the vertices of ZnN₄ prone to be ruptured by shear stresses. Purple: zinc, gray: carbon, blue: nitrogen, and white: hydrogen. b) Illustrations and XRD results for the change in the crystalline structure of cold-sprayed ZIF-7 films with varying concentrations of nylon solution. a) Reproduced with permission.^[162] Copyright 2016, Elsevier. b) Reproduced with permission.^[163] Copyright 2017, Elsevier.

3.1. Energy Applications

3.1.1. Electrodes and Films for Photovoltaic Solar Cells

As described in Sections 2.1 and 2.2, the potential of the cold spraying method for energy applications, primarily for solar cells, was explored. Cold-spraying of thin single-layer Cu lines onto Si wafers was demonstrated. These exhibited reasonable performance as front electrodes in Si solar cells (Table 3).^[62] Different widths of pyramid-shaped Cu electrodes were developed using a mask (Figure 5b,c), which yielded

acceptable conductivities with specific resistivity (R_{sp}) in the 0.009–0.013 Ω cm range.^[62] Cold-sprayed Cu electrodes deposited on a phosphorus-doped n-type emitter of a p-type Si wafer (Table 3 and cf. Section 2.2) were also reported.^[83] In this case, the electrical properties of Cu electrodes with different thicknesses were evaluated by a transfer length method (TLM). To prevent diffusion of Cu into the underlying Si wafer and to enhance the adhesion of the Cu electrodes to the Si wafer, multilayered (Figure 19) and mixed (Figure 3c) Ni–Cu electrodes were developed and their deposition mechanisms explored (cf. Sections 2.1 and 2.2).^[24,63,80] These novel Ni–Cu electrodes

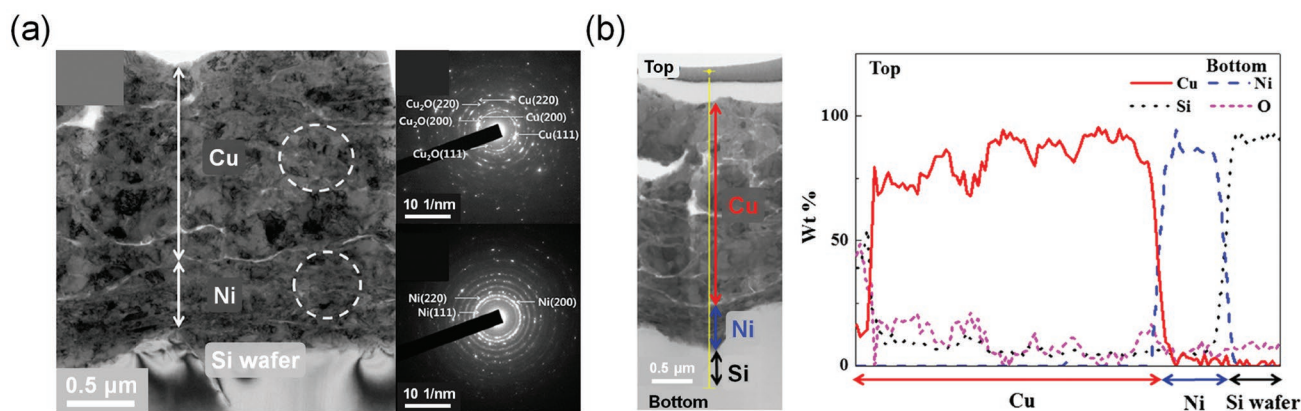


Figure 19. a) Cross-sectional transmission electron microscopy (TEM) and the corresponding selected-area electron diffraction (SAED) patterns of a Ni–Cu electrode on a Si wafer. b) Cross-sectional TEM image of a Ni–Cu electrode on a Si wafer and the corresponding energy-dispersive X-ray (EDX) line profile. a,b) Reproduced with permission.^[80] Copyright 2015, Elsevier.

exhibited advantageous conductivities compared to those produced by screen-printing and light-induced plating (LIP).

To take advantage of the excellent optoelectronic properties of graphene quantum dots (GQDs), the cold spraying method was employed to deposit GQD layers on c-Si surfaces and their corresponding performance as Si solar cells was evaluated (cf. Section 2.3 and Table 4).^[107] Different thicknesses of GQD layers on the hydrophilic surface of c-Si were obtained by varying the nozzle scan speed. In particular, an energy-down-shift effect of cold-sprayed GQD layers was found, where the corresponding wavelength range shifted from 300–420 to 450–700 nm. As a result, the power conversion efficiency (PCE) of specimens formed using the cold-sprayed GQD layer increased from 14.9% to 15.3%, with a 2.94% increase in the short-circuit current density.

In subsequent work, the cold spraying method was employed to fabricate lead chalcogenide (PbX, X = S, Se, or Te) QD films, overcoming some of the limitations of other techniques including poor colloidal stability, the need to use high-boiling-point solvents for dispersion, and complicated fabrication processes (cf. Table 5 and Section 2.4).^[128] The thickness of PbS QD films was varied by manipulating the number of sweeps of the supersonic nozzle, achieving an n-type QD film with a thickness of 300 nm (2.5 cm × 2.5 cm) in less than 1 min with 5 mg of PbS QD suspension. Note that prior to cold spraying, the PbS QD suspension was stabilized with methylammonium lead halide perovskite (MAPbI₃), thereby improving the colloidal stability of the PbS QDs. Additional treatment with 3-mercaptopropionic acid (MPA) caused the upper region of the n-type PbS QD film to change into a p-type material, resulting in a multilayered structure with a high PCE value of 3.7%.

3.1.2. Textured Surfaces for Efficient Cooling

The use of micro- and nanotextured surfaces on cooling systems—including heat pipes and heat exchangers—has been recognized as one of the best approaches to increase their cooling efficiency. This is because an increase in boiling nucleation sites (which corresponds to an increase in the surface-to-volume ratio) can effectively increase the rate of heat transfer in two-phase heat transfer systems. For example, the use of

cold-sprayed reduced graphene oxide (rGO) films on substrates enhanced heat transfer in pool boiling and convective cooling tests (cf. Section 2.3).^[102,103] Not only did the sharp edges of the rGO flakes produce a highly nanotextured surface on the Cu substrate, but the high kinetic energy of the supersonic flow also ensured strong adhesion and minimal resistance to heat transfer between the substrate and coating (Figure 9a). The nanotextured surface formed by the cold-sprayed rGO increased the density of nucleation sites for bubble formation, thus significantly enhancing the critical heat flux (CHF) and heat transfer coefficient compared with nontextured surfaces.

To further corroborate the applicability of the cold spraying method for cooling technologies, pyramid-shaped (or triangular) Cu lines (patterned on a Cu substrate) were studied and their cooling performance in pool boiling was examined. For this, Cu lines with a height and width of 128 and 348 μm, respectively, were deposited using different masking slits (Figure 6a, cf. Table 3, and Section 2.2).^[81] Because of the improved bubble release rate, these lines enhanced CHF values and heat transfer coefficients compared with a bare Cu substrate. In particular, 2 mm spaced Cu lines yielded the highest values of CHF and heat transfer coefficients (cf. Figure 6a). However, their performance in pool boiling started to deteriorate when the distance between the adjacent lines was less than 2 mm, probably because of bubble coalescence and the acceleration of film boiling. The heat transfer efficiency of frustum pyramid-shaped Cu pillars, which were fabricated via cold spraying with wire meshes is illustrated in Figure 6b and Table 3; cf. Section 2.2.^[82] The pool boiling performance with different geometric arrangements and configurations of Cu pillars revealed that pyramid-base lines with a width of 0.91 mm performed the best with respect to the heat transfer coefficient, CHF, and the cross-flow coolant velocity over the pyramids.

The effect of cold-sprayed Cu microstructures on heat transfer efficiency was also explored (Tables 1 and 2, and cf. Section 2.1).^[60,61] To deposit and form the pyramidal Cu fin arrays, steel wire mesh was used under the optimized cold spraying conditions (Figure 20a). The flow structures over the Cu fin arrays were predicted using FLUENT. It was found that the turbulence intensity resulting from the Cu fin arrays was significantly increased (Figure 20b,c).

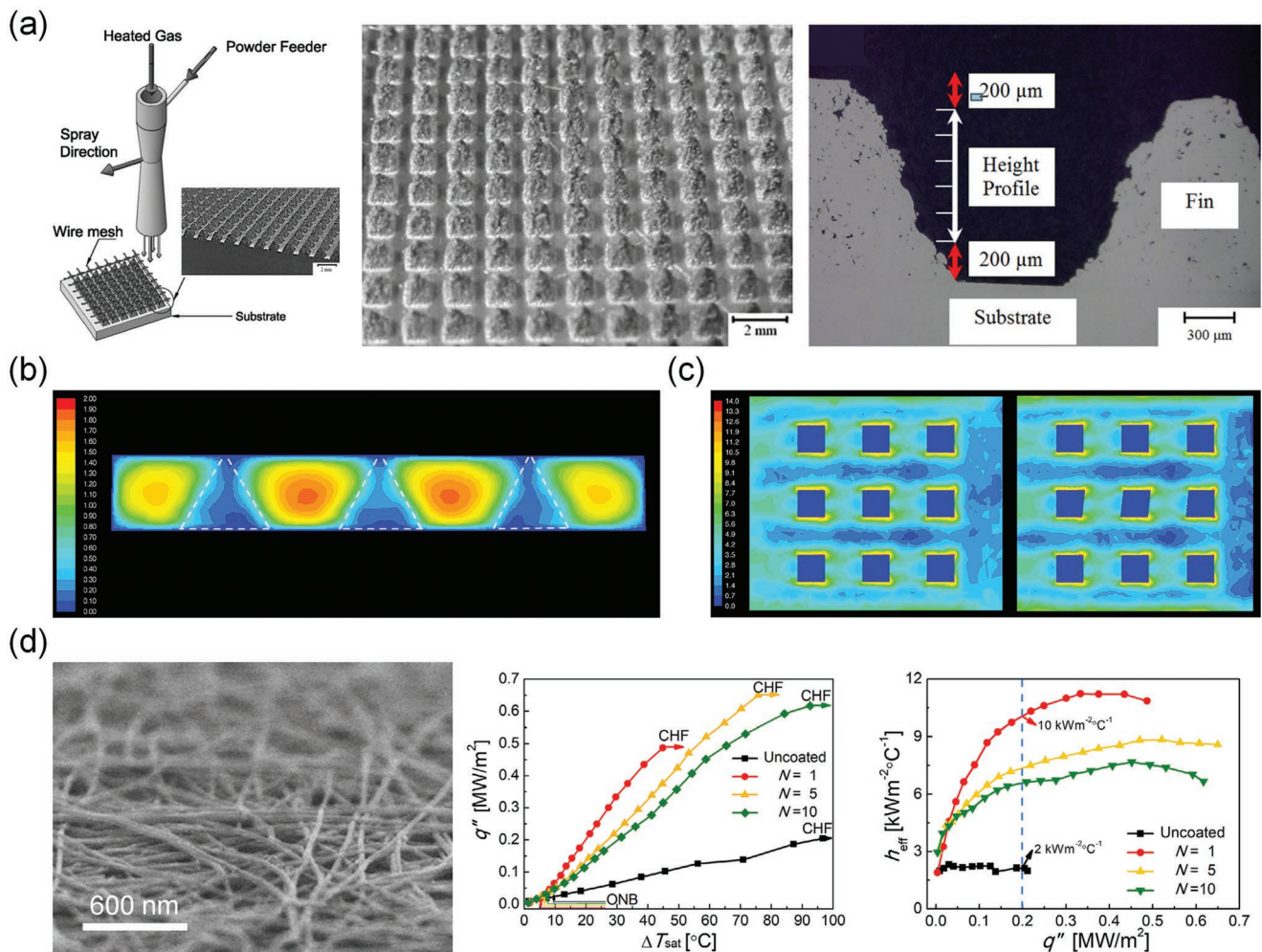


Figure 20. a) Sketch and photographs of cold-sprayed Cu fin arrays. b) Velocity distribution over Cu fin arrays. c) Turbulence intensity contour plots on Cu fin arrays. d) Scanning electron microscopy (SEM) image of cold-sprayed AgNWs on a Cu substrate and the corresponding results of pool boiling test: (middle) heat flux q'' as a function of superheat ΔT_{sat} , and (right) heat transfer coefficient as a function of the heat flux q'' . Note that N in the graphs indicates the number of sweeps of the supersonic nozzle during cold spraying. a-middle) Reproduced with permission.^[60] Copyright 2013, Springer Nature. a-left, a-right, and b, c) Reproduced with permission.^[61] Copyright 2016, Elsevier. d) Reproduced with permission.^[88] Copyright 2018, Elsevier.

In addition to microtextured Cu surfaces, the cooling performance of nanotextured Cu surfaces has also been explored (cf. Section 2.2)^[84] using substrates sandblasting with kanthal particles. Kanthal particles have a high hardness (8500 MPa), which implies that the topmost surface of the flattened (or layered) Cu particles could be dimpled by their impact significantly increasing surface area and the rate of cooling.

The effect of cold-sprayed silver nanowires (AgNWs) on pool boiling performance was also studied with the aim of enhancing the cooling efficiency of miniaturized electronics (Figure 20d, Table 3, cf. Section 2.2).^[84,88] Accordingly, pool boiling performance (including the CHF and heat transfer coefficient) was examined with different AgNW coating thicknesses, which caused some changes in surface wettability. Both the CHF and heat transfer coefficient of the AgNW surfaces were improved compared with those of the nontextured surfaces. However, very high texturing disrupted cooling because of trapping of nucleated bubbles, which then acted as an insulating layer within the densely entangled AgNWs.

3.1.3. Thermal and Electrical Insulation Films

Thermal barrier coatings (TBCs) and electrically insulating materials have been widely used in numerous industrial applications. For example, TBCs represent one of the most important coating layers in engines and turbines for prevention of degradation of these components. Also, electrically insulating materials are required in metallurgical processes including electrically assisted forging (EAF) and electrically assisted manufacturing (EAM).^[20,168–170] In these cases, various ceramic materials (e.g., aluminum oxide (Al₂O₃), titanium dioxide (TiO₂), and zirconium dioxide (ZrO₂)) have been used, as they meet the requirements for insulating materials, i.e., possess high melting temperatures, experience no phase changes under operating conditions, have low thermal conductivities and diffusivities, and similar thermal expansion coefficients to those of metals.^[171] However, there have been only a few reports exploring the use of clays and clay minerals with spraying methods despite the fact that they may also meet these requirements.

Cold spraying was used to fabricate thermally and electrically insulating layers of clays and clay minerals (cf. Section 2.6, Table 7).^[147–149] In particular, kaolinite, bentonite, and montmorillonite particles with sizes in the range of a few micrometers (cf. Figure 16b) were employed. These particles were mixed with a viscoelastic nylon solution to facilitate their dispersion and prevent agglomeration during the cold-spraying process (Table 7). The cold-sprayed clay films provided high values of electrical resistance of the order of 10^9 – 10^{10} Ω and, considering their favorable low thermal conductivity (10^{-1} – 10^0 $\text{W m}^{-1} \text{K}^{-1}$) and thermal diffusivity (10^{-7} – 10^{-6} $\text{m}^2 \text{s}^{-1}$), exhibited outstanding thermal insulation properties (Figure 16c).^[147]

Cold-sprayed clay films (produced under open-air conditions) were compared with aerosol-deposited ceramic layers (produced under vacuum).^[148] Although the aerosol-deposited ceramic films composed of Al_2O_3 and TiO_2 were harder and more scratch-resistant than the cold-sprayed clay films, they exhibited poorer electrical insulation properties because of the widespread occurrence of oxygen vacancies within the ceramics (as is characteristic of semiconducting metal oxides). While the cold spraying approach is a scalable process (because it can be performed in open air), aerosol deposition is less scalable due to the requirement of vacuum conditions.

The cold-sprayed clay films hybridized with aerogel achieve better thermal insulation performance than pristine cold-sprayed clay films (Figure 16d).^[149] Having in mind the superior insulating properties of silica aerogel (which is composed of $\approx 90\%$ air and $\approx 10\%$ silica by volume, and has an extremely low thermal conductivity on the order of $13 \text{ mW m}^{-1} \text{K}^{-1}$),^[172–174] montmorillonite clay particles were mixed with silica aerogel particles (at a volume ratio = 3:1) and used to fabricate a flexible insulating film on a poly(ethylene terephthalate) (PET) film (cf. Section 2.6). Although the hybrid clay–aerogel film exhibited relatively poor adhesive strength compared to the pristine clay films, the hybrid layer exhibited a discernible improvement in thermal insulation.

3.1.4. Transparent Conducting Films

Transparent conducting films (TCFs), which possess transmittance ($>85\%$) in the visible spectrum in the vicinity of 550 nm, and have a low sheet resistance ($<100 \Omega \text{ sq}^{-1}$), are crucial materials for various modern optoelectronic applications, especially those requiring touch-screen panels. In particular, as mobile phones have become an indispensable part of our everyday life, the global demand for TCFs (as critical components of touch-screen panels) has increased enormously. Therefore, many materials have been actively studied in recent years to improve TCF performance in terms of both optoelectronic and mechanical properties. An optimized cold spraying process for fabricating an rGO TCF (Tables 1 and 4, and cf. Section 2.3) was reported in ref. [91]. In terms of transmittance and sheet resistance, these films had comparable properties and increased flexibility compared to previously reported films produced using different methods (i.e., spin coating, vacuum filtration, and doctor blading). In particular, the deposited rGO films exhibited unique self-healing properties; specifically, the number of defects in the rGO was reduced after cold spraying due to the stretching of pentagonal and heptagonal rings in the rGO sheets (Figure 9c).

Recently, AgNWs have attracted significant attention as one of most promising nanomaterials for TCFs, overcoming limitations of indium tin oxide (ITO), conducting polymers, and carbon nanotubes (CNTs) in terms of low-cost and ultrafast fabrication of flexible and wearable electronics.^[9] However, the high contact resistance (or junction resistance) between overlapping AgNWs, which is an inevitable phenomenon in 1D nanomaterials in percolation networks, remains a significant issue for their further use in TCFs.^[85] To address this issue, the cold spraying technique was employed to develop flexible, stretchable, and scalable TCFs, the properties of which were attributed to the self-fusing of AgNWs driven by the high kinetic energy of cold spraying (cf. Section 2.2 and Figure 7).^[85] A large-scale AgNW film on a PET substrate was produced by a roll-to-roll cold spraying system (see Figure 7b). Notably, the percolating AgNWs deposited on an ecoflex polymer substrate could be stretched by up to 700% without significant electrical degradation. This is by far the highest demonstrated stretchability in AgNW TCFs. The cold-sprayed AgNW films exhibited remarkable performance in electrical and mechanical tests, revealing a low sheet resistance ($<10 \Omega \text{ sq}^{-1}$) and a high transmittance ($>90\%$) (Figure 7c). The deposition of AgNWs onto flexible PI (polyimide) substrates by cold spraying was also demonstrated and their electrical properties investigated.^[89] A multilayered AgNW film with ITO and zinc oxide (ZnO) (eventually forming PI/ITO/ZnO/AgNW layers) was also explored to demonstrate its potential as a window layer for flexible solar cells. Subsequently, transparent wearable heaters using AgNWs were developed based on the cold spraying technique (Table 3).^[86] In this case, a voltage was applied to the cold-sprayed AgNW film to induce Joule heating (Figure 8b,c), which allowed a maximum heating temperature of 160 °C. AgNWs were also successfully deposited onto complex surfaces (see Figure 8c). Based on these advantages for the fabrication of TCFs, and given that cold spraying does not require post-treatment and is a one-step and scalable process, one can conclude that it has potential to replace the existing TCF fabrication methods fairly quickly.

Having in mind other applications requiring extremely high temperatures,^[148] Cu–Ni thin films were formed by cold spraying mixed Cu–Ni powder (Figure 3d, Table 2, and Section 2.1).^[64] Even though these were opaque, they could be deposited onto various types of substrates including glass and polymers (see Figure 3d), and revealed a remarkable heating performance with heating temperatures that could reach over 1000 °C, and exhibited stable cyclic heating over 42 cycles.

3.1.5. Materials for Energy Storage

Flexible energy storage devices are of great interest for various applications, such as roll-up displays, wearable gadgets, biomedical implant devices, and health monitoring skins.^[175] These flexible batteries must provide a high specific capacity, possess a long lifetime, be low-cost, and be highly flexible. However, existing slurry coatings are unreliable in bending and insufficiently flexible because of poor adhesion of the electrode material to the current collector. This poor adhesion can result in film delamination during bending, thus hampering the performance of the electrode. There is, therefore, a need to find alternatives to slurry coating that can ensure adhesion and

overcome capacity loss. In this regard, the use of a binder-free supersonic cold spraying method becomes valuable, given that the cold spraying approach imparts high kinetic energy to particles, which significantly enhances adhesion to the substrate without the need for a binder (cf. Section 2).

Therefore, the cold spraying method was explored as a means of coating nanoscale materials, such as rGO, from suspensions (Section 2.3).^[91] One of the advantages of using rGO in a suspension is that it allows control over solvent evaporation, which can efficiently inhibit the aggregation of rGO flakes, thus providing uniform deposition of them. Moreover, this method allows one to reduce binder usage by providing stronger adhesion than the traditional slurry coating method.^[104] For example, rGO specimens were made by slurry coating^[104] for comparison with the adhesion achieved using the cold spraying approach. The scanning electron microscopy (SEM) images in Figure 10a,b reveal that the cold-sprayed rGO formed planar contact zones (or a complete contact) because of the high kinetic energy of cold spraying. This validated the superior adhesion achieved with the substrate (Cu foil) while the slurry rGO revealed a poor contact, as indicated by minimal contact points. As a result, in adhesion tests (Figure 10e), the pulling force as a function of distance for the cold-sprayed rGO was twice that of the slurry rGO. Moreover, electrochemical cycling tests revealed the superior performance of the cold-sprayed rGO films as anodes in lithium-ion batteries (LIBs). This is attributed to the lack of additives and the strong adhesion that reduces interfacial resistance. In addition, the LIB composed of the cold-sprayed rGO showed high flexibility with a consistent specific capacity.

As discussed in detail in Section 2.6, the cold spraying method can be used for deposition of various composites consisting of either nanomaterials or metal oxides. Note that LIBs involve three different mechanisms for lithium ion uptake, namely, intercalation, conversion, and alloying/dealloying (Figure 17). Materials appropriate for all these mechanisms based on composite forms with rGO were successfully fabricated via the cold spraying technique.^[153–155] In these cases, rGO acted as a cushioning matrix material, preventing metal oxides from agglomerating, while providing an electrically conducting scaffold. Optimized cold spraying conditions were identified for each of these material deposition methods, as summarized in Table 3. The transition metal oxides, such as TiO₂,^[153] iron (III) oxide (or hematite, Fe₂O₃),^[154] and zinc stannate (Zn₂SnO₄),^[155] were cold-sprayed and employed as anodes in LIB applications (cf. Figure 17). Samples were observed to be well adhered to the substrate (Cu foil) and remained intact for hundreds of charge/discharge cycles.

Transition metal carbides can also be prepared by the cold spraying method using metal salts along with relatively high concentrations of PAN. Iron carbide (Fe₃C) fibers and Fe₃C intertwined with rGO fibers were prepared by cold spraying using a polymer suspension (Table 7 and cf. Section 2.6).^[156] This method overcomes the needle-blocking problem that arises when rGO is intertwined with polymer precursors in other spinning methods.^[131] The resulting carbon-rich rGO/Fe₃C nanofibers yielded both good rate capability and excellent capacity retention.

The cold spraying method is also suitable for deposition of urea-derived g-CN composites (cf. Section 2.6).^[158] Cold-sprayed

g-CN/ZnFe₂O₃ hybrid composites exhibited intercalation (due to rGO), alloying (by ZnO → LiZn), and conversion (Fe₂O₃ → Fe) mechanisms of Li uptake. This hybrid composite, when coated via cold spraying followed by annealing, exhibited a capacity retention of 68% after 160 cycles relative to the first reversible capacity. As previously described, solution- or suspension-based supersonic cold spraying of various metal oxides and nanomaterials demonstrates the versatility and immense potential of the cold spraying technique for energy storage materials and especially for secondary battery systems.

While adding conducting carbon to metal oxides seems to be an obvious route to overcome poor conductivity of metal oxides when used as electrodes in LIBs, the growth of metal oxide particles over carbon requires wet chemistry methods, such as hydrothermal processes or chemical precipitation. The cold spraying technique plays a vital role here; when rGO is mixed with a metal oxide in a suspension and coated using supersonic spraying, the high-speed impact on the substrate tightly binds metal oxide particles to the rGO sheets. As mentioned above, in cold spraying, adhesion occurs via a mechanism associated with the plastic deformation and rupture of metal oxides at the interface with the substrate. Thus, the inclusion of rGO/g-CN sheets will bond metal oxide with carbon, providing a synergetic effect.

3.1.6. Photoelectrodes for Photoelectrochemical Water Splitting

Photoelectrochemical (PEC) or solar water splitting is a potential green energy source based on chemical storage of energy from sunlight in energy-rich hydrogen. PEC water splitting involves photocathodes that reduce water to H₂ and photoanodes that oxidize water to yield O₂. This technique exploits their different conduction and valence band potentials.^[176] The cold spraying technique can be used for the scalable production of binder-free photoelectrodes. For photocathodes, cold-sprayed cupric oxide (CuO) films were introduced using copper (I) oxide (Cu₂O) powder (with an average diameter of 0.5–1 μm) followed by annealing (Figure 12a–c, Table 5, and cf. Section 2.4).^[126] Supersonic cold spraying facilitated the in situ nanotexturing of Cu₂O films. These nanotextured morphologies—along the film surface—resembled dinosaur skin, with a surface roughness of ≈0.18 μm. These photocathodes exhibited a superior photocurrent density (PCD) of 3.1 mA cm⁻² (Figure 12a,c). This was achieved after the gas pressure and temperature were optimized to attain a critical velocity for the high-speed impact of sub-micrometer Cu₂O particles (Table 5). The sparse studies on photoelectrodes using the cold spraying technique demonstrate the need for deeper research with a thorough investigation of optimal parameters to take advantage of its rapid scaling and high-impact-driven adhesion.

Recently, the cold spraying technique was used for deposition of photoresponsive Fe₂O₃ particles for applications such as photoanodes (Figure 13a,b, Table 5, and Section 2.4).^[127] SEM observations clearly showed that Fe₂O₃ particles were well adhered to the substrate, and X-ray diffraction (XRD), and transmission electron microscopy (TEM) indicated that the crystal structure of the film did not show significant changes compared to pristine Fe₂O₃ powder, likely because of the low-temperature deposition

characteristic of cold spraying (cf. Figure 13a). Furthermore, additional surface passivation layers of these films formed by atomic layer deposition (ALD) of ZnO and TiO₂ could enhance their stability and photocurrent value (Figure 13c).

Earlier work not based on the cold spraying method revealed that the photoresponse of TiO₂ films fabricated by aerosol deposition depended upon film thickness. The highest photocurrent of 93 $\mu\text{A cm}^{-2}$ was obtained for a film thickness of 4 μm .^[177] However, for TiO₂ films irradiated with an electron beam, the PCD increased even more up to 0.205 mA cm^{-2} .^[178] Furthermore, to enhance the photocurrent, solution-based aerosol deposition was reported, whereby graphene was added to TiO₂ to reduce the electron–hole recombination and enable faster charge transfer. Such a composite film resulted in an enhanced PCD of 0.44 mA cm^{-2} .^[179]

3.2. Environmental Applications

3.2.1. Water Purification Membranes and Self-Cleaning Films

As one of the serious environmental concerns in modern society, access to clean water is a significant issue for both scientific and policy communities. Among various nanoscale carbon-based materials (e.g., graphene, CNTs, and fullerenes) with outstanding adsorption capacity and specific surface area, graphene has been intensively studied because of its remarkable theoretical specific surface area of 2630 $\text{m}^2 \text{g}^{-1}$ (cf. Section 2.3) and strong selective sorption capacity toward organics.^[90,180–182]

However, the use of graphene as a commercially viable water purification material has been prevented by its high cost and insufficient purification capacity, as evaluated by measuring a purifiable flow rate under a certain pressure differential. Meanwhile, a cost-effective and scalable process for fabricating rGO–nylon membranes (Figure 11, Table 3, and Section 2.3) via the cold spraying technique was demonstrated.^[106] The very thin and dense rGO membranes, which strongly locked rGO flakes within highly entangled and supersonically blown nylon 6 nanofibers, were fabricated (Figure 11b). This allows one to obtain very firm, portable rGO membranes (see Figure 11a insets). In particular, employing the cold spraying method enabled production of large-scale rGO–nylon membranes (0.0035 m^2) in less than 10 s. Moreover, in water purification tests undertaken using methylene blue (MB) solution (Figure 11c), such a membrane produced highly purified water at a flow rate of 4 L h^{-1} under a pressure differential of 3.5 bar. Recalculating for a larger membrane of the area of 0.5 m^2 , this result implies feasibility of achieving a purified water flow rate of 4000 L h^{-1} .

In buildings, the estimated energy loss caused by inefficient windows is $\approx 40\%$ of total energy consumption.^[183] Because dust particles present on the surface of windows can degrade their heat transfer efficiency, the use of self-cleaning windows has attracted much attention in recent decades.^[184] Self-cleaning films were developed using the cold spraying technique (Table 7 and cf. Section 2.6).^[146] Specifically, prior to cold spraying, TiO₂ nanoparticles with an average diameter of 21 nm were mixed with sub-micrometer poly(tetrafluoroethylene) (PTFE) particles. This allows tuning of the surface wettability of the

resulting cold-sprayed films from a superhydrophobic state to a superhydrophilic state, as a higher proportion of TiO₂ within the mixed powder results in a progressively more hydrophilic film. The change in water wetting from the Cassie–Baxter state, which exhibited a maximum water contact angle of 163°, to the Wenzel state was attributed not only to chemical modification but also to a change in the morphology of the cold-sprayed films from a rough compact structure to a porous one.

Other functions such as heating and thermal insulation have also been embedded in self-cleaning films based on cold-sprayed superhydrophobic polystyrene (PS) layers (cf. Section 2.5 and Table 6) or a combination of AgNWs and SiO₂ (Figure 15, cf. Sections 2.2 and 2.4, and Tables 3 and 5).^[87] Contrary to the use of PTFE particles in the study just described,^[146] a PS solution was sprayed to form a superhydrophobic layer (Figure 15b). Specifically, AgNWs and SiO₂ were cold-sprayed onto a PS layer for heating and thermal insulation, respectively. As a result, the multifunctional self-cleaning film not only exhibited a water contact angle of 120° but also demonstrated high performance with respect to thermal insulation and heating to over 100 °C (Figure 15c,d).

3.2.2. Metal–Organic Frameworks

Metal–organic frameworks (MOFs) are multifunctional materials composed of metal and organic ligands coordinated in a self-assembled manner, forming built-in 3D porosity. The porosity and high surface area of MOFs make them suitable for various applications, including gas sensing/separation, optoelectronics, catalysis, and energy storage.^[185–187] These applications could be expanded if high-throughput and scalable MOF film deposition methods were developed. MOFs, especially zeolitic imidazolate frameworks (ZIFs), have exhibited structural transformation under certain conditions of pressure and temperature. In this regard, various process parameters required to deposit ZIF-8 films using cold spraying were studied. ZIF-8 films were deposited and successfully retained the ZIF-8 structure when isopropyl alcohol (IPA) was used as the solvent (Section 2.6 and Table 7).^[162] The ZIF-8 structure amorphized when the cold spraying pressure was 0.7 MPa, which resulted in a strong-impact coating because of the increased velocity of the ZIF-8 nanoparticles. Furthermore, when the films were coated with high-boiling-point solvents, such as dimethylformamide (DMF), dimethylacetamide (DMA), and dimethyl sulfoxide (DMSO), the corresponding films demonstrated the preferred (112) film orientation (Figure 18a).

The influence of cold spraying with ZIF-7 has also been investigated, whereby cold spraying facilitates transformation of ZIF-7 to (002)-oriented ZIF-7 (phase III). This results from the high-velocity impact that contributes to breaking the six-membered rings to four-membered rings (see Figure 18b, and cf. Section 2.6 and Table 7).^[163] The ZIF-7 structural change was also observed at a lower air pressure of 0.2 MPa and a temperature of 250 °C. However, this structure breaking was prevented by the addition of 6 wt% nylon 6 solution. Nylon 6 modified the impact pressure by forming a kind of a shock-absorbing layer that provided mechanical stability to the ZIF-7 while the cold spraying retained the original crystalline structure of the ZIF-7.

Given that—similarly to ZIFs—MIL-100 (where MIL = Materials of Institute Lavoisier) with iron is a well-known MOF for water adsorption,^[164] MIL-100 films were also deposited by cold spraying and their application as humidity sensors was evaluated. The cold-spraying velocity did not affect the robust MIL-100 and, accordingly, its crystalline structure remained unchanged. Nitrogen adsorption on the cold-sprayed MIL-100 films was comparable to that of the pure powder. Water adsorption studies revealed two isotherm segments associated with the 2.5- and 2.9-nm mesopores, which were also comparable with those of pure powder. For use as a sensor, the electrical conductivity was altered by adding AgNWs into the MIL-100 because the pristine MIL-100 was nonconductive. When tested for humidity variations, the AgNW-containing composites revealed good

responsiveness, thus confirming their suitability for humidity sensing applications.

4. Summary and Outlook

Significant advances in energy and environmental applications of films produced by the supersonic cold spraying technique have been made in recent years, as discussed in Section 3. The underpinning fundamental research related to this technique allows improvement of supersonic flow characteristics and facilitates micromaterial deposition (Sections 1 and 2). In contrast to conventional bottom-up coating methods including sputtering and chemical vapor deposition (CVD)/physical vapor

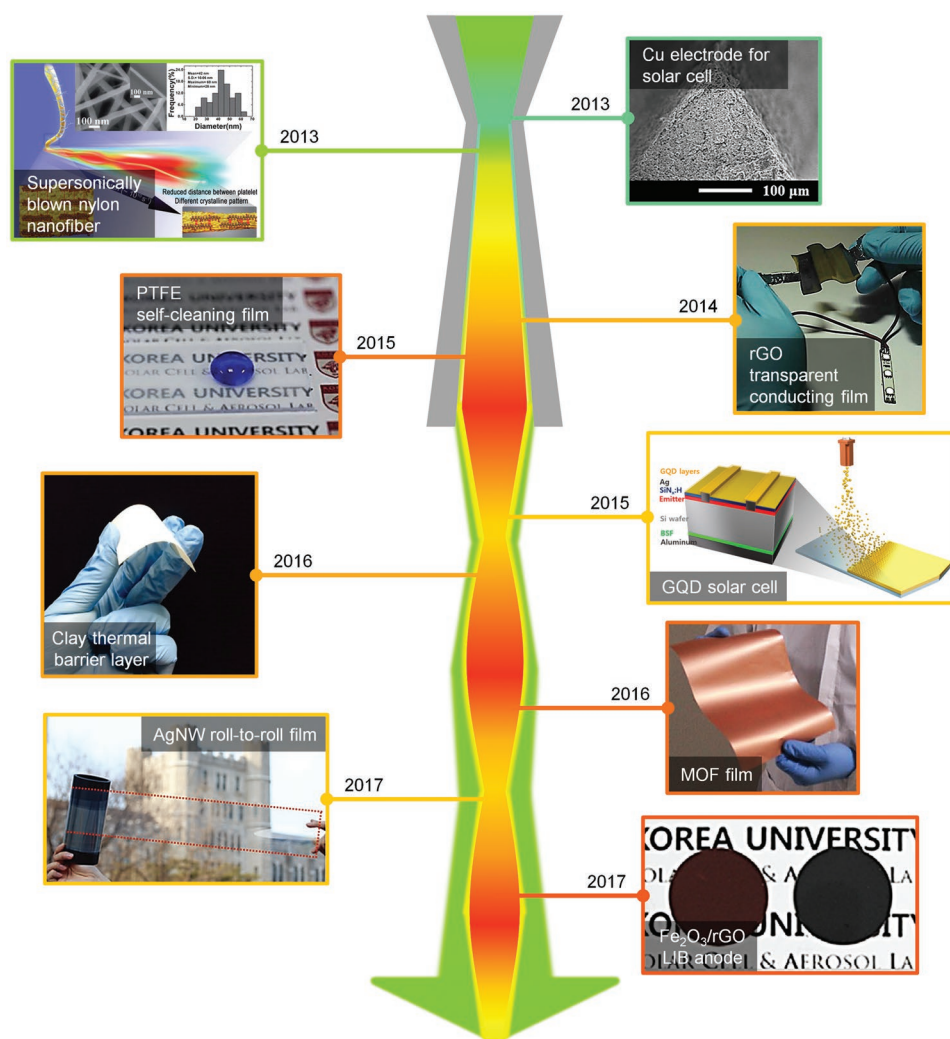


Figure 21. Chronology of important experimental studies of cold spraying technology for energy and environmental applications. From top to bottom: Image for “Cu electrode for solar cell”: Reproduced with permission.^[62] Copyright 2013, Springer Nature. Image for “Supersonically blow nylon nanofiber”: Reproduced with permission.^[136] Copyright 2013, Royal Society of Chemistry. Image for “rGO transparent conducting film”: Reproduced with permission.^[91] Copyright 2014, Wiley-VCH. Image for “PTFE self-cleaning film”: Reproduced with permission.^[146] Copyright 2015, Royal Society of Chemistry. Image for “GQD solar cell”: Reproduced with permission.^[107] Copyright 2015, American Chemical Society. Image for “Clay thermal barrier layer”: Reproduced with permission.^[147] Copyright 2016, Elsevier. Image for “MOF film”: Reproduced with permission.^[162] Copyright 2016, Elsevier. Image for “AgNW roll-to-roll film”: Reproduced with permission.^[85] Copyright 2017, Wiley-VCH. Image for “Fe₃O₄/rGO LIB anode”: Reproduced with permission.^[154] Copyright 2017, Elsevier.

deposition (PVD), the cold spraying technique can not only be operated under open-air conditions but can also be incorporated into roll-to-roll systems. The latter endows it immense potential as a commercially-viable industrial manufacturing process.

In this regard, the use of the cold spraying was recently introduced into various aspects of the energy and environmental fields, and a wide range of applications including cold-sprayed nanomaterials (e.g., reduced graphene oxide (rGO) and graphene quantum dots (GQDs)), polymers, clays, metal-organic frameworks (MOFs), and hybrid materials emerged as a result of this research (Figure 21). By virtue of its cost-effectiveness, fast deposition rate, and scalability, remarkable progress has been made in its efficiency and performance. This has led to significant improvements in the fields of solar cells, cooling and insulating films, thin conductive films (TCFs), lithium-ion batteries (LIBs), water purification membranes, and self-cleaning films (Section 3).

There are, however, numerous additional nanomaterials to which cold spraying could be applied. Pursuing these opportunities will result in further achievements in energy, environmental, and biomedical applications. Accordingly, the supersonic cold spraying technique will be of significant value to many scientists and engineers seeking a novel coating process for nanomaterials, and holds great promise for developers of novel technologies.

Acknowledgements

This research was supported by the Technology Development Program to Solve Climate Changes of the National Research Foundation (NRF) funded by the Ministry of Science, ICT & Future Planning, NRF-2016M1A2A2936760, NRF-2017R1A2B4005639, and NRF-2013R1A5A1073861. The generous support of NASA through the Grant No. NNX17AF33G is greatly appreciated.

Conflict of Interest

The authors declare no conflict of interest.

Keywords

energy and environmental applications, low-cost coating, multidimensional nanomaterial deposition, scalable nonvacuum coating, supersonic cold spraying, ultrathin flexible materials

Received: August 4, 2019

Revised: September 9, 2019

Published online:

-
- [1] A. D. Maynard, *Nat. Nanotechnol.* **2015**, *10*, 1005.
 [2] J. Scott, *Science* **2007**, *315*, 954.
 [3] Z. Yu, Q. Zhang, L. Li, Q. Chen, X. Niu, J. Liu, Q. Pei, *Adv. Mater.* **2011**, *23*, 664.
 [4] L. Ye, K.-T. Yong, L. Liu, I. Roy, R. Hu, J. Zhu, H. Cai, W.-C. Law, J. Liu, K. Wang, J. Liu, Y. Liu, Y. Hu, X. Zhang, M. T. Swihart, P. N. Prasad, *Nat. Nanotechnol.* **2012**, *7*, 453.
 [5] F. Xu, Y. Zhu, *Adv. Mater.* **2012**, *24*, 5117.
 [6] D. M. Sun, C. Liu, W. C. Ren, H. M. Cheng, *Small* **2013**, *9*, 1188.
 [7] V. Chabot, D. Higgins, A. Yu, X. Xiao, Z. Chen, J. Zhang, *Energy Environ. Sci.* **2014**, *7*, 1564.

- [8] P. Lopez-Varo, L. Bertoluzzi, J. Bisquert, M. Alexe, M. Coll, J. Huang, J. A. Jimenez-Tejada, T. Kirchartz, R. Nechache, F. Rosei, *Phys. Rep.* **2016**, *653*, 1.
 [9] S. An, H. S. Jo, D. Y. Kim, H. J. Lee, B. K. Ju, S. S. Al-Deyab, J. H. Ahn, Y. Qin, M. T. Swihart, A. L. Yarin, *Adv. Mater.* **2016**, *28*, 7149.
 [10] S. Gupta, L. Qiao, S. Zhao, H. Xu, Y. Lin, S. V. Devaguptapu, X. Wang, M. T. Swihart, G. Wu, *Adv. Energy Mater.* **2016**, *6*, 1601198.
 [11] P. J. Kelly, R. D. Arnell, *Vacuum* **2000**, *56*, 159.
 [12] K. Sarakinos, J. Alami, S. Konstantinidis, *Surf. Coat. Technol.* **2010**, *204*, 1661.
 [13] Y. H. Lee, X. Q. Zhang, W. Zhang, M. T. Chang, C. T. Lin, K. D. Chang, Y. C. Yu, J. T. W. Wang, C. S. Chang, L. J. Li, *Adv. Mater.* **2012**, *24*, 2320.
 [14] Y. Zhang, L. Zhang, C. Zhou, *Acc. Chem. Res.* **2013**, *46*, 2329.
 [15] D. M. Mattox, *Handbook of Physical Vapor Deposition (Pvd) Processing*, William Andrew, Norwich, NY, USA **2010**.
 [16] P. A. Pandey, G. R. Bell, J. P. Rourke, A. M. Sanchez, M. D. Elkin, B. J. Hickey, N. R. Wilson, *Small* **2011**, *7*, 3202.
 [17] P. Fauchais, J. V. Heberlein, M. I. Boulos, *Thermal Spray Fundamentals: From Powder to Part*, Springer, New York **2014**.
 [18] C. U. Hardwicke, Y.-C. Lau, *J. Therm. Spray Technol.* **2013**, *22*, 564.
 [19] M. R. Dorfman, A. Sharma, *J. Therm. Spray Technol.* **2013**, *22*, 559.
 [20] N. P. Padture, M. Gell, E. H. Jordan, *Science* **2002**, *296*, 280.
 [21] N. Espallargas, *Future Development of Thermal Spray Coatings: Types, Designs, Manufacture and Applications*, Woodhead Publishing, Cambridge, UK **2015**.
 [22] J. Villafuerte, *Modern Cold Spray: Materials, Process, and Applications*, Springer International Publishing, Cham, Switzerland **2015**.
 [23] W. Li, K. Yang, S. Yin, X. Yang, Y. Xu, R. Lupoi, *J. Mater. Sci. Technol.* **2018**, *34*, 440.
 [24] J.-G. Lee, D.-Y. Kim, B. Kang, D. Kim, S. S. Al-Deyab, S. C. James, S. S. Yoon, *Comput. Mater. Sci.* **2015**, *108*, 114.
 [25] H. Assadi, H. Kreye, F. Gärtner, T. Klassen, *Acta Mater.* **2016**, *116*, 382.
 [26] R. N. Raoulison, Y. Xie, T. Sapanathan, M. P. Planche, R. Kromer, S. Costil, C. Langlade, *Addit. Manuf.* **2018**, *19*, 134.
 [27] V. Champagne, D. Helfritsch, *Int. Mater. Rev.* **2016**, *61*, 437.
 [28] R. Dykhuizen, M. Smith, *J. Therm. Spray Technol.* **1998**, *7*, 205.
 [29] D. Gilmore, R. Dykhuizen, R. Neiser, M. Smith, T. Roemer, *J. Therm. Spray Technol.* **1999**, *8*, 576.
 [30] R. Dykhuizen, M. Smith, D. Gilmore, R. Neiser, X. Jiang, S. Sampath, *J. Therm. Spray Technol.* **1999**, *8*, 559.
 [31] E. H. Kwon, S. H. Cho, J. W. Han, C. H. Lee, H. J. Kim, *Met. Mater. Int.* **2005**, *11*, 377.
 [32] R. Huang, H. Fukanuma, *J. Therm. Spray Technol.* **2012**, *21*, 541.
 [33] J.-J. Park, M.-W. Lee, S. S. Yoon, H.-Y. Kim, S. C. James, S. D. Heister, S. Chandra, W.-H. Yoon, D.-S. Park, J. Ryu, *J. Therm. Spray Technol.* **2011**, *20*, 514.
 [34] M.-W. Lee, J.-J. Park, D.-Y. Kim, S. S. Yoon, H.-Y. Kim, S. C. James, S. Chandra, T. Coyle, *J. Therm. Spray Technol.* **2011**, *20*, 1085.
 [35] J.-J. Park, J.-G. Lee, S. C. James, S. S. Al-Deyab, S. Ahn, S. S. Yoon, *Comput. Mater. Sci.* **2015**, *101*, 66.
 [36] M. Grujicic, J. R. Saylor, D. E. Beasley, W. DeRosset, D. Helfritsch, *Appl. Surf. Sci.* **2003**, *219*, 211.
 [37] M. Grujicic, C. Zhao, W. DeRosset, D. Helfritsch, *Mater. Des.* **2004**, *25*, 681.
 [38] T. Stoltenhoff, H. Kreye, H. Richter, *J. Therm. Spray Technol.* **2002**, *11*, 542.
 [39] H. Assadi, F. Gärtner, T. Stoltenhoff, H. Kreye, *Acta Mater.* **2003**, *51*, 4379.
 [40] C. Borchers, F. Gärtner, T. Stoltenhoff, H. Assadi, H. Kreye, *J. Appl. Phys.* **2003**, *93*, 10064.
 [41] C. Borchers, F. Gärtner, T. Stoltenhoff, H. Kreye, *J. Appl. Phys.* **2004**, *96*, 4288.

- [42] C. Borchers, F. Gärtner, T. Stoltenhoff, H. Kreye, *Acta Mater.* **2005**, *53*, 2991.
- [43] T. Stoltenhoff, C. Borchers, F. Gärtner, H. Kreye, *Surf. Coat. Technol.* **2006**, *200*, 4947.
- [44] F. Gärtner, T. Stoltenhoff, J. Voyer, H. Kreye, S. Riekehr, M. Kocak, *Surf. Coat. Technol.* **2006**, *200*, 6770.
- [45] T. Schmidt, F. Gaertner, H. Kreye, *J. Therm. Spray Technol.* **2006**, *15*, 488.
- [46] T. Schmidt, F. Gärtner, H. Assadi, H. Kreye, *Acta Mater.* **2006**, *54*, 729.
- [47] T. Schmidt, H. Assadi, F. Gärtner, H. Richter, T. Stoltenhoff, H. Kreye, T. Klassen, *J. Therm. Spray Technol.* **2009**, *18*, 794.
- [48] H. Assadi, T. Schmidt, H. Richter, J.-O. Kliemann, K. Binder, F. Gärtner, T. Klassen, H. Kreye, *J. Therm. Spray Technol.* **2011**, *20*, 1161.
- [49] C.-J. Li, W.-Y. Li, *Surf. Coat. Technol.* **2003**, *167*, 278.
- [50] C.-J. Li, W.-Y. Li, Y.-Y. Wang, *Surf. Coat. Technol.* **2005**, *198*, 469.
- [51] W.-Y. Li, C.-J. Li, *J. Therm. Spray Technol.* **2005**, *14*, 391.
- [52] C.-J. Li, W.-Y. Li, H. Liao, *J. Therm. Spray Technol.* **2006**, *15*, 212.
- [53] W.-Y. Li, H. Liao, C.-J. Li, G. Li, C. Coddet, X. Wang, *Appl. Surf. Sci.* **2006**, *253*, 2852.
- [54] C.-J. Li, H.-T. Wang, Q. Zhang, G.-J. Yang, W.-Y. Li, H. Liao, *J. Therm. Spray Technol.* **2010**, *19*, 95.
- [55] W. Li, X. Guo, M. Yu, H. Liao, C. Coddet, *J. Therm. Spray Technol.* **2011**, *20*, 252.
- [56] R. Morgan, P. Fox, J. Pattison, C. Sutcliffe, W. O'Neill, *Mater. Lett.* **2004**, *58*, 1317.
- [57] J. Pattison, S. Celotto, A. Khan, W. O'Neill, *Surf. Coat. Technol.* **2008**, *202*, 1443.
- [58] R. Lupoi, W. O'Neill, *Surf. Coat. Technol.* **2010**, *205*, 2167.
- [59] M. J. Vucko, P. C. King, A. J. Poole, C. Carl, M. Z. Jahedi, R. de Nys, *Biofouling* **2012**, *28*, 239.
- [60] Y. Cormier, P. Dupuis, B. Jodoin, A. Corbeil, *J. Therm. Spray Technol.* **2013**, *22*, 1210.
- [61] P. Dupuis, Y. Cormier, M. Fenech, A. Corbeil, B. Jodoin, *Int. J. Heat Mass Transfer* **2016**, *93*, 301.
- [62] D.-Y. Kim, J.-J. Park, J.-G. Lee, D. Kim, S. J. Tark, S. Ahn, J. H. Yun, J. Gwak, K. H. Yoon, S. Chandra, *J. Therm. Spray Technol.* **2013**, *22*, 1092.
- [63] J.-G. Lee, J.-H. Lee, S. An, J. Y. Yoon, J.-W. Choi, M. G. Kang, J. I. Lee, H.-E. Song, S. S. Al-Deyab, S. C. James, *J. Alloys Compd.* **2017**, *695*, 3714.
- [64] J. G. Lee, D. Y. Kim, T. G. Kim, J. H. Lee, S. S. Al-Deyab, H. W. Lee, J. S. Kim, D. H. Yang, A. L. Yarin, S. S. Yoon, *Adv. Mater. Interfaces* **2017**, *4*, 1700075.
- [65] T. Van Steenkiste, J. Smith, *J. Therm. Spray Technol.* **2004**, *13*, 274.
- [66] F. Raletz, M. Vardelle, G. Ezo'o, *Surf. Coat. Technol.* **2006**, *201*, 1942.
- [67] P. S. Phani, D. S. Rao, S. Joshi, G. Sundararajan, *J. Therm. Spray Technol.* **2007**, *16*, 425.
- [68] T. Hussain, D. McCartney, P. Shipway, D. Zhang, *J. Therm. Spray Technol.* **2009**, *18*, 364.
- [69] L. Venkatesh, N. M. Chavan, G. Sundararajan, *J. Therm. Spray Technol.* **2011**, *20*, 1009.
- [70] W. Choi, L. Li, V. Luzin, R. Neiser, T. Gnäupel-Herold, H. Prask, S. Sampath, A. Gouldstone, *Acta Mater.* **2007**, *55*, 857.
- [71] P. C. King, M. Jahedi, *Appl. Surf. Sci.* **2010**, *256*, 1735.
- [72] Y. Zou, W. Qin, E. Irissou, J.-G. Legoux, S. Yue, J. A. Szpunar, *Scr. Mater.* **2009**, *61*, 899.
- [73] R. Lima, J. Karthikeyan, C. Kay, J. Lindemann, C. Berndt, *Thin Solid Films* **2002**, *416*, 129.
- [74] H.-K. Kang, S. B. Kang, *Scr. Mater.* **2003**, *49*, 1169.
- [75] H.-J. Kim, C.-H. Lee, S.-Y. Hwang, *Mater. Sci. Eng., A* **2005**, *391*, 243.
- [76] L. Ajdelsztajn, J. M. Schoenung, B. Jodoin, G. E. Kim, *Metall. Mater. Trans. A* **2005**, *36*, 657.
- [77] R. Ghelichi, D. MacDonald, S. Bagherifard, H. Jahed, M. Guagliano, B. Jodoin, *Acta Mater.* **2012**, *60*, 6555.
- [78] H. Bu, M. Yandouzi, C. Lu, D. MacDonald, B. Jodoin, *Surf. Coat. Technol.* **2012**, *207*, 155.
- [79] D. Goldbaum, J. M. Shockley, R. R. Chromik, A. Rezaeian, S. Yue, J.-G. Legoux, E. Irissou, *J. Therm. Spray Technol.* **2012**, *21*, 288.
- [80] J.-G. Lee, D.-Y. Kim, B. Kang, D. Kim, H.-e. Song, J. Kim, W. Jung, D. Lee, S. S. Al-Deyab, S. C. James, *Acta Mater.* **2015**, *93*, 156.
- [81] H. S. Jo, J.-G. Lee, S. An, T. G. Kim, S. C. James, J. Choi, S. S. Yoon, *Int. J. Heat Mass Transfer* **2017**, *113*, 210.
- [82] H. S. Jo, M.-W. Kim, T. G. Kim, S. An, H.-G. Park, J.-G. Lee, S. C. James, J. Choi, S. S. Yoon, *Int. J. Therm. Sci.* **2018**, *132*, 26.
- [83] B. Kang, K. D. Lee, J.-G. Lee, J.-W. Choi, S. S. Yoon, Y. Kang, H.-S. Lee, D. Kim, *J. Therm. Spray Technol.* **2016**, *25*, 465.
- [84] M.-W. Kim, T. G. Kim, H. S. Jo, J.-G. Lee, S. C. James, M. S. Choi, W. Y. Kim, J. S. Yang, J. Choi, S. S. Yoon, *Int. J. Heat Mass Transfer* **2018**, *123*, 1120.
- [85] J. G. Lee, D. Y. Kim, J. H. Lee, S. Sinha-Ray, A. L. Yarin, M. T. Swihart, D. Kim, S. S. Yoon, *Adv. Funct. Mater.* **2017**, *27*, 1602548.
- [86] J.-G. Lee, J.-H. Lee, S. An, D.-Y. Kim, T.-G. Kim, S. S. Al-Deyab, A. L. Yarin, S. S. Yoon, *J. Mater. Chem. A* **2017**, *5*, 6677.
- [87] J.-G. Lee, S. An, T.-G. Kim, M.-W. Kim, H.-S. Jo, M. T. Swihart, A. L. Yarin, S. S. Yoon, *ACS Appl. Mater. Interfaces* **2017**, *9*, 35325.
- [88] H. S. Jo, T. G. Kim, J.-G. Lee, M.-W. Kim, H. G. Park, S. C. James, J. Choi, S. S. Yoon, *Int. J. Heat Mass Transfer* **2018**, *123*, 397.
- [89] T.-G. Kim, J.-G. Lee, C.-W. Park, H.-S. Jo, M.-W. Kim, M. F. van Hest, D.-H. Cho, Y.-D. Chung, S. S. Yoon, *J. Alloys Compd.* **2018**, *739*, 653.
- [90] S. An, B. N. Joshi, J.-G. Lee, M. W. Lee, Y. I. Kim, M.-w. Kim, H. S. Jo, S. S. Yoon, *Catal. Today* **2017**, *295*, 14.
- [91] D. Y. Kim, S. Sinha-Ray, J. J. Park, J. G. Lee, Y. H. Cha, S. H. Bae, J. H. Ahn, Y. C. Jung, S. M. Kim, A. L. Yarin, *Adv. Funct. Mater.* **2014**, *24*, 4986.
- [92] K. S. Novoselov, A. K. Geim, S. V. Morozov, D. Jiang, Y. Zhang, S. V. Dubonos, I. V. Grigorieva, A. A. Firsov, *Science* **2004**, *306*, 666.
- [93] T. Lin, Y. Tang, Y. Wang, H. Bi, Z. Liu, F. Huang, X. Xie, M. Jiang, *Energy Environ. Sci.* **2013**, *6*, 1283.
- [94] K. S. Kim, Y. Zhao, H. Jang, S. Y. Lee, J. M. Kim, K. S. Kim, J.-H. Ahn, P. Kim, J.-Y. Choi, B. H. Hong, *Nature* **2009**, *457*, 706.
- [95] B. N. Chandrashekar, B. Deng, A. S. Smitha, Y. Chen, C. Tan, H. Zhang, H. Peng, Z. Liu, *Adv. Mater.* **2015**, *27*, 5210.
- [96] X. Wang, L. Zhi, K. Müllen, *Nano Lett.* **2008**, *8*, 323.
- [97] P. H. Wöbkenberg, G. Eda, D. S. Leem, J. C. De Mello, D. D. Bradley, M. Chhowalla, T. D. Anthopoulos, *Adv. Mater.* **2011**, *23*, 1558.
- [98] V. C. Tung, M. J. Allen, Y. Yang, R. B. Kaner, *Nat. Nanotechnol.* **2009**, *4*, 25.
- [99] E. Kymakis, K. Savva, M. M. Stylianakis, C. Fotakis, E. Stratakis, *Adv. Funct. Mater.* **2013**, *23*, 2742.
- [100] S. Gilje, S. Han, M. Wang, K. L. Wang, R. B. Kaner, *Nano Lett.* **2007**, *7*, 3394.
- [101] M. Bai, K. Xie, K. Yuan, K. Zhang, N. Li, C. Shen, Y. Lai, R. Vajtai, P. Ajayan, B. Wei, *Adv. Mater.* **2018**, *30*, 1801213.
- [102] S. An, D.-Y. Kim, J.-G. Lee, H. S. Jo, M.-W. Kim, S. S. Al-Deyab, J. Choi, S. S. Yoon, *Int. J. Heat Mass Transfer* **2016**, *98*, 124.
- [103] H. Yoon, M.-W. Kim, H. Kim, D.-Y. Kim, S. An, J.-G. Lee, B. N. Joshi, H. S. Jo, J. Choi, S. S. Al-Deyab, *Int. J. Heat Mass Transfer* **2016**, *101*, 198.
- [104] S. D. Kim, J.-G. Lee, T.-G. Kim, K. Rana, J. Y. Jeong, J. H. Park, S. S. Yoon, J.-H. Ahn, *Carbon* **2018**, *139*, 195.
- [105] P. Jacobson, B. Stöger, A. Garhofer, G. S. Parkinson, M. Schmid, R. Caudillo, F. Mittendorfer, J. Redinger, U. Diebold, *J. Phys. Chem. Lett.* **2012**, *3*, 136.
- [106] J.-G. Lee, D.-Y. Kim, M. G. Mali, S. S. Al-Deyab, M. T. Swihart, S. S. Yoon, *Nanoscale* **2015**, *7*, 19027.

- [107] K. D. Lee, M. J. Park, D.-Y. Kim, S. M. Kim, B. Kang, S. Kim, H. Kim, H.-S. Lee, Y. Kang, S. S. Yoon, B. H. Hong, D. Kim, *ACS Appl. Mater. Interfaces* **2015**, *7*, 19043.
- [108] X. Li, M. Rui, J. Song, Z. Shen, H. Zeng, *Adv. Funct. Mater.* **2015**, *25*, 4929.
- [109] F. Jiang, D. Chen, R. Li, Y. Wang, G. Zhang, S. Li, J. Zheng, N. Huang, Y. Gu, C. Wang, *Nanoscale* **2013**, *5*, 1137.
- [110] D. Damjanovic, *Rep. Prog. Phys.* **1998**, *61*, 1267.
- [111] K. I. Park, C. K. Jeong, J. Ryu, G. T. Hwang, K. J. Lee, *Adv. Energy Mater.* **2013**, *3*, 1539.
- [112] K. Y. Lee, D. Kim, J. H. Lee, T. Y. Kim, M. K. Gupta, S. W. Kim, *Adv. Funct. Mater.* **2014**, *24*, 37.
- [113] W. Seung, H. J. Yoon, T. Y. Kim, H. Ryu, J. Kim, J. H. Lee, J. H. Lee, S. Kim, Y. K. Park, Y. J. Park, *Adv. Energy Mater.* **2017**, *7*, 1600988.
- [114] S. W. Lee, Y. S. Lee, J. Heo, S. C. Siah, D. Chua, R. E. Brandt, S. B. Kim, J. P. Mailoa, T. Buonassisi, R. G. Gordon, *Adv. Energy Mater.* **2014**, *4*, 1301916.
- [115] Y. S. Lee, D. Chua, R. E. Brandt, S. C. Siah, J. V. Li, J. P. Mailoa, S. W. Lee, R. G. Gordon, T. Buonassisi, *Adv. Mater.* **2014**, *26*, 4704.
- [116] Y. J. Jang, J.-W. Jang, S. H. Choi, J. Y. Kim, J. H. Kim, D. H. Youn, W. Y. Kim, S. Han, J. S. Lee, *Nanoscale* **2015**, *7*, 7624.
- [117] Y. Lee, I. Leu, C. Liao, S. C. Chang, M. Wu, J. Yen, K. Fung, *Electrochem. Solid-State Lett.* **2006**, *9*, A207.
- [118] S. Bijani, M. Gabás, L. Martínez, J. Ramos-Barrado, J. Morales, L. Sánchez, *Thin Solid Films* **2007**, *515*, 5505.
- [119] P. Rai, R. Khan, S. Raj, S. M. Majhi, K.-K. Park, Y.-T. Yu, I.-H. Lee, P. K. Sekhar, *Nanoscale* **2014**, *6*, 581.
- [120] C.-Y. Chiang, M.-H. Chang, H.-S. Liu, C. Y. Tai, S. Ehrman, *Ind. Eng. Chem. Res.* **2012**, *51*, 5207.
- [121] S. Masudy-Panah, R. Siavash Moakhar, C. S. Chua, H. R. Tan, T. I. Wong, D. Chi, G. K. Dalapati, *ACS Appl. Mater. Interfaces* **2016**, *8*, 1206.
- [122] X. Guo, P. Diaio, D. Xu, S. Huang, Y. Yang, T. Jin, Q. Wu, M. Xiang, M. Zhang, *Int. J. Hydrogen Energy* **2014**, *39*, 7686.
- [123] Y.-F. Lim, C. S. Chua, C. J. J. Lee, D. Chi, *Phys. Chem. Chem. Phys.* **2014**, *16*, 25928.
- [124] P. Wang, Y. H. Ng, R. Amal, *Nanoscale* **2013**, *5*, 2952.
- [125] P. Basnet, Y. Zhao, *Catal. Sci. Technol.* **2016**, *6*, 2228.
- [126] J. G. Lee, D.-Y. Kim, J.-H. Lee, M.-W. Kim, S. An, H. S. Jo, C. Nervi, S. S. Al-Deyab, M. T. Swihart, S. S. Yoon, *ACS Appl. Mater. Interfaces* **2016**, *8*, 15406.
- [127] T.-G. Kim, B. Joshi, C.-W. Park, E. Samuel, M.-W. Kim, M. T. Swihart, S. S. Yoon, *J. Alloys Compd.* **2019**, *798*, 699.
- [128] H. Choi, J.-G. Lee, X. D. Mai, M. C. Beard, S. S. Yoon, S. Jeong, *Sci. Rep.* **2017**, *7*, 622.
- [129] D. N. Dirin, S. Dreyfuss, M. I. Bodnarchuk, G. Nedelcu, P. Papagiorgis, G. Itkos, M. V. Kovalenko, *J. Am. Chem. Soc.* **2014**, *136*, 6550.
- [130] M. W. Lee, S. An, S. S. Latthe, C. Lee, S. Hong, S. S. Yoon, *ACS Appl. Mater. Interfaces* **2013**, *5*, 10597.
- [131] A. L. Yarin, B. Pourdeyhimi, S. Ramakrishna, *Fundamentals and Applications of Micro-and Nanofibers*, Cambridge University Press, Cambridge, UK **2014**.
- [132] S. An, J. H. Hong, K. Y. Song, M. W. Lee, S. S. Al-Deyab, J. J. Kim, A. L. Yarin, S. S. Yoon, *Cellulose* **2017**, *24*, 951.
- [133] S. An, D. J. Kang, A. L. Yarin, *Nanoscale* **2018**, *10*, 16591.
- [134] S. An, A. Sankaran, A. L. Yarin, *ACS Appl. Mater. Interfaces* **2018**, *10*, 37749.
- [135] A. L. Yarin, M. W. Lee, S. An, S. S. Yoon, *Self-Healing Nanotextured Vascular Engineering Materials*, Springer Nature, Switzerland AG, Cham, Switzerland **2019**.
- [136] S. Sinha-Ray, M. W. Lee, S. Sinha-Ray, S. An, B. Pourdeyhimi, S. S. Yoon, A. L. Yarin, *J. Mater. Chem. C* **2013**, *1*, 3491.
- [137] S. An, C. Lee, M. Liou, H. S. Jo, J.-J. Park, A. L. Yarin, S. S. Yoon, *ACS Appl. Mater. Interfaces* **2014**, *6*, 13657.
- [138] I. Burlacov, J. Jirkovský, L. Kavan, R. Ballhorn, R. Heimann, *J. Photochem. Photobiol., A* **2007**, *187*, 285.
- [139] S. R. Bakshi, V. Singh, K. Balani, D. G. McCartney, S. Seal, A. Agarwal, *Surf. Coat. Technol.* **2008**, *202*, 5162.
- [140] Y. Tao, T. Xiong, C. Sun, H. Jin, H. Du, T. Li, *Appl. Surf. Sci.* **2009**, *256*, 261.
- [141] S. Cho, K. Takagi, H. Kwon, D. Seo, K. Ogawa, K. Kikuchi, A. Kawasaki, *Surf. Coat. Technol.* **2012**, *206*, 3488.
- [142] E. J. T. Pialago, O. K. Kwon, C. W. Park, *Appl. Therm. Eng.* **2013**, *56*, 112.
- [143] W. Li, C. Huang, M. Yu, D. Liu, Y. Feng, H. Liao, *Surf. Coat. Technol.* **2014**, *239*, 95.
- [144] S. Kumar, S. K. Reddy, S. V. Joshi, *Surf. Coat. Technol.* **2017**, *318*, 62.
- [145] R. Raolison, C. Verdy, H. Liao, *Mater. Des.* **2017**, *133*, 266.
- [146] D.-Y. Kim, J.-G. Lee, B. N. Joshi, S. S. Latthe, S. S. Al-Deyab, S. S. Yoon, *J. Mater. Chem. A* **2015**, *3*, 3975.
- [147] D.-Y. Kim, J.-G. Lee, B. Joshi, J.-H. Lee, S. S. Al-Deyab, H. G. Yoon, D. R. Yang, A. L. Yarin, S. S. Yoon, *Appl. Clay Sci.* **2016**, *120*, 142.
- [148] J.-G. Lee, D.-Y. Kim, B. N. Joshi, J.-H. Lee, T.-K. Lee, J.-S. Kim, D.-H. Yang, W.-Y. Kim, S. S. Al-Deyab, S. S. Yoon, *J. Therm. Spray Technol.* **2016**, *25*, 763.
- [149] T.-G. Kim, C.-W. Park, J.-G. Lee, M.-W. Kim, M. S. Choi, W. Y. Kim, J. S. Yoon, S. S. Yoon, *Ceram. Int.* **2018**, *44*, 12934.
- [150] K. Zhou, Y. Zhu, X. Yang, X. Jiang, C. Li, *New J. Chem.* **2011**, *35*, 353.
- [151] H. Fang, L. Zhao, W. Yue, Y. Wang, Y. Jiang, Y. Zhang, *Electrochim. Acta* **2015**, *186*, 397.
- [152] S. Goriparti, E. Miele, F. De Angelis, E. Di Fabrizio, R. P. Zaccaria, C. Capiglia, *J. Power Sources* **2014**, *257*, 421.
- [153] E. Samuel, J.-G. Lee, B. Joshi, T.-G. Kim, M.-w. Kim, I. W. Seong, W. Y. Yoon, S. S. Yoon, *J. Alloys Compd.* **2017**, *715*, 161.
- [154] J.-G. Lee, B. N. Joshi, J.-H. Lee, T.-G. Kim, D.-Y. Kim, S. S. Al-Deyab, I. W. Seong, M. T. Swihart, W. Y. Yoon, S. S. Yoon, *Electrochim. Acta* **2017**, *228*, 604.
- [155] T.-G. Kim, E. Samuel, B. Joshi, C.-W. Park, M.-W. Kim, M. T. Swihart, W. Y. Yoon, S. S. Yoon, *J. Alloys Compd.* **2018**, *766*, 331.
- [156] B. Joshi, J.-G. Lee, E. Samuel, H. S. Jo, T.-G. Kim, M. T. Swihart, W. Y. Yoon, S. S. Yoon, *J. Alloys Compd.* **2017**, *726*, 114.
- [157] S. An, B. N. Joshi, M. W. Lee, N. Y. Kim, S. S. Yoon, *Appl. Surf. Sci.* **2014**, *294*, 24.
- [158] B. Joshi, E. Samuel, T.-G. Kim, C.-W. Park, Y.-I. Kim, M. T. Swihart, W. Y. Yoon, S. S. Yoon, *J. Alloys Compd.* **2018**, *768*, 525.
- [159] X. Li, Y. Feng, M. Li, W. Li, H. Wei, D. Song, *Adv. Funct. Mater.* **2015**, *25*, 6858.
- [160] G. Wang, Z. Wen, Y.-E. Yang, J. Yin, W. Kong, S. Li, J. Sun, S. Ji, *J. Mater. Chem. A* **2018**, *6*, 7557.
- [161] H. Xu, X. Chen, L. Chen, L. e. Li, L. Xu, J. Yang, Y. Qian, *Int. J. Electrochem. Sci.* **2012**, *7*, 7976.
- [162] D.-Y. Kim, B. N. Joshi, J.-G. Lee, J.-H. Lee, J. S. Lee, Y. K. Hwang, J.-S. Chang, S. Al-Deyab, J.-C. Tan, S. S. Yoon, *Chem. Eng. J.* **2016**, *295*, 49.
- [163] B. N. Joshi, J.-G. Lee, S. An, D.-Y. Kim, J. S. Lee, Y. K. Hwang, J.-S. Chang, S. S. Al-Deyab, J.-C. Tan, S. S. Yoon, *Mater. Des.* **2017**, *114*, 416.
- [164] J.-G. Lee, B. N. Joshi, E. Samuel, S. An, M. T. Swihart, J. S. Lee, Y. K. Hwang, J.-S. Chang, S. S. Yoon, *J. Alloys Compd.* **2017**, *722*, 996.
- [165] Y. Li, F. Liang, H. Bux, W. Yang, J. Caro, *J. Membr. Sci.* **2010**, *354*, 48.
- [166] Y. Xu, L. Xu, S. Qi, Y. Dong, Z. U. Rahman, H. Chen, X. Chen, *Anal. Chem.* **2013**, *85*, 11369.
- [167] A. Cadiou, J. S. Lee, D. Damasceno Borges, P. Fabry, T. Devic, M. T. Wharmby, C. Martineau, D. Foucher, F. Taulelle, C. H. Jun, *Adv. Mater.* **2015**, *27*, 4775.
- [168] M. Peters, C. Leyens, U. Schulz, W. A. Kaysser, *Adv. Eng. Mater.* **2001**, *3*, 193.

- [169] A. Jordan, B. L. Kinsey, *J. Mater. Process. Technol.* **2015**, *221*, 1.
- [170] J.-G. Lee, Y.-H. Cha, D.-Y. Kim, J.-H. Lee, T.-K. Lee, W.-Y. Kim, J. Park, D. Lee, S. C. James, S. S. Al-Deyab, *J. Therm. Spray Technol.* **2015**, *24*, 1046.
- [171] X. Cao, R. Vassen, D. Stoeber, *J. Eur. Ceram. Soc.* **2004**, *24*, 1.
- [172] F. Shi, L. Wang, J. Liu, *Mater. Lett.* **2006**, *60*, 3718.
- [173] J. L. Gurav, I.-K. Jung, H.-H. Park, E. S. Kang, D. Y. Nadargi, *J. Nanomater.* **2010**, *2010*, 1.
- [174] J. P. Randall, M. A. B. Meador, S. C. Jana, *ACS Appl. Mater. Interfaces* **2011**, *3*, 613.
- [175] N. Li, Z. Chen, W. Ren, F. Li, H.-M. Cheng, *Proc. Natl. Acad. Sci. USA* **2012**, *109*, 17360.
- [176] M. G. Lee, J. S. Park, H. W. Jang, *J. Korean Ceram. Soc.* **2018**, *55*, 185.
- [177] J.-J. Park, D.-Y. Kim, J.-G. Lee, Y.-H. Cha, M. T. Swihart, S. S. Yoon, *RSC Adv.* **2014**, *4*, 8661.
- [178] S. S. Latthe, S. An, S. Jin, S. S. Yoon, *J. Mater. Chem. A* **2013**, *1*, 13567.
- [179] J. G. Lee, D. Y. Kim, J. J. Park, Y. H. Cha, J. Y. Yoon, H. S. Jeon, B. K. Min, M. T. Swihart, S. Jin, S. S. Al-Deyab, *J. Am. Ceram. Soc.* **2014**, *97*, 3660.
- [180] P. Lazar, F. e. Karlický, P. Jurečka, M. S. Kocman, E. Otyepková, K. R. Šafářová, M. Otyepka, *J. Am. Chem. Soc.* **2013**, *135*, 6372.
- [181] C. J. Russo, L. A. Passmore, *Nat. Methods* **2014**, *11*, 649.
- [182] S. An, H. S. Jo, K. Y. Song, M. G. Mali, S. S. Al-Deyab, S. S. Yoon, *Nanoscale* **2015**, *7*, 19170.
- [183] S. Grynning, A. Gustavsen, B. Time, B. P. Jelle, *Energy Build.* **2013**, *61*, 185.
- [184] M. Nosonovsky, P. K. Rohatgi, *Biomimetics in Materials Science: Self-Healing, Self-Lubricating, and Self-Cleaning Materials*, Springer Science & Business Media, New York **2011**.
- [185] J. C. Tan, J. D. Furman, A. K. Cheetham, *J. Am. Chem. Soc.* **2009**, *131*, 14252.
- [186] O. Shekhah, J. Liu, R. Fischer, C. Wöll, *Chem. Soc. Rev.* **2011**, *40*, 1081.
- [187] P. Falcaro, R. Ricco, C. M. Doherty, K. Liang, A. J. Hill, M. J. Styles, *Chem. Soc. Rev.* **2014**, *43*, 5513.